AB-INITIO NUMERICAL STUDIES IN SEMICONDUCTOR ALLOYS

THESE N° 1087 (1992)

PRESENTEE AU DEPARTEMENT DE PHYSIQUE

ECOLE POLYTECHNIQUE FEDERALE DE LAUSANNE

POUR L'OBTENTION DU GRADE DE DOCTEUR ES SCIENCES

PAR

STEFANO DE GIRONCOLI

laurea in fisica, Università degli Studi di Trieste, Italie
de nationalité italienne

acceptée sur proposition du jury:

Prof. A. Baldereschi, rapporteur
Prof. F. Bassani, corapporteur
Prof. M. Cardona, corapporteur
Dr K. Maschke, corapporteur

Lausanne, EPFL
1992

ai miei genitori,
Maria e Luigi

Résumé

Le sujet de ce travail de thèse est l'étude théorique, par des méthodes numériques *ab initio*, des propriétés physiques des alliages substitutionels entre composants semiconducteurs.

Les méthodes numériques *ab initio* sont aujourd'hui un outil théorique très puissant pour l'étude des propriétés physiques de structures cristallines, même dans le cas de structures d'une certaine complexité. Ces méthodes exploitent la périodicité du système; pour les appliquer à des systèmes désordonnés où la périodicité est perdue (telles que les solutions solides à semiconducteur), le système réel *non périodique* est substitué par un système *périodique* à très grande constante du réseau (une supercellule) qui reproduit la distribution locale des atomes existante dans l'alliage. Cependant, cette approximation étant d'autant plus satisfaisante que la cellule considérée est grande, les prévisions numériques précises peuvent demander des supercellules très grandes ($500 \div 1000$ atomes) auxquelles les méthodes actuelles ne sont plus applicables directement, et des nouvelles techniques sont nécessaires.

La différence chimique entre les composants semiconducteurs n'est pas très grande et on peut utiliser une approche en théorie de perturbations dans l'étude de leur alliages. En utilisant des techniques modernes très performantes, la description *ab initio* des alliages est ramenée à des modèles beaucoup plus simples qui, tout en gardant la qualité des résultats propre aux calculs *ab initio*, peuvent être étudiés facilement par des grandes supercellules. Par cette méthode les propriétés structurelles, thermodynamiques, vibrationelles et optiques de quelques alliages à semiconducteur ont été étudiées avec succès.

Abstract

This thesis is devoted to the theoretical study, by *ab initio* numerical methods, of the physical properties of substitutional semiconductor alloys.

Nowadays, *ab initio* numerical methods allow to study quite accurately the physical properties of moderately complex periodic systems. These methods exploit the periodicity of the system, and can be applied to disordered systems (such as the substitutional semiconductor alloys), where the periodicity is lost, by replacing the original *non-periodic* system by a *periodic* one, which contains several unequivalent atoms in a large unit cell (supercell), distributed in such a way to reproduce the local atomic coordination present in the alloy. However, since this approximation is the better the larger the supercell used, an accurate description of disorder can require supercells so large ($500 \div 1000$ atoms) that the usual methods become too expensive and new techniques have to be developed.

The chemical similarity between semiconductor components allows one to employ a perturbative approach in the study of their alloys. Exploiting the efficiency of modern perturbation techniques, we have been able to map the complex alloy problem onto much simpler models that, keeping the same accuracy of a complete first principles approach, can be easily studied with large supercells. By this approach, the structure, the thermodynamics, the lattice dynamics and the electronic structure of a few semiconductor alloys has been studied successfully.

Contents

Chapter 1

Introduction

This thesis is devoted to the study of substitutional semiconductor alloys. Semiconductor materials are technologically very important and they are the subject of much experimental and theoretical work[1]. Within this wide class of materials the elemental semiconductors (*Si*, *Ge*) and the *III-V* polar compounds (*III*: *Al*, *Ga*, *In*; *V*: *P*, *As*, *Sb*) in their cubic structures (diamond and zincblende structure, respectively) are the most studied and widely used for device applications. Since the existing number of such simple semiconductors is small, they provide only a limited range of materials properties and much attention is presently being payed to their alloys and superlattices with the purpose of tailoring at will their physical properties.

When studying semiconductor alloys, several questions both of fundamental and applied interest can be raised: *i)* First of all, an understanding of the structural properties and of the thermodynamical stability or instability of a given alloy with respect to its segregated components or to possible ordered structures is important and is a prerequisite to any further investigation of its properties. Even if, at ordinary growth temperatures, complete segregation or ordering is kinetically forbidden, the knowledge of the thermodynamical tendency to cluster, to segregate or to have a given short-range order is important to assess the physical limit below which it is no more reasonable to try to control at will the atomic positions in an atomic scale device (for instance in a superlattice). This eventually will set a limit to the tunability of the physical properties of the system. *ii)* A detailed knowledge of the vibrational properties of semiconductor alloys is also quite interesting. From the fundamental point of view, semiconductor alloys are simple realizations of disordered systems where the peculiar effects of disorder on the vibrational properties—such as the persistence or disappearance of well defined dispersion relations and the formation of localized or confined modes—can be studied. From the application point of view, the alloy vibrational properties are important because of their relevance for materials characterization through, *e.g.*, Raman spectroscopy. *iii)* Last but not least, an understanding of the modifications of the electronic structure of a material due to alloying—such as the variation of the fundamental and secondary band gaps and optical activity with composition—is desirable. This is maybe the most interesting effect of alloying from the application point of view.

The aim of the present work is to show that answers to these questions can be

given with accurate numerical studies. Lying midway between experimental and theoretical physics, computational physics is somewhat complementary to both of them and—with the growing power of large supercomputers—has become a valuable tool in the study of the properties of materials. It shares with theoretical physics the idea of studying a system by mapping it onto a suitable mathematical framework, where the physical parameters can be directly controlled and information, difficult or impossible to access experimentally, can be obtained. The use of numerical methods to solve the problem allows one to use a physical description sufficiently complex to be realistic and a numerical simulation can therefore give reliable information when experiments are lacking. Much as in experimental physics, the results of numerical simulations have to be properly analyzed to extract useful information from numerical noise, searching the best conditions to display and clarify the physical effects under study. Among computational approaches, *ab initio* methods based on the Density Functional Theory (DFT) of Hohenberg, Kohn and Sham[2,3] are the most sophisticated and have demonstrated to be very useful and reliable for the description of ground state properties in a large class of systems. For semiconductor materials DFT is very successful and has became the natural framework to study the structural and vibrational properties of simple and complex systems. As for optical properties, although they are—in principle—out of the reach of DFT,[4] DFT-derived band structures are in general reasonable as compared with experimental data and it is common practice to use them to extract some information in complex situations.

In spite of the many successes of DFT, even for complex systems, still very little has been done for disordered alloys. Symmetry is usually used to simplify the solution of problems and it is the lack of translational symmetry that renders so difficult the theoretical study of disordered alloys. One can recognize that the relevant properties of a disordered alloy do not depend on the particular random configuration of the system and can be obtained by averaging the properties of all possible configurations, thus recovering translational symmetry in the average. A popular way to circumvent the disorder problem is therefore to replace the random alloy by a translationally invariant effective medium that would reproduce the physical properties of the disordered system after configurational average. The problem is now to give a recipe to perform the average. Common approximations are—in order of increasing complexity and accuracy—the virtual crystal, the average T-matrix and the coherent potential approximations. We note, however, that even the most accurate of these effective medium approaches, can be badly inadequate in describing the effect of disorder in some apparently harmless situations, as, for instance, in the description of the lattice dynamics of binary alloys (see Chapter 4). This fact suggests to avoid effective medium approximations and to prefer other methods that account for disorder correctly though at an higher computational cost. The natural way to deal with disorder in a direct way without forgetting completely the standard concepts of solid state physics is to replace the disordered—not periodic—system by a periodic one with a very large unit cell (supercell) relying on the fact that physical properties depend essentially on the local environment of each atom[5] and are little affected by far regions. The larger is the supercell used the smaller will be the error made. If necessary the results of sev-

eral random periodic supercells can be averaged to reduce statistical error. Although conceptually very simple and exact in principle, this approach can require—to give accurate results—very large supercells ($100 \div 1000$ atoms in the unit cell) for which complete DFT calculations cannot be afforded, even with the large supercomputers existing today. One is thus apparently left with the choice between unreliable mean-field calculations and direct configurational average performed in supercells probably too small to be accurate.

For the alloys considered in this work, a practical solution to this seemingly unavoidable difficulty is to take advantage of the chemical similarity of semiconductor compounds. This allows one to use a perturbative approach in the investigation of the alloy still keeping the results accurate enough. The advantage of this approach is twofold: *i)* any alloy configuration is a slight perturbation of a periodic virtual crystal and the calculations can be performed exploiting the high symmetry of the unperturbed system, thus reducing the computational work considerably; *ii)* moreover, the perturbative approach allows one to map *exactly*—at the perturbative level being considered—the very complex DFT description of the alloy onto much simpler models (such as some generalized lattice-gas models for the thermodynamic properties or some rigid-ion models or ball-and-spring models for the vibrational properties), whose parameters are directly obtained from first principles calculations. Once the simple model has been constructed the alloy properties can be easily studied with supercells large enough to give accurate results.

1.1 Structure of this work

In Chapter 2 we give a short introduction to Density Functional Perturbation Theory, which is the framework of our theoretical approach, and explain how it makes possible the study of structural, thermodynamical, vibrational and electronic properties of substitutional semiconductor alloys. Chapters 3-5 form the body of this work and are devoted to applications of the method. In Chapter 3, the structural and thermodynamical properties of two paradigmatic alloys—$Ga_xAl_{1-x}As$ and Si_xGe_{1-x}—are studied showing similarities and differences between the pseudobinary lattice-matched and the binary lattice-mismatched case. Comparison with other theoretical works and the few existing experimental data is reported. In both materials no thermodynamic tendency to order is found and at ordinary temperature the random alloy is found to be the stable structure. Recently reported ordered structures in epitaxially grown samples are therefore probably induced by the growth process. In Chapter 4, the lattice dynamics of $Ga_xAl_{1-x}As$ and Si_xGe_{1-x} is examined. In this case more experimental data are available and our calculations help understanding the origin of some of the observed features. Some useful conclusion for materials characterization can also be drawn. Finally, in Chapter 5, the electronic structure of $Ga_xAl_{1-x}As$ alloy is studied. General conclusions and prospects for future extension of the present work are collected in Chapter 6.

Chapter 2

Theory of semiconductor alloys within density functional perturbation theory

In this chapter we describe a theoretical approach, based on Density Functional Theory (DFT), that allows to study—from first principles and in a unitary framework—the structure, the thermodynamics, the lattice dynamics and the electronic structure of semiconductor substitutional alloys. In this approach the alloy properties, as described by DFT, are mapped, using perturbation theory, into much simpler models that can be studied easily. In the next section, DFT and the linear-response techniques employed in the mapping process are briefly described. Later on in this chapter the models appropriate for the different properties of interest are derived.

As far as structural, thermodynamical, and vibrational properties are concerned the Born-Oppenheimer adiabatic approximation holds up to several thousands degrees Kelvin and the relevant quantity to investigate is the potential energy surface of the ions determined by the 'instantaneous' electronic ground state. DFT is an electronic ground state theory and can therefore describe all these properties in principle exactly. Optical properties, on the other hand, are determined by elementary electronic excitations in the system, which are outside the scope of DFT, and one should pass to a quasi-particle description.[6] This is by itself a very hard task[7] and combining that approach with a proper description of disorder is not feasible. In practice, however, DFT-derived band structures are usually quite reasonable and we will take the pragmatic attitude of assuming that disorder and quasi-particle effects act separately and will study the electronic properties at the DFT level, adding the quasi-particle corrections only at the end.

2.1 Density Functional Perturbation Theory

Let us fix notation starting from the beginning. The Hohenberg and Kohn theorem[2] states that it exists a universal functional, $F[n]$, of the electron density, $n(\mathbf{r})$, such that for any external potential, $V(\mathbf{r})$, acting on a N-electron system, the minimum of the

functional

$$\mathcal{E}_{el}[V,n] = F[n] + \int V(\mathbf{r})n(\mathbf{r})d\mathbf{r}, \tag{2.1}$$

under the constraint of a fixed number of electrons, $\int n(\mathbf{r})d\mathbf{r} = N$, is obtained for the ground state (GS) density of the electron system and the value of the functional at its minimum is the corresponding electronic GS energy. Splitting the functional $F[n]$ in a non-interacting kinetic energy term, $T_S[n]$, the classical electrostatic (Hartree) energy and the remaining "exchange-correlation" (xc) contribution, Kohn and Sham[3] formally solved the problem in terms of a set of equations for a system of non-interacting electrons in an effective self-consistent external potential:

$$\left[-\frac{\hbar^2}{2m}\nabla^2 + V_{eff}(\mathbf{r})\right]\phi_i(\mathbf{r}) = \varepsilon_i\phi_i(\mathbf{r}), \tag{2.2a}$$

$$V_{eff}(\mathbf{r}) = V(\mathbf{r}) + e^2\int\frac{n(\mathbf{r}')}{|\mathbf{r}-\mathbf{r}'|}d\mathbf{r}' + v_{xc}(\mathbf{r}), \tag{2.2b}$$

$$n(\mathbf{r}) = \sum_i |\phi_i(\mathbf{r})|^2, \tag{2.2c}$$

where the summation runs over the N lowest lying occupied states. The Kohn-Sham (KS) equations are only a formal solution because $v_{xc}(\mathbf{r})$ is the functional derivative of the unknown exchange-correlation functional $E_{xc}[n]$. The usefulness of DFT for practical purposes relies on the existence of simple and accurate approximations to $E_{xc}[n]$, and therefore to $v_{xc}(\mathbf{r})$, that completely specify and allow to solve the problem of Eqs. 2.2. The simplest and most widely used approximation is the so called Local Density Approximation (LDA) that states that the contribution of each small volume of the system to the exchange-correlation energy is the same as in an homogeneous electron gas of density equal to the local one:

$$E_{xc}^{LDA}[n] = \int \varepsilon_{xc}^{hom}(n(\mathbf{r}))n(\mathbf{r})d\mathbf{r} \quad\Longrightarrow\quad v_{xc}^{LDA}(\mathbf{r}) = \left.\frac{d(\varepsilon_{xc}^{hom}(n)n)}{dn}\right|_{n=n(\mathbf{r})} = \mu_{xc}^{hom}(n(\mathbf{r})), \tag{2.3}$$

where $\varepsilon_{xc}^{hom}(n)$ is the exchange-correlation energy per particle of the homogeneous electron gas of density n, and $\mu_{xc}^{hom}(n)$ is the exchange-correlation contribution to its chemical-potential. We will adopt this approximation and take the homogeneous electron gas data from the parameterization of Perdew and Zunger of the Ceperley and Alder Quantum MonteCarlo results.[8]

Suppose now that we have solved the problem for a given reference external potential, $V(\mathbf{r})$, and that the solution for some 'close' potential, $V(\mathbf{r}) + \lambda\Delta V(\mathbf{r})$, is needed. Due to the variational nature of the functional $\mathcal{E}_{el}(V,n)$ with respect to the electron density the error made by keeping n fixed at its unperturbed value is only second-order in the strength of the perturbation:

$$\mathcal{E}_{el}[V + \lambda\Delta V, n_\lambda] = \mathcal{E}_{el}[V + \lambda\Delta V, n_0] + \mathcal{O}(\lambda^2), \tag{2.4}$$

where n_0 is the GS density of the unperturbed system, and n_λ is the GS density of the perturbed system as a function of λ. This is the famous Hellman-Feynman

theorem[9] stating that first-order derivative of the total energy with respect to an external perturbation can be obtained from the knowledge of the unperturbed electronic GS only. From Eqs. 2.1 and 2.4 one readily obtains:

$$\frac{d\mathcal{E}_{el}}{d\lambda}\Big|_{\lambda=0} = \int \Delta V(\mathbf{r}) n_0(\mathbf{r}) d\mathbf{r}. \tag{2.5}$$

If the first-order variation, Δn, of the density with respect to λ is also known the error in the knowledge of the density is only second-order in λ and the energy of the perturbed system can therefore be determined with only a forth-order error in the strength of the perturbation:

$$\mathcal{E}_{el}[V + \lambda\Delta V, n_\lambda] = \mathcal{E}_{el}[V + \lambda\Delta V, n_0 + \lambda\Delta n] + \mathcal{O}(\lambda^4). \tag{2.6}$$

The second-order derivative of the total energy, with respect to the parameter λ, can be obtained by recognizing that Eq. 2.5 is actually valid for all values of λ (with n_λ substituted to n_0) and taking its derivative straightforwardly:

$$\frac{d^2\mathcal{E}_{el}}{d\lambda^2}\Big|_{\lambda=0} = \int \Delta V(\mathbf{r}) \Delta n(\mathbf{r}) d\mathbf{r}. \tag{2.7}$$

An expression for the third-order derivative of the energy can be found in Ref. 10.

The only non-trivial point in the previous derivation is the determination of the first-order variation of the density upon variation of the external potential. Linearization of Eqs. 2.2 yields:[11]

$$\left[-\frac{\hbar^2}{2m}\nabla^2 + V_{eff}(\mathbf{r}) - \varepsilon_i\right] \Delta\phi_i(\mathbf{r}) = -(\Delta V_{eff}(\mathbf{r}) - \langle\phi_i|\Delta V_{eff}|\phi_i\rangle)\phi_i(\mathbf{r}), \tag{2.8a}$$

$$\Delta V_{eff}(\mathbf{r}) = \Delta V(\mathbf{r}) + e^2 \int \frac{\Delta n(\mathbf{r}')}{|\mathbf{r} - \mathbf{r}'|} d\mathbf{r}' + \frac{d\mu_{xc}^{hom}}{dn}(n_0(\mathbf{r}))\, \Delta n(\mathbf{r}), \tag{2.8b}$$

$$\Delta n(\mathbf{r}) = 2\sum_i \phi_i^*(\mathbf{r})\Delta\phi_i(\mathbf{r}), \tag{2.8c}$$

that can be solved iteratively much in the same way as Eqs. 2.2, the main difference being that the eigenvalue equation for the ϕ's is replaced by a linear equation for the $\Delta\phi$'s.

An important technical point to notice is that these equations provide a convenient algorithm to calculate the wavefunction and density response of a periodic system to external perturbations of any periodicity. If the perturbing potential is characterized by a well defined wavevector $\mathbf{q}$ (*i.e.* $\Delta V(\mathbf{r}) = e^{i\mathbf{q}\mathbf{r}}\Delta\tilde{V}(\mathbf{r})$, with $\Delta\tilde{V}(\mathbf{r})$ periodic), it only couples—to linear order—Bloch states which differ by that wavevector, and the resulting density response bears the same periodicity as the perturbing potential. This feature is preserved through iterations and allows one to treat perturbations with different periodicity separately. Each perturbation, independently of $\mathbf{q}$, requires then a computational workload of the same order as that needed to solve the KS equations in the *unperturbed system.*

With the present method also macroscopically varying perturbations ($\mathbf{q} \to 0$), such as a macroscopic electric field, can be treated efficiently. The $\mathbf{q} \to 0$ limit in Eqs. 2.2 can be evaluated explicitly (see Appendix for details) and one is left with a system of coupled equations between the macroscopic and the microscopic (periodic) degrees of freedom, that can be solved much in the same way as in the usual case. This allows one to calculate accurately from first principles a number of important macroscopic response functions—such as dielectric[11,12] and piezoelectric constants[12]—and the Born effective charges,[12,13] relevant in the vibrational properties of polar materials, avoiding supercell and/or extrapolation techniques necessary, for instance, in the so-called *direct* method.[14]

To solve in practice the KS equations for an extended periodic system one takes advantage of its translational invariance and the resulting Bloch theorem. The Brillouin zone (BZ) integrations needed to construct the charge density and other relevant quantity are performed with the special points technique.[15] For each k-point in the BZ, the wavefunctions are expanded in a suitable finite basis-set. We use plane-wave basis-sets, where all plane-waves whose kinetic energy is lower than a given cutoff energy are included in the expansion. This choice—not the only possible one[16,17]—has the advantage that the matrix elements of the hamiltonian are particularly simple and that the convergence of the results with the number of basis-functions considered is easily checked by increasing the cutoff energy. In order to describe the electron-ion interactions we use *ab initio* non-local pseudopotentials[18] since no reasonably small plane-wave basis-set can describe the strongly localized core electrons. In the pseudopotential method the core electrons are simply missing and their effect on the valence ones is simulated by a smooth angular-momentum-dependent potential. In the previous discussion we have assumed, for simplicity, the electron-ion interactions being described by local pseudopotentials. The generalization to non-local ones is straightforward and is given for completeness in the Appendix.

Let us finally discuss the efficient implementation of the perturbative approach of Eq. 2.8. If the response to only a few perturbations is desired, it is convenient to solve Eq. 2.8a by iterative methods, as it is usually done for the eigenvalue problem of the unperturbed system. The computational effort needed is therefore of order N_{PW}^2 operations for each perturbation, where N_{PW} is the number of plane waves in the basis-set. Since we will need to compute the density response for perturbations corresponding to a fine grid of points in the BZ the iterative solution is not particularly useful and it is simpler to tridiagonalize once and for all the matrix in the l.h.s of Eq. 2.8a (an N_{PW}^3 operations step) and to solve then the linear problem straightforwardly (again only N_{PW}^2 operations for each perturbation).

2.2 Structure and Thermodynamics

The central idea of our approach to the structural and thermodynamical properties of semiconductor alloys is reminiscent of the pseudopotential perturbation theory[19] as applied to simple metals. In that case, simple metals are considered as sufficiently close

to the homogeneous electron gas to justify a perturbative expansion with respect to the strength of the atomic pseudopotentials, taking the jellium as reference system. Further approximations—as the use of oversimplified empty-core pseudopotentials and the RPA screening function of jellium—are usually made in order to simplify the problem. In our case the alloy is described within DFT using first-principles norm-conserving pseudopotentials[18] to describe the electron-ion interaction. Semiconductor alloys are sufficiently far from the homogeneous electron gas that the latter cannot be safely taken as a good reference system, and we take therefore the periodic 50% virtual-crystal corresponding to the alloy under investigation as a reference. As far as the chemical species forming the alloy are not too different a perturbative treatment with respect to the virtual-crystal is then justified and the reference system is still sufficiently simple that accurate linear-response techniques can efficiently be used to calculate the relevant interaction parameters with no approximation but the LDA one.

The thermodynamical properties of any system can be obtained by standard Boltzmann averages:

$$\langle \mathcal{A} \rangle = \frac{\sum_C \mathcal{A}(C) \exp(-\frac{\mathcal{E}(C)}{k_B T})}{\sum_C \exp(-\frac{\mathcal{E}(C)}{k_B T})}, \tag{2.9}$$

where C denotes a microscopic configuration of the system, $\mathcal{E}(C)$ its energy, $\mathcal{A}(C)$ the corresponding value of the relevant observable, T is the temperature, and k_B is the Boltzmann constant. Substitutional alloys are peculiar in the fact that all relevant configurations share the same underlying lattice—in our case the diamond or the zincblende lattice—and different configurations are identified by different distributions of atomic species on this lattice. If alloy atoms have different sizes the lattice is locally distorted, and the macroscopic structural parameters also vary with composition. Let us postpone the analysis of this important points for the moment and start our discussion in the simpler case where local distortions can be neglected.

Let the sites of the underlying lattice be labelled by $(\mathbf{R}, s)$, where $\mathbf{R}$ is a lattice vector and s identifies the atoms in the unit cell. Any microscopic configuration of a substitutional lattice-matched $A_x B_{1-x}$ alloy is then fully specified by a set of Ising-like variables, $C \equiv \{\sigma_{\mathbf{R},s}\}$, whose value is $\sigma_{\mathbf{R},s} = \pm 1$ if the lattice site $(\mathbf{R}, s)$ is occupied by an atom of species A or B respectively. DFT gives—in principle—the corresponding total energy:

$$\mathcal{E}(\{\sigma_{\mathbf{R},s}\}) = \mathcal{E}_{el}[V(\mathbf{r}, \{\sigma_{\mathbf{R},s}\}), n(\mathbf{r}, \{\sigma_{\mathbf{R},s}\})] + \mathcal{E}_{ion}(\{\sigma_{\mathbf{R},s}\}), \tag{2.10}$$

where $V(\mathbf{r}, \{\sigma_{\mathbf{R},s}\})$ is the external potential appropriate to the desired configuration, $n(\mathbf{r}, \{\sigma_{\mathbf{R},s}\})$ the corresponding GS density and $\mathcal{E}_{ion}(\{\sigma_{\mathbf{R},s}\})$ is the classical ionic contribution to the energy. However, the direct calculation of this energy is feasible only for configurations with no more than some tens of unequivalent atoms and cannot be performed in the general case considered here. This difficulty can be overcome by calculating approximately the configuration energies using perturbation theory.

The electron-ion interactions being described by pseudopotentials, it is easy to define a periodic 'reference' crystal in which all atoms are identical and correspond to a pseudopotential that is the average of the atomic potentials of the two component

atoms. This is the well known virtual crystal approximation to the 50% alloy. The external potential of any given alloy configuration, with A concentration $x = \frac{\langle\sigma\rangle+1}{2}$, can then be written as:

$$V(\mathbf{r}, \{\sigma_{\mathbf{R}s}\}) = V_{av}(\mathbf{r}) + \sum_{\mathbf{R},s} \sigma_{\mathbf{R}s} \Delta V_\sigma^s(\mathbf{r} - \mathbf{R}), \tag{2.11}$$

where $V_{av}(\mathbf{r})$ is the potential of the 50% virtual-crystal and $\Delta V_\sigma^s(\mathbf{r}) = \frac{1}{2}(V_A(\mathbf{r} - \boldsymbol{\tau}_s) - V_B(\mathbf{r} - \boldsymbol{\tau}_s))$ is the perturbing potential corresponding to the transformation of the s-th virtual atom (at position $\boldsymbol{\tau}_s$) of the elementary cell located at the origin in an A or B atom, according to the value of σ. Owing to the linearity of the problem and the translational symmetry of the unperturbed system the GS density for the given configuration can be written as:

$$n(\mathbf{r}, \{\sigma_{\mathbf{R}s}\}) = n_{av}(\mathbf{r}) + \sum_{\mathbf{R},s} \sigma_{\mathbf{R}s} \Delta n_\sigma^s(\mathbf{r} - \mathbf{R}) + \mathcal{O}(\sigma^2), \tag{2.12}$$

where $n_{av}(\mathbf{r})$ is the virtual-crystal GS density and $\Delta n_\sigma^s(\mathbf{r})$ is the density response of the virtual crystal to the "alchemical" perturbation $\Delta V_\sigma^s(\mathbf{r})$. Inserting this expression in the total energy and developing to second order in the σ's we obtain:

$$\mathcal{E}(\{\sigma_{\mathbf{R}s}\}) = \mathcal{E}_{av} + \sum_s K_s \sum_{\mathbf{R}} \sigma_{\mathbf{R}s} + \frac{1}{2} \sum_{\substack{\mathbf{R},\mathbf{R}' \\ s,s'}} J_{ss'}(\mathbf{R} - \mathbf{R}') \sigma_{\mathbf{R}s} \sigma_{\mathbf{R}'s'} + \mathcal{O}(\sigma^3), \tag{2.13}$$

where $\mathcal{E}_{av} = \mathcal{E}_{el}[V_{av}(\mathbf{r}), n_{av}(\mathbf{r})] + \mathcal{E}_{ion,av}$ is the energy of the virtual crystal and the 1-spin and 2-spin interaction parameters are given by:

$$K_s = \int \Delta V_\sigma^s(\mathbf{r}) n_{av}(\mathbf{r}) d\mathbf{r} + \frac{\partial \mathcal{E}_{ion}}{\partial \sigma_{0s}}, \tag{2.14a}$$

$$J_{ss'}(\mathbf{R} - \mathbf{R}') = \int \Delta V_\sigma^s(\mathbf{r} - \mathbf{R}) \Delta n_\sigma^{s'}(\mathbf{r} - \mathbf{R}') d\mathbf{r} + \frac{\partial^2 \mathcal{E}_{ion}}{\partial \sigma_{\mathbf{R}s} \partial \sigma_{\mathbf{R}'s'}}. \tag{2.14b}$$

Eq. 2.13 shows that the alloy problem can be mapped onto a lattice-gas with only two-body interactions (not necessarily short-range), the mapping being *exact* up to second order in the potential differences between the constituent atoms.[20]

Although their physical meaning of *interatomic* interaction parameters is more evident in the real space formulation given above, the $J_{ss'}(\mathbf{R})$'s are most conveniently computed by Fourier transforming their reciprocal space analogues:

$$J_{ss'}(\mathbf{R}) = \sum_{\mathbf{q}} e^{+i\mathbf{q}\mathbf{R}} J_{ss'}(\mathbf{q}), \tag{2.15a}$$

$$J_{ss'}(\mathbf{q}) = \int (\Delta V_\sigma^{s\mathbf{q}}(\mathbf{r}))^* \Delta n_\sigma^{s'\mathbf{q}}(\mathbf{r}) d\mathbf{r} + \frac{\partial^2 \mathcal{E}_{ion}}{\partial \sigma_{-\mathbf{q}s} \partial \sigma_{\mathbf{q}s'}}, \tag{2.15b}$$

where the summation in Eq. 2.15a runs over the entire BZ of the unperturbed system, $\sigma_{\mathbf{q}s} = \sum_{\mathbf{R}} e^{-i\mathbf{q}\mathbf{R}} \sigma_{\mathbf{R}s}$, $\Delta V_\sigma^{s\mathbf{q}}(\mathbf{r}) = \frac{1}{N} \sum_{\mathbf{R}} e^{+i\mathbf{q}\mathbf{R}} \Delta V_\sigma^s(\mathbf{r} - \mathbf{R})$ is a perturbation with well

defined wavevector, $\mathbf{q}$, and $\Delta n_\sigma^{s\mathbf{q}}(\mathbf{r})$ is the corresponding density response. In practice, the summation is performed only on a fine regular grid of wavevectors in the BZ, which corresponds to a large supercell in real-space, and the interaction parameters are thus known only up to a finite range. This is not a problem since the efficiency of the linear-response techniques allows one to perform the BZ integration accurately enough to account for all relevant interactions.

2.2.1 including lattice relaxation

So far, we have neglected all bond-length fluctuations which arise from chemical disorder. The problem of finding the bond-length distribution in a substitutional disordered system has been solved in the linear regime long time ago.[21,22] Here we use a similar approach, and extend it to determine the contribution of atomic relaxation to the energy of the alloy. Let us indicate by $\{\mathbf{u}_{\mathbf{R}s}\}$ the displacements of the atoms from their ideal lattice positions. The virtual crystal is in equilibrium with respect to atomic displacements and the equilibrium values of the u's in the alloy are to leading order linear in ΔV_σ. As a consequence, the general expression of the alloy energy as a function of the σ's and the u's reads:

$$\mathcal{E}(\{\sigma_{\mathbf{R}s}\},\{\mathbf{u}_{\mathbf{R}s}\}) = \mathcal{E}_{av} + \sum_s K_s \sum_{\mathbf{R}} \sigma_{\mathbf{R}s} + \frac{1}{2}\sum_{\substack{\mathbf{R},\mathbf{R}'\\ s,s'}} J_{ss'}(\mathbf{R}-\mathbf{R}')\sigma_{\mathbf{R}s}\sigma_{\mathbf{R}'s'}$$

$$+\frac{1}{2}\sum_{\substack{\mathbf{R},\mathbf{R}'\\ s,s'}} \mathbf{u}_{\mathbf{R}s}\cdot\mathbf{\Phi}_{ss'}(\mathbf{R}-\mathbf{R}')\cdot\mathbf{u}_{\mathbf{R}'s'} - \sum_{\substack{\mathbf{R},\mathbf{R}'\\ s,s'}} \mathbf{u}_{\mathbf{R}s}\cdot\mathbf{F}_{ss'}(\mathbf{R}-\mathbf{R}')\sigma_{\mathbf{R}'s'} + \mathcal{O}(\sigma^3), \quad (2.16)$$

where K_s and the J's are the interaction constants defined in Eq. 2.14; $\mathbf{\Phi}_{ss'}(\mathbf{R}-\mathbf{R}')$ is the matrix of the second-order derivatives of the energy with respect to atomic displacements from the ideal positions (*i.e* the virtual-crystal interatomic force constants, see later) and $\mathbf{F}_{ss'}(\mathbf{R})$ is the force acting on the virtual ion at site $(\mathbf{R},s)$ when the s'-th virtual ion of the unit cell located at the origin is replaced by a real one (the $\mathbf{F}$'s are sometimes referred to as Kanzaki's forces[21]). The explicit expressions, in real space, for the $\mathbf{\Phi}$ and $\mathbf{F}$ interaction parameters are:

$$\Phi_{\substack{s\ s'\\ \alpha\ \beta}}(\mathbf{R}-\mathbf{R}') = \int \Delta V^s_{\mathbf{u}^\alpha}(\mathbf{r}-\mathbf{R})\Delta n^{s'}_{\mathbf{u}^\beta}(\mathbf{r}-\mathbf{R}')d\mathbf{r} + \frac{\partial^2\mathcal{E}_{ion}}{\partial \mathbf{u}^\alpha_{\mathbf{R}s}\partial \mathbf{u}^\beta_{\mathbf{R}'s'}}, \quad (2.17a)$$

$$F_{\substack{s\ s'\\ \alpha}}(\mathbf{R}-\mathbf{R}') = -\int \Delta V^s_{\mathbf{u}^\alpha}(\mathbf{r}-\mathbf{R})\Delta n^{s'}_\sigma(\mathbf{r}-\mathbf{R}')d\mathbf{r} + \frac{\partial^2\mathcal{E}_{ion}}{\partial \mathbf{u}^\alpha_{\mathbf{R}s}\partial \sigma_{\mathbf{R}'s'}},$$

$$= -\int \Delta V^{s'}_\sigma(\mathbf{r}-\mathbf{R}')\Delta n^s_{\mathbf{u}^\alpha}(\mathbf{r}-\mathbf{R})d\mathbf{r} + \frac{\partial^2\mathcal{E}_{ion}}{\partial \mathbf{u}^\alpha_{\mathbf{R}s}\partial \sigma_{\mathbf{R}'s'}}, \quad (2.17b)$$

where $\Delta V^s_\sigma(\mathbf{r})$ and $\Delta n^s_\sigma(\mathbf{r})$ have been defined previously, and $\Delta V^s_{\mathbf{u}^\alpha}(\mathbf{r})$ and $\Delta n^s_{\mathbf{u}^\alpha}(\mathbf{r})$ are the perturbing potential and the induced density response associated to the displacement in the α direction of the s-th virtual atom of the elementary cell located at the origin. Eqs. 2.17 are valid for $(\mathbf{R},s)\neq(\mathbf{R}',s')$ only. The on-site term is slightly more

complicated, including a second-order derivative of the perturbing potential, but can easily be recovered requiring translational symmetry.

In Eq. 2.16, the u's are not independent variables: their values are those that, for any given microscopic configuration $\{\sigma_{\mathbf{R}s}\}$, minimize the energy:

$$-\frac{\partial \mathcal{E}}{\partial \mathbf{u}_{\mathbf{R}s}} = -\sum_{\mathbf{R}',s'} \mathbf{\Phi}_{ss'}(\mathbf{R}-\mathbf{R}')\cdot \mathbf{u}_{\mathbf{R}'s'} + \sum_{\mathbf{R}',s'} \mathbf{F}_{ss'}(\mathbf{R}-\mathbf{R}')\sigma_{\mathbf{R}'s'} = 0. \tag{2.18}$$

Eq. 2.18 simply states that at equilibrium the total force (Kanzaki's plus harmonic) acting on individual atoms vanishes. Solving Eq. 2.18 with respect to the u's gives:

$$\mathbf{u}^0_{\mathbf{R}s} = \sum_{\substack{\mathbf{R}',\mathbf{R}'' \\ s',s''}} \mathbf{\Phi}^{-1}_{ss'}(\mathbf{R}-\mathbf{R}')\cdot \mathbf{F}_{s's''}(\mathbf{R}'-\mathbf{R}'')\sigma_{\mathbf{R}''s''}. \tag{2.19}$$

Inserting Eq. 2.19 into Eq. 2.16, one arrives at an expression for the energy similar to Eq. 2.13—where lattice relaxation was neglected—in which relaxation does not appear explicitly, but the spin-spin interactions are renormalized by it. The final expression reads:

$$\mathcal{E}(\{\sigma_{\mathbf{R}s}\}) = \mathcal{E}_{av} + \sum_s K_s \sum_{\mathbf{R}} \sigma_{\mathbf{R}s} + \frac{1}{2}\sum_{\substack{\mathbf{R},\mathbf{R}' \\ s,s'}} \hat{J}_{ss'}(\mathbf{R}-\mathbf{R}')\sigma_{\mathbf{R}s}\sigma_{\mathbf{R}'s'} + \mathcal{O}(\sigma^3), \tag{2.20}$$

where

$$\hat{J}_{ss'}(\mathbf{R}-\mathbf{R}') = J_{ss'}(\mathbf{R}-\mathbf{R}') - \sum_{\substack{\mathbf{R}'',\mathbf{R}''' \\ s'',s'''}} \mathbf{F}_{s''s}(\mathbf{R}''-\mathbf{R})\cdot \mathbf{\Phi}^{-1}_{s''s'''}(\mathbf{R}''-\mathbf{R}''')\cdot \mathbf{F}_{s'''s'}(\mathbf{R}'''-\mathbf{R}'). \tag{2.21}$$

Again, the renormalized interaction parameters, $\hat{J}_{ss'}(\mathbf{R})$, are most easily calculated in reciprocal space, where convolutions are replaced by simple multiplications:

$$\hat{J}_{ss'}(\mathbf{q}) = J_{ss'}(\mathbf{q}) - \sum_{s'',s'''} \mathbf{F}_{ss''}(\mathbf{q})^{+}\cdot \mathbf{\Phi}^{-1}_{s''s'''}(\mathbf{q})\cdot \mathbf{F}_{s'''s'}(\mathbf{q}), \tag{2.22}$$

and then Fourier transformed to real space.

The same mechanism that determines fluctuations of the interatomic distances on the *microscopic* scale, also determines the dependence of the alloy equilibrium volume upon composition (*macroscopic* relaxation) and the two kinds of relaxation could be treated on the same footing by our method, in the harmonic regime. In fact, the $\mathbf{q} \to 0$ limits of $\mathbf{\Phi}_{ss'}(\mathbf{q})$ and of $\mathbf{F}_{ss'}(\mathbf{q})$ are related to the elastic constants and to the macroscopic stress induced by an "alchemical" perturbation, respectively. However, macroscopic relaxation can have important anharmonic contributions and it is more practical and accurate to deal with microscopic and macroscopic relaxation effects separately treating the elastic—macroscopic—term exactly and using Eq. 2.22 for the microscopic relaxation only. To this end, we define the alloy formation energy, $\Delta\mathcal{E}(\{\sigma_{\mathbf{R}s}\},\Omega)$, as the difference between the energy of the alloy in a given configuration

$\{\sigma_{\mathbf{R}s}\}$ and at a given molar volume Ω, and the appropriate average of those of the pure components at their respective equilibrium volumes:

$$\Delta\mathcal{E}(\{\sigma_{\mathbf{R}s}\},\Omega) = \mathcal{E}(\{\sigma_{\mathbf{R}s}\},\Omega) - x\mathcal{E}_A(\Omega_A) - (1-x)\mathcal{E}_B(\Omega_B), \tag{2.23}$$

where $\mathcal{E}_{A,B}$ and $\Omega_{A,B}$ are the equilibrium energies and volumes of the pure materials, and $x = \frac{\langle\sigma\rangle+1}{2}$ is the molar composition of the A_xB_{1-x} alloy. The formation energy can now be split into an elastic contribution, $\Delta\mathcal{E}_{\text{elast}}$, plus a configurational contribution, $\Delta\mathcal{E}_{\text{config}}$, where

$$\Delta\mathcal{E}_{\text{elast}}(x,\Omega) = x(\mathcal{E}_A(\Omega) - \mathcal{E}_A(\Omega_A)) + (1-x)(\mathcal{E}_B(\Omega) - \mathcal{E}_B(\Omega_B)) \tag{2.24}$$

is the energy paid to bring the two pure materials from their equilibrium volumes to the volume of the alloy and does not depend on the microscopic configuration but only on the macroscopic concentration, x, and

$$\Delta\mathcal{E}_{\text{config}}(\{\sigma_{\mathbf{R}s}\},\Omega) = \mathcal{E}(\{\sigma_{\mathbf{R}s}\},\Omega) - x\mathcal{E}_A(\Omega) - (1-x)\mathcal{E}_B(\Omega) \tag{2.25}$$

is the formation energy of the alloy at the *fixed volume* Ω. The elastic energy $\Delta\mathcal{E}_{\text{elast}}$ can be easily calculated from the equations of state for the pure components, whereas the configurational energy $\Delta\mathcal{E}_{\text{config}}$ is computed from the perturbative expansion of Eq. 2.20 using the $\tilde{J}$'s appropriate to the volume Ω:

$$\Delta\mathcal{E}_{\text{config}}(\{\sigma_{\mathbf{R}s}\},\Omega) = \frac{1}{2}\left(\sum_{s,s'}\sum_{\mathbf{R},\mathbf{R}'}\tilde{J}^{(\Omega)}_{ss'}(\mathbf{R}-\mathbf{R}')\sigma_{\mathbf{R}s}\sigma_{\mathbf{R}'s'} - N\sum_{s,s'}\sum_{\mathbf{R}}\tilde{J}^{(\Omega)}_{ss'}(\mathbf{R})\right). \tag{2.26}$$

In this way we account exactly for the anharmonic volume dependence of the elastic energy and also for some degree of anharmonicity in the configurational term through the volume dependence of the $\tilde{J}$'s. It should be noted that, in the calculation of the $\tilde{J}$'s to be inserted into Eq. 2.26, only the microscopic relaxation ($\mathbf{q} \neq 0$) has to be considered in the renormalization step (Eq. 2.22), since the macroscopic one is already accounted for exactly in the elastic term.

Once the alloy problem has been successfully mapped onto a lattice-gas model the resulting statistical-mechanical problem can be studied using standard mean-field or cluster-variation methods[23,24] or performing MonteCarlo simulations. From this study the variation of structural parameters of the alloy (bond-lengths, lattice parameters) as a function of composition as well as its thermodynamical properties (tendency to order or segregate, relative stability of different ordered structures) can be obtained.

Let us compare the present approach to the "Renormalized Interactions Method" (RIM) proposed by Zunger and coworkers[25] for the *ab initio* study of substitutional alloys. As in the present approach the alloy problem is mapped onto a lattice-gas model and the energy of the generic alloy configuration is expanded in terms of interatomic interactions that, in RIM, are fitted to the results of first-principles DFT calculations for a number of ordered structures that can be described by small supercells. Contrary to the present approach, RIM is not bound to systems whose chemical disorder is weak: in

fact, many-spin interactions can be extracted in a similar way as 2-spins ones, whereas in our approach the direct calculation of many-spins interactions is possible in principle but not very practical. On the other hand, RIM does not allow to treat long-range interactions, which cannot be extracted from calculations made for small supercells. Short-range interactions are therefore affected ("renormalized") by the neglect of long-range ones. As a consequence, RIM is an approximate scheme even in the limit of weak chemical disorder, whereas our scheme (which is based on perturbation theory and has practically no limitation in the range of the interactions) is exact in that limit. The importance of long-range interactions in lattice-mismatched semiconductor alloys has recently been recognized by Zunger and coworkers in Ref. 26.

2.3 Lattice dynamics

The vibrations of atoms around their equilibrium positions are determined by the shape of the energy surface near its (local) minimum. Phonons are the eigenmodes of this vibrational motion, defined expanding the energy of the system up to second order with respect to atomic displacements from equilibrium. For any periodic system, phonons frequencies can be obtained solving the eigenvalue problem:

$$\omega_\nu^2 \, M_s \, \mathbf{u}^\nu_{\mathbf{R},s} = \sum_{\mathbf{R}',s'} \Phi_{ss'}(\mathbf{R}-\mathbf{R}') \, \mathbf{u}^\nu_{\mathbf{R}'s'}, \tag{2.27}$$

where ω_ν is the frequency of the ν-th vibrational eigenmode, $\mathbf{u}^\nu_{\mathbf{R},s}$ is the corresponding displacement for the s-th atom in the unit cell located at $\mathbf{R}$, and M_s its atomic mass. The interatomic force constants appearing in Eq. 2.27, $\Phi_{ss'}(\mathbf{R}-\mathbf{R}')$, are second-order derivatives of the total energy with respect to atomic displacements from equilibrium positions. They can, therefore, be computed exactly within the Density Functional Perturbation Theory (DFPT) approach of Section 2.1.

In polar materials, the force constant matrix in reciprocal space, $\Phi_{ss'}(\mathbf{q})$, is non-analytic in the $\mathbf{q} \to 0$ limit. This is due to the long-range character of the Coulomb forces that can give rise to macroscopic electric fields for the long wavelength phonons, according to their polarization. The nonanalytical term has the general form:[27,28]

$$\Phi^{na}_{\substack{s\,s' \\ \alpha\,\beta}}(\mathbf{q}\to 0) = \frac{4\pi e^2}{\Omega} \frac{(\mathbf{q}\cdot\mathbf{Z}^*_s)_\alpha \, (\mathbf{q}\cdot\mathbf{Z}^*_{s'})_\beta}{\mathbf{q}\cdot\epsilon_\infty\cdot\mathbf{q}}. \tag{2.28}$$

Eq. 2.28 shows that all the information necessary to deal with the nonanalytic part of the dynamical matrix is contained in the high-frequency static dielectric tensor, ϵ_∞, and in the Born effective charge tensors, Z^*_s, of the different ions in the unit cell. Their calculation involves the density response to a macroscopic electric field, which can be easily obtained within DFPT (see the Appendix), and all the required quantities can, therefore, be calculated from first principles.

The mentioned nonanalyticity in reciprocal space makes the interatomic force constants in polar materials very long-range in real space, where their direct representation is not practical. An elegant solution to this problem is to take advantage of the known

origin of this nonanalyticity and, for each $\mathbf{q}$, subtract from the $\Phi_{ss'}(\mathbf{q})$ a term that in the limit $\mathbf{q} \to 0$ contains the whole non analyticity. The remaining $\tilde{\Phi}_{ss'}(\mathbf{q})$ is thus analytical and can be Fourier transformed in real space as usual. Whenever a particular $\Phi_{ss'}(\mathbf{q})$ is needed the analytic part is first constructed from the real space force constants and the nonanalytic term is then added directly in reciprocal space. The particular model used for the nonanalytic part is not very important, the only basic requirements being: *i)* to reproduce the correct behaviour at $\mathbf{q} \to 0$ (Eq. 2.28), *ii)* to behave smoothly throughout the BZ in order not to introduce in real space spurious long-range interactions and *iii)* to be easily calculated. All these requirements are met by choosing the nonanalytic term as the one arising from the Coulomb interaction of point-like ions of charge $Z_s^*/\sqrt{\epsilon_\infty}$. Note that with this choice the lattice-dynamical problem is mapped *exactly* onto a rigid-ion model whose real-space interaction constants, however, are not necessarily restricted to a small number of neighbors.

2.3.1 mass approximation and beyond

The study from first principles of the vibrational properties of a disorderd alloy is, in principle, straightforward: the disordered system is simulated by large supercells and, for any alloy configuration, $C \equiv \{\sigma_{\mathbf{R}s}\}$, the corresponding equilibrium positions are determined by minimizing the energy and the interatomic force constants, $\Phi_{ss'}^{(C)}(\mathbf{R}, \mathbf{R}')$, are computed by DFPT. However, the computational labour required by this procedure increases rapidly with the number of unequivalent atoms in the system and can be afforded only for small systems.[29] In the general case of a disordered alloy, the direct computation of the interatomic force constants is not feasible.

The practical solution to this difficulty relies again on perturbative arguments: the alloy is considered as a slight perturbation with respect to the 50% virtual crystal and its energy expanded in terms of the "alchemical" variables, $\{\sigma_{\mathbf{R}s}\}$, and the displacements from the ideal positions, $\{\mathbf{u}^0_{\mathbf{R}s}\}$. By truncating the energy expansion at a given perturbative level, one has a controlled approximation of the energetics of the alloy and then—for any configuration and at the given level of approximation—can easily calculate the atomic equilibrium positions and the interatomic force constants.

The simplest approximation in the above scheme is to include in the energy expansion only the second-order terms that can easily be computed within DFPT. This approximation yields the virtual-crystal interatomic force constants (the Φ's of Eq. 2.17a) for all alloy configurations and the only effect of chemical disorder on the alloy lattice dynamics is through the different atomic masses of its constituents:

$$\omega_\nu^2 \, M_{\mathbf{R}s}^{(C)} \, \mathbf{u}_{\mathbf{R}s}^\nu = \sum_{\mathbf{R}',s'} \Phi_{ss'}(\mathbf{R} - \mathbf{R}') \, \mathbf{u}_{\mathbf{R}'s'}^\nu. \tag{2.29}$$

This *mass approximation* was first introduced by Barker *et al.*[30] for *GaAs/AlAs* superlattices on empirical grounds and it has been recently demonstrated from first-principles calculations (see Ref. 31 and Chapter 4) to be valid for lattice-matched semiconductor systems.

In the case of lattice-mismatched alloys the mass approximation gives poor results[31] and corrections beyond it are necessary. The natural way to go beyond the mass approximation is to retain also the third-order terms in the expansion of the alloy energy:

$$\begin{aligned}
\frac{\partial^3 \mathcal{E}(\{\sigma_{\mathbf{R}s}\},\{\mathbf{u}_{\mathbf{R}s}\})}{\partial \mathbf{u}_{\mathbf{R}s}\partial \mathbf{u}_{\mathbf{R}'s'}\partial \mathbf{u}_{\mathbf{R}''s''}} &= \Phi^{(1)}_{ss's''}(\mathbf{R}-\mathbf{R}'',\mathbf{R}'-\mathbf{R}''),\\
\frac{\partial^3 \mathcal{E}(\{\sigma_{\mathbf{R}s}\},\{\mathbf{u}_{\mathbf{R}s}\})}{\partial \mathbf{u}_{\mathbf{R}s}\partial \mathbf{u}_{\mathbf{R}'s'}\partial \sigma_{\mathbf{R}''s''}} &= \mathbf{F}^{(1)}_{ss's''}(\mathbf{R}-\mathbf{R}'',\mathbf{R}'-\mathbf{R}''),\\
\frac{\partial^3 \mathcal{E}(\{\sigma_{\mathbf{R}s}\},\{\mathbf{u}_{\mathbf{R}s}\})}{\partial \mathbf{u}_{\mathbf{R}s}\partial \sigma_{\mathbf{R}'s'}\partial \sigma_{\mathbf{R}''s''}} &= \mathbf{J}^{(1)}_{ss's''}(\mathbf{R}-\mathbf{R}'',\mathbf{R}'-\mathbf{R}''),\\
\frac{\partial^3 \mathcal{E}(\{\sigma_{\mathbf{R}s}\},\{\mathbf{u}_{\mathbf{R}s}\})}{\partial \sigma_{\mathbf{R}s}\partial \sigma_{\mathbf{R}'s'}\partial \sigma_{\mathbf{R}''s''}} &= L_{ss's''}(\mathbf{R}-\mathbf{R}'',\mathbf{R}'-\mathbf{R}''). \qquad (2.30)
\end{aligned}$$

The interatomic force constants for any given configuration, $C \equiv \{\sigma_{\mathbf{R}s}\}$, are then given by

$$\begin{aligned}
\Phi^{(C)}_{ss'}(\mathbf{R},\mathbf{R}') = \Phi_{ss'}(\mathbf{R}-\mathbf{R}') &+ \sum_{\mathbf{R}'',s''} \Phi^{(1)}_{ss's''}(\mathbf{R}-\mathbf{R}'',\mathbf{R}'-\mathbf{R}'')\, \mathbf{u}^0_{\mathbf{R}''s''}\\
&+ \sum_{\mathbf{R}'',s''} \mathbf{F}^{(1)}_{ss's''}(\mathbf{R}-\mathbf{R}'',\mathbf{R}'-\mathbf{R}'')\, \sigma_{\mathbf{R}''s''}, \qquad (2.31)
\end{aligned}$$

where $\{\mathbf{u}^0_{\mathbf{R}s}\}$ are the displacements of the equilibrium positions, for the alloy configuration considered, from the ideal lattice sites.

All the third-order derivatives could, in principle, be obtained directly from a linear-response calculation for the virtual crystal using the method of Ref. 10 but it is easier to extract these *higher-order* interatomic force constants (HIFC's) by fitting Eq. 2.31 to a small number of independent high-symmetry configurations for which *ab initio* interatomic force constants can be computed directly. To reduce the number of parameters to be fitted, additional constraints have been imposed that enforce physically known properties of the HIFC's: *i)* permutation symmetry of the order of the derivatives in Eq. 2.30 is imposed, *ii)* the Acoustic Sum Rule (ASR)[32] for the generic configuration is required, which implies

$$\sum_{\mathbf{R},s} \Phi^{(1)}_{ss's''}(\mathbf{R}-\mathbf{R}'',\mathbf{R}'-\mathbf{R}'') = 0, \qquad (2.32)$$

$$\sum_{\mathbf{R},s} \mathbf{F}^{(1)}_{ss's''}(\mathbf{R}-\mathbf{R}'',\mathbf{R}'-\mathbf{R}'') = 0, \qquad (2.33)$$

for all $(\mathbf{R}',s')$ and $(\mathbf{R}'',s'')$, and *iii)* the first-order variations, $\Phi^{(1)}$ and $\mathbf{F}^{(1)}$, are required to correctly describe the effect of a rigid rotation of the system on the interatomic force constants of the virtual crystal,

$$\begin{aligned}
\sum_{\mathbf{R}',s'} \sum_{\rho\sigma} \Phi^{(1)}_{\substack{s\ s's''\\ \alpha\ \beta\ \sigma}}(\mathbf{R}-\mathbf{R}'',\mathbf{R}'-\mathbf{R}'')\, e_{\gamma\sigma\rho}\, (\mathbf{R}'+\boldsymbol{\tau}_{s'}-\mathbf{R}''-\boldsymbol{\tau}_{s''})_\rho =\\
\sum_{\sigma} e_{\gamma\alpha\sigma}\, \Phi_{\substack{s\ s'\\ \sigma\ \beta}}(\mathbf{R}-\mathbf{R}') + \sum_{\sigma} e_{\gamma\sigma\beta}\, \Phi_{\substack{s\ s'\\ \alpha\ \sigma}}(\mathbf{R}-\mathbf{R}'), \qquad (2.34)
\end{aligned}$$

and on the Kanzaki's forces of Section 2.2,

$$\sum_{\mathbf{R}'',s''} \sum_{\sigma\rho} F^{(1)}_{\substack{s\,s'\,s'' \\ \alpha\,\sigma}}(\mathbf{R}-\mathbf{R}'',\mathbf{R}'-\mathbf{R}'')\, e_{\gamma\sigma\rho}\,(\mathbf{R}'+\boldsymbol{\tau}_{s'}-\mathbf{R}''-\boldsymbol{\tau}_{s''})_\rho = \sum_{\sigma} e_{\gamma\alpha\sigma}\, F_{\substack{s\,s'' \\ \sigma}}(\mathbf{R}-\mathbf{R}'), \tag{2.35}$$

where $e_{\alpha\beta\gamma}$ is the Levi-Civita tensor.

To further reduce the number of free parameters we make the assumption that the effects of strain and chemical disorder are only local and we allow $\Phi^{(1)}$ and $\mathbf{F}^{(1)}$ not to vanish only for those triplets of sites that contain at least one first-nearest-neighbor pair and at most second-nearest-neighbor ones. This assumption is sound for $\mathbf{F}^{(1)}$ since other quantities—such as the $\mathbf{F}$ and the J of Section 2.2—that correspond to derivatives with respect to $\sigma_{\mathbf{R}s}$ are very short-range (see discussion in Chapter 3). The restriction is less justified for $\Phi^{(1)}$ since it is well known that in cubic semiconductors the IFC's are rather long-range along the bond chains in the (110) planes.[33] This feature is important to explain the characteristic flatness of their acoustic branch, and we expect, therefore, that the HIFC's we will obtain may not be completely satisfactory in the acoustic region.

Up to now, only non-polar lattice-mismatched materials have been studied with HIFC's (see Chapter 4), but the extension to polar materials is in principle straightforward. The above procedure is applied to obtain the *analytic* part of the HIFC's, which is fitted to the corresponding analytic part of the interatomic force constants computed from first princilples for a few ordered configurations. The nonanalytic part of HIFC's is determined by the first-order variations of the dielectric constant and of the effective charges, that can be fitted in a similar way to first-principles results. All these constraints are imposed by least square minimization and one ends up with a set of HIFC's that allows one to construct quite inexpensively the dynamical matrix of systems with several hundredth of unequivalent atoms, thus allowing to study homogeneous alloys as well as ordered and partially disordered superlattices.

2.4 Electronic structure

Band gaps in semiconductors and insulators are systematically underestimated if the KS eigenvalues of Eq. 2.2a are interpreted as single-particle excitation energies. Many important works[4] have shown this to be—more than a deficiency of the LDA approximation usually used in the calculation—an intrinsic feature of DFT, which is a ground state theory and is not suitable to describe excited states. Several attempts[7] to go beyond DFT have been made in recent years focusing on a quasi-particle description of electronic excitations in the *GW* approximation.[6] The DFT-derived electronic structure, however, remains the starting point for any further improvement, and it is often a very good starting point. In particular, DFT wavefunctions seem to be very close to the quasi-particle amplitudes obtained in more accurate schemes. Moreover, besides the already mentioned underestimation of the band gaps, DFT electronic structures compare reasonably well with experimental data as far as the topology of the bands

and the ordering of the energy levels are concerned. The study of the electronic structure of disordered alloys at the DFT level can therefore give useful information on the electronic properties of the real materials.

Even at the DFT level, the determination of the electronic structure of an alloy is a non-trivial problem since very large hamiltonian matrices have to be constructed and diagonalized to determine the single-particle states. The need for the self-consistent solution of the KS equations makes this task even more difficult and the direct determination of electronic properties of complex systems within DFT is usually limited to structures with some tens of unequivalent atoms in the unit cell. The proper account of disorder may require supercells of several hundreds of atoms, for which a complete DFT calculation is not possible. A interesting attempt to solve this problem is to search for some "Special Quasirandom Structure" (SQS)[34] that can be taken as representative of the disordered alloy, still having a small number ($8 \div 16$) of unequivalent atoms in the unit cell. Here we follow a different path, devising a way to solve the electronic problem accurately directly using large supercells.

As usual in this work the problem is solved considering the alloy as a perturbation with respect to the virtual crystal. Let us limit the discussion only to the case of lattice-matched alloys. The extension to lattice-mismatched systems is straightforward and will be briefly discussed at the end of the section. Two are the non-trivial steps in the determination of the alloy electronic structure: *i)* for any alloy configuration, $C \equiv \{\sigma_{\mathbf{R},s}\}$, the single-particle effective KS hamiltonian has to be constructed,

$$H^{(C)} = -\frac{\hbar^2}{2m}\nabla^2 + V_{eff}^{(C)}(\mathbf{r}), \tag{2.36}$$

and *ii)* the resulting eigenvalue problem has to be solved.

As for the first problem, the KS effective potential can be obtained, in close analogy with the discussion of Section 2.2, by superposing to the virtual-crystal potential, $V_{av,eff}(\mathbf{r})$, its first-order variation induced by elementary atomic substitutions of the virtual atoms with real ones:

$$V_{eff}^{(C)}(\mathbf{r}) \approx V_{av,eff}(\mathbf{r}) + \sum_{\mathbf{R},s} \sigma_{\mathbf{R},s} \Delta V^s_{\sigma,eff}(\mathbf{r} - \mathbf{R}), \tag{2.37}$$

where $\Delta V^s_{\sigma,eff}(\mathbf{r})$ is the first-order variation of the self-consistent potential, induced by the "alchemical" perturbation $\Delta V^s_\sigma(\mathbf{r})$ that transforms the s-th virtual atom of the unit cell at the origin into a real one, and reads:

$$\Delta V^s_{\sigma,eff}(\mathbf{r}) = \Delta V^s_\sigma(\mathbf{r}) + e^2 \int \frac{\Delta n^s_\sigma(\mathbf{r}')}{|\mathbf{r} - \mathbf{r}'|} d\mathbf{r}' + \frac{d\mu^{hom}_{xc}}{dn}(n_{av}(\mathbf{r}))\Delta n^s_\sigma(\mathbf{r}), \tag{2.38}$$

where $\Delta n^s_\sigma(\mathbf{r})$ is the density response to the perturbation and $n_{av}(\mathbf{r})$ is the ground state density of the unperturbed virtual crystal. Once this elementary variation of the KS potential is known—from the density functional perturbation theory of Section 2.1 (Eqs. 2.8)—, the single-particle KS potential for large supercells can be easily constructed, through Eq. 2.37, avoiding the self-consistent solution of the KS equations.

Note that, at variance with the total energy expansion of Sections 2.2 and 2.3, where the knowledge of the linear response of the density could give the total energy up to third order in the perturbation, here the *same* density response gives correctly only the linear term in the variation of the potential. This is due to the fact that the single-particle KS potential is *not* variational with respect to the density as it is, instead, the case for the total energy considered previously. Nevertheless, there is considerable evidence on the validity of linear response in the description of the electronic structure of complex semiconductor systems[35] and further evidence will be presented in Chapter 5.

Once the single-particle hamiltonian has been constructed, the corresponding eigenvalue problem has to be solved. To this end, the alloy wavefunctions are expanded into a suitable basis-set. A very practical choice is to write the alloy wavefunctions, $\psi(\mathbf{r})$'s, in terms of the virtual-crystal eigenfunctions, $\phi_{\mathbf{k},i}(\mathbf{r})$'s:

$$\psi(\mathbf{r}) = \sum_{i=1}^{N_b} \sum_{\mathbf{k}} c_i(\mathbf{k}) \phi_{\mathbf{k},i}(\mathbf{r}), \tag{2.39}$$

where the sum over $\mathbf{k}$ runs over the entire BZ and that over i includes the first N_b bands of the virtual crystal. This basis-set offers several advantages: *i)* it forms an orthonormal set, *ii)* it becomes complete in the limit of $N_b \to \infty$, and *iii)* its convergence can be easily checked including more bands. Even more important, due to the chemical similarity of the alloy and the virtual crystal, a basis-set including only a small number of virtual-crystal eigenfunctions per atom is expected to be enough to give converged results, thus allowing to study quite large systems accurately.

A great simplification in the evaluation of the hamiltonian matrix elements for a generic configuration can be obtained by expressing the total perturbing potential in terms of reciprocal space quantities:

$$\sum_{\mathbf{R}} \sigma_{\mathbf{R},s} \Delta V^{s}_{\sigma,eff}(\mathbf{r} - \mathbf{R}) = \sum_{\mathbf{q}} \sigma_{\mathbf{q},s} \Delta V^{s\mathbf{q}}_{\sigma,eff}(\mathbf{r}) \tag{2.40}$$

with $\sigma_{\mathbf{q},s} = \sum_{\mathbf{R}} e^{-i\mathbf{q}\mathbf{R}} \sigma_{\mathbf{R},s}$ and $\Delta V^{s\mathbf{q}}_{\sigma,eff}(\mathbf{r}) = \frac{1}{N} \sum_{\mathbf{R}} e^{+i\mathbf{q}\mathbf{R}} \Delta V^{s}_{\sigma,eff}(\mathbf{r} - \mathbf{R})$. With these notations the explicit form of the hamiltonian matrix elements is simply:

$$\langle \phi_{\mathbf{k},i} | H^{(C)} | \phi_{\mathbf{k}',j} \rangle = \bar{\varepsilon}_{\mathbf{k},i} \delta_{i,j} \delta_{\mathbf{k},\mathbf{k}'} + \sum_{s} \sigma_{\mathbf{k}-\mathbf{k}',s} \langle \phi_{\mathbf{k},i} | \Delta V^{s\,\mathbf{k}-\mathbf{k}'}_{\sigma,eff} | \phi_{\mathbf{k}',j} \rangle, \tag{2.41}$$

where $\bar{\varepsilon}_{\mathbf{k},i}$ is the single-particle energy of the i-th virtual-crystal band at the point $\mathbf{k}$ in the BZ. The hamiltonian matrix for any specific configuration depends on the alloy structure factors, $\sigma_{\mathbf{q},s}$, in a very simple way and moreover all the matrix elements of the perturbing potential are very easily obtained with the method of Section 2.1.

Let us finally discuss the almost trivial extension of the present approach to the case of lattice-mismatched alloys. In this case alloy atoms are displaced from the ideal positions and this relaxation has to be taken into account in the definition of the alloy KS potential. The relaxed atomic positions are easily evaluated from Eq. 2.19, and the linear variation of the KS effective potential due to lattice distortion can be calculated with the method of Section 2.1 and included in the definition of the alloy hamiltonian.

As it is the case for the total energy expansion of Section 2.2, lattice relaxation does not appear explicitly in the single particle hamiltonian, Eq. 2.41, but just in the definition of the variation of the KS effective potential that is renormalized by it:

$$\Delta\hat{V}^{s\mathbf{q}}_{\sigma,eff}(\mathbf{r}) = \Delta V^{s\mathbf{q}}_{\sigma,eff}(\mathbf{r}) + \sum_{s''} \Delta V^{s''\mathbf{q}}_{\mathrm{u},eff}(\mathbf{r}) \cdot \sum_{s'} \Phi^{-1}_{s''s'}(\mathbf{q}) \cdot \mathbf{F}_{s's}(\mathbf{q}), \qquad (2.42)$$

where $\Delta V^{s\mathbf{q}}_{\mathrm{u},eff}(\mathbf{r})$ is the linear variation of the virtual-crystal KS potential induced by the phonon-like displacement, with wavevector $\mathbf{q}$, of the s-th atoms in each unit cell of the crystal, and the $\mathbf{\Phi}_{ss'}$ and $\mathbf{F}_{ss'}$ are the harmonic and Kanzaki's forces of the crystal (Eqs. 2.17) evaluated in reciprocal space. In conclusion, for lattice-mismatched alloys the evaluation of the "ingredients" of the calculation is more complex, but once these have been obtained the study of their electronic properties is as simple as in the lattice-matched case.

Chapter 3

Structure and Thermodynamics

Since the early investigations of their thermodynamical properties,[36-38] semiconductor alloys have been considered model random alloys with a fairly simple phase diagram characterized by a miscibility gap below some critical temperature and no tendency to form ordered compounds. Direct experimental investigations of their solidus-solidus phase diagrams are generally lacking, due to very low atomic interdiffusion at the relevant temperatures, and the main sources of information are the solidus-liquidus diagrams that are well described by simple quasi-regular solution model.[24] In recent years, however, several groups[39-41] have reported on the formation (in epitaxially grown samples) of ordered semiconductor structures occurring unintentionally. An important question—of fundamental and applied interest—is therefore whether the recently observed ordered structures are only growth-induced and would disappear after appropriate annealing of the system or if they are instead the thermodynamically stable state of the alloy.

In this chapter we will study the bulk structural and thermodynamical properties of two paradigmatic examples of semiconductor alloys. As a first propaedeutic case we will consider $Ga_xAl_{1-x}As$ where strain effects can be neglected and the mapping of the alloy problem into a lattice gas model is particularly simple. The more complex situation where the two components forming the alloy have different lattice parameters will then be considered and the effects of strain—both macroscopic and microscopic—will be analyzed in some detail. As a definite example we will consider Si_xGe_{1-x}.

3.1 GaAlAs

$Ga_xAl_{1-x}As$ is a pseudobinary substitutional alloy with a zincblende structure. One of the two fcc sublattices is occupied by As atoms, while the two kinds of cations (Ga, Al) share the other one. According to early theoretical and experimental works,[36,37] $Ga_xAl_{1-x}As$ alloy is completely miscible and random at ordinary growth temperatures. Recently, however, it has reported to present spontaneous long-range order under particular growth conditions[39] and the corresponding ordered structure—the $(GaAs)_1/(AlAs)_1$ superlattice (SL) along the (001) direction (see Fig. 3.2)—has even been proposed as the stable thermodynamic state of the alloy at temperatures below

about $800°C$.

In this section the thermodynamics of $Ga_xAl_{1-x}As$ alloys is studied by the "computational alchemy" approach described in Chapter 2. Two are the essential features of this system that make it a particularly "easy" case in our approach: *i)* the two pure materials are chemically not very different so that a perturbative treatment with respect to the virtual crystal is expected to be quite accurate; *ii)* the *Ga–As* and *Al–As* bond-lengths are remarkably equal (experimentally they differ only by about 0.01 a.u.) so that lattice relaxation effects can be neglected when treating ordered or disordered compounds.

In the total energy and linear-response calculations presented below the interactions of valence electrons with *Ga*, *Al* and *As* (pseudo-)atoms are described by norm conserving[18] non-relativistic pseudopotentials generated with the recipe of Von Barth and Car.[42] A kinetic energy cutoff of 16 Ry and 10 special points[15] in the Brillouin Zone (BZ) of the zincblende structure are used. Whenever other structures are considered an equivalent set of sampling points is used. The calculated equilibrium lattice parameters for the pure materials are 10.60 a.u. (exp. 10.68) and 10.61 a.u. (exp. 10.69) for *GaAs* and *AlAs* respectively, only 1 % lower than the experimental values, an accuracy typical of DFT calculations in semiconductors. More importantly the almost perfect lattice-matching of the two materials is well reproduced by the calculation. Due to this extremely small lattice-mismatch in the following we will neglect atomic relaxation and all calculations will be performed at the average theoretical lattice constant of the two materials leaving the atoms at the ideal virtual-crystal positions.

Following the arguments of Chapter 2, the formation energy of any alloy configuration, $C \equiv \{\sigma_{\mathbf{R}}\}$, with respect to the segregated materials can be written as

$$\Delta\mathcal{E}(\{\sigma_{\mathbf{R}}\}) = \frac{1}{2}\left(\sum_{\mathbf{R},\mathbf{R}'} J(\mathbf{R}-\mathbf{R}')\sigma_{\mathbf{R}}\sigma_{\mathbf{R}'} - N\sum_{\mathbf{R}} J(\mathbf{R})\right), \tag{3.1}$$

where N is the number of elementary cells in the sample. The index which identifies the different atoms inside the virtual-crystal unit cell has been suppressed since only one fcc sublattice is actually affected by disorder and $\sigma_{\mathbf{R}} = \pm 1$ according to the cation (*Ga* or *Al*) occupying the site $\mathbf{R}$ in that sublattice. The formation energy of the random 50 % alloy is easily calculated from Eq. 3.1 assuming no correlation between different sites and reads:

$$\Delta\mathcal{E}_{\text{Random}} = -\frac{N}{2}\sum_{\mathbf{R}\neq 0} J(\mathbf{R}). \tag{3.2}$$

The interaction parameters, J's, have been computed in reciprocal-space on a regular grid of points allowing to determine the real-space interatomic interactions up to the sixth fcc (13^{th} zincblende) shell of neighbours. In Fig. 3.1 we display the calculated $J(\mathbf{R})$ as a function of the interatomic distance. The interaction constants are quite short-range and practically vanish beyond the first fcc shell of neighbours (the 2^{nd} shell in the zincblende lattice). The important interaction parameters are negative *i.e.* clustering of like atoms, and therefore segregation, is energetically preferred. Interatomic interaction constants seem to be very short-range whenever only the chemical part is

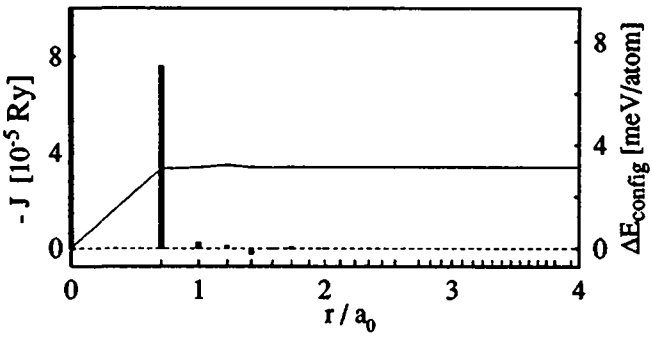

Figure 3.1: Atomic interatomic constants of $Ga_xAl_{1-x}As$ alloy (thick vertical bars) as a function of the atomic separation r. Thin vertical bars on the horizontal axis indicate shells of neighbours in the fcc cationic sublattice. The solid line indicate the formation energy of the random alloy in the quasi-regular solution approximation, obtained by truncating the interactions at a given shell of neighbours.

considered and lattice relaxation is absent or neglected. The same behaviour will be found for Si_xGe_{1-x} alloys when only the chemical part of the interaction is considered. Inclusion of lattice relaxation—important in that case, negligible here—changes *qualitatively* the behaviour of the interatomic interaction constants, $J(\mathbf{R})$, making them long-range.

The accuracy of the present approach in the description of alloy thermodynamics relies on the ability of the perturbative expansion of Eq. 3.1 to reproduce the results of complete DFT calculations. This is demonstrated in Table 3.1 where we compare the formation energies of several ordered $Ga_xAl_{1-x}As$ structures (see Fig. 3.2) as obtained by the present *ab initio* lattice gas model and by accurate DFT self-consistent calculations. Inspection of this table shows that truncation of the perturbative expansion of the total energy to the second order in the strength of the perturbation is a very good approximation. All formation energies in Table 3.1 are positive indicating that the system tends to segregate at low temperature. The calculation also shows that the $(GaAs)_1/(AlAs)_1$ (001) SL recently proposed[39] as possible equilibrium state of the alloy at high temperature is actually the *less* stable among the $x = 0.5$ ordered structures considered, the most stable being the (111) SL, followed by chalcopyrite. All the ordered structures are, in turn, unstable with respect to the random alloy of corresponding composition that is, no doubt, the equilibrium state at high temperature, where it is also favoured by entropy. As for the relative stability of the different ordered structures, our results agree with the similar calculations in Ref. 25, but somewhat differ in the numerical values of their formation energies, which are systematically higher (more positive) in our calculations. The main source of this discrepancy is the better sampling used here for BZ integration: ten points[15] in the irreducible wedge

Structure	DFT	DFPT
$Ga_1Al_3As_4$ Luzonite	6.36	6.36
$Ga_3Al_1As_4$ Luzonite	6.36	6.36
$Ga_1Al_3As_4$ Famatinite	6.25	6.25
$Ga_3Al_1As_4$ Famatinite	6.25	6.25
$Ga_2Al_2As_4$ Chalcopyrite	8.30	8.26
$Ga_1Al_1As_2$ (001) SL	8.57	8.46
$Ga_1Al_1As_2$ (111) SL	6.60	6.62
$Ga_{0.5}Al_{0.5}As$ Random	—	6.32

Table 3.1: Comparison between the formation energies of several $GaAlAs$ ordered structures calculated by full self-consistent calculations (DFT) and by interatomic interaction constants obtained from perturbation theory (DFPT). The formation energy of the random alloy as obtained from the interatomic interaction constants is also reported for comparison. Energies are in meV/cation.

of the zincblende structure, as compared with the two used in Ref. 25. The use of a different method in the self-consistent solution of the Kohn-Sham equations (LAPW[17] instead of the pseudopotential method used here) has only minor effects. Good agreement is found between our estimate for the formation energy of the random alloy and a "direct calculation" in a 64-atom supercell reported in Ref. 43. Reasonable agreement is also found with experimental determinations of the alloy "interaction parameter" $\Omega = 4\Delta\mathcal{E}_{\text{Random}}$: 0.6 Kcal/mole as compared with $0 \div 1.6$ from experiments.[37]

3.1.1 phase diagram and structural properties

We pass now to illustrate how the present method can be used to calculate thermodynamic properties by Monte Carlo (MC) simulations. We have performed constant-volume, constant chemical-potential MC simulations on a fcc supercell of linear dimensions 8 times larger than the primitive zincblende cell, thus containing 512 As atoms and 512 cations. We use the standard Metropolis algorithm with the elementary step given by an attempt to change the chemical nature of a given cation (reversing its $\sigma_{\mathbf{R}}$). This trial move is then accepted with probability given by the proper Boltzmann factor:

$$p = \min\left[\exp\left(-\frac{\Delta\mathcal{E}-\mu\Delta N_{Ga}}{k_BT}\right),\ 1\right], \tag{3.3}$$

where $\Delta\mathcal{E}$ is the variation of configurational energy due to the attempted move, ΔN_{Ga} the corresponding variation in the number of Ga atoms in the sample, μ is the chemical-

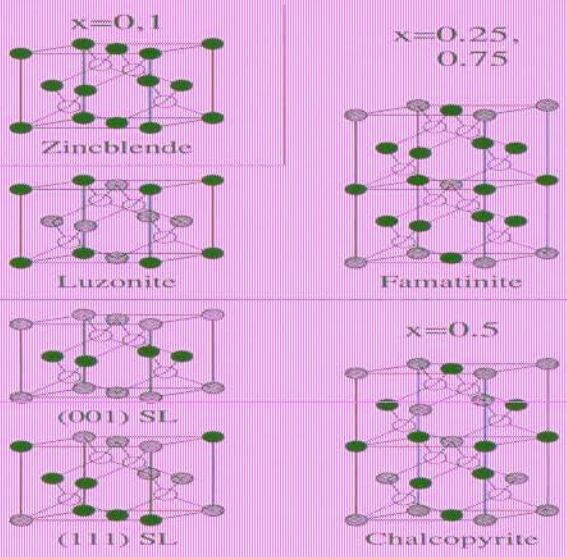

Figure 3.2: Crystal structures for the ordered $Ga_xAl_{1-x}As$ compounds considered in Table 3.1. Anion atoms are shown in white, cations in grey and black.

Luzonite
Famatinite
(001) SL
x=0.5
(111) SL
Chalcopyrite
Figure 3.2: Crystal structures for the ordered $Ga_xAl_{1-x}As$ compounds considered in Table 3.1. Anion atoms are shown in white, cations in grey and black.
27
Luzonite
Famatinite
(001) SL
x=0.5
(111) SL
Chalcopyrite

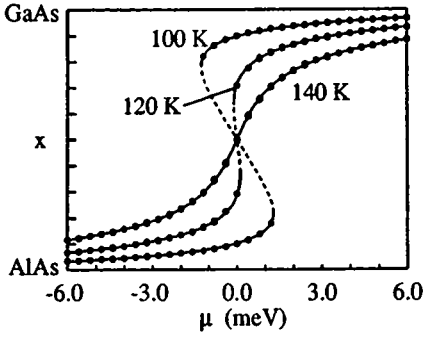

Figure 3.3: Average Ga concentration of $Ga_xAl_{1-x}As$ alloy as a function of chemical-potential for three different temperatures. The lines are obtained by a fitting procedure, as described in the text. The dashed portion of the lines at 100 and 120 K corresponds to the instability region inside the spinodal line.

potential (actually the difference between the Ga and Al chemical-potentials), T the simulation temperature and k_B the Boltzmann constant. For each considered temperature a sequence of chemical-potentials has been sampled in both directions; once starting from the $AlAs$-rich phase and increasing the chemical-potential, once starting from the $GaAs$-rich phase and decreasing it. For each value of μ a thousand MC step per site have been performed that was sufficient to equilibrate and have a small statistical error.

In Fig. 3.3 we display the average Ga concentration, x, as a function of the chemical-potential obtained for three different temperatures (above, below, and around the critical temperature, T_c). The statistical error is estimated to be smaller than the displayed full dots. Above T_c, the concentration is a continuous function of the chemical-potential, thus indicating complete miscibility for any concentration. As the temperature decreases below T_c, a discontinuity appears, which signals the opening of a miscibility gap. To estimate the coexistence concentrations below the critical temperature the free energies of the two phases ($GaAs$-rich and $AlAs$-rich) have to be compared. These can be obtained by integrating the chemical-potential with respect to the concentration (since $\mu = \partial F/\partial x$). To this end, the dependence of the chemical-potential upon concentration is fitted with the function

$$\mu(x) = k_B T \log\left(\frac{x}{1-x}\right) + \frac{dP(x)}{dx},$$

where $P(x)$ is a fourth-order polynomial which vanishes at $x = 1$ and $x = 0$, so that the correct high- and low-concentration limits are enforced.

The miscibility gap is then found corresponding to the values of chemical-potential where the two phases have the same free energy, whereas the maximum and minimum of $\mu(x)$ appearing below T_c correspond to the spinodal line, separating the region where

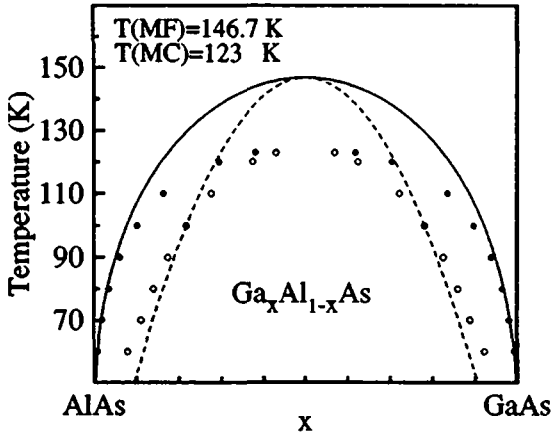

Figure 3.4: Phase diagram of $Ga_xAl_{1-x}As$ alloy. Circles: MonteCarlo predictions for miscibility gap (solid circles) and spinodal (open circles) lines. Lines: Mean-field predictions for the same lines (solid and dashed lines, respectively).

the alloy is metastable with respect to local concentration fluctuations and the region where it becomes unstable. This information is collected in Fig. 3.4 which shows the resulting phase diagram: full dots correspond to the miscibility gap, empty dots correspond to the spinodal line, as obtained from MC simulation. The mean-field (MF) results of the quasi-regular solution model are also displayed by a continuous and a dashed line (miscibility gap and spinodal lines respectively). Although the qualitative behaviour of the phase diagram comes out correctly, MF yields a higher critical temperature than MC. Actually, the fact that simple MF approximation seriously overestimates the transition temperature of simple 3-dimensional Ising hamiltonian is well established and can be used to assess the accuracy of the present MC calculation. In fact, coming back to Fig. 3.1, it is clear that the $Ga_xAl_{1-x}As$ alloy is equivalent, as far as energetics is concerned, to a 3-dimensional fcc Ising model with only nearest neighbour ferromagnetic interactions, but for small corrections due to more distant interactions. For this textbook case, the ratio of the true transition temperature and its MF estimate is known from high-temperature expansion to be 0.816. From our MC simulation we obtain 0.84 in reasonable agreement with this result. We conclude that our simulation conditions are adequate to locate within a few percent the critical temperature of our lattice-gas model and we expect this to be true in the general case.

From the results of Table 3.1 and the phase diagram of Fig. 3.4 it is clear that the equilibrium state of $Ga_xAl_{1-x}As$ at high temperature is the random alloy. To further clarify this point and detect possible deviations from randomness in the homogeneous alloy, let us examine the pair correlation function of the system at different

shell	$Ga_{\frac{1}{2}}Al_{\frac{1}{2}}As$				segregated alloy	(001) SL
	130 K	150 K	300 K	450 K		
0^{th}	1	1	1	1	1	1
1^{st}	0.19	0.13	0.05	0.03	1	-1/3
2^{nd}	0.11	0.06	0.01	0.00	1	1
3^{rd}	0.08	0.04	0.00	0.00	1	-1/3
4^{th}	0.07	0.03	0.00	0.00	1	1
5^{th}	0.06	0.02	0.00	0.00	1	-1/3
6^{th}	0.05	0.02	0.00	0.00	1	1

Table 3.2: Pair correlation function of $Ga_{\frac{1}{2}}Al_{\frac{1}{2}}As$ as obtained for several shells of neighbours by MC simulations at different temperatures above the critical one. Correlation functions of the segregated alloy and of the observed high-temperature ordered structure are also given for comparison.

temperatures above the miscibility gap. The pair correlation function is defined as:

$$C(\mathbf{R}) = < \sigma_{\mathbf{R}'} \sigma_{\mathbf{R}'+\mathbf{R}} > - < \sigma_{\mathbf{R}'} >^2, \tag{3.4}$$

where the average is performed over lattice sites and alloy configurations. In Table 3.2 the pair correlation functions of $Ga_{\frac{1}{2}}Al_{\frac{1}{2}}As$ at several temperatures as obtained by MC simulations are displayed. For comparison are also given the correlation functions of the segregated alloy and of the observed[39] high-temperature ordered structure. No thermodynamic tendency to order can be seen in the reported data. At low temperature, close to the critical temperature, a moderate tendency of the alloy to form clusters of like atoms is visible and expected, but already at room temperature the system is substantially random, and randomness keeps increasing with temperature. From the present investigation we can therefore conclude that the high-temperature ordered structure observed[39] in epitaxially grown $Ga_xAl_{1-x}As$ samples *is not* the equilibrium structure of the alloy at high temperature and is probably growth-induced.

3.2 SiGe

The binary Si_xGe_{1-x} alloy has long been believed to be a model random alloy at room temperature.[38] Recently, it has been observed[40] that Si_xGe_{1-x} displays long-range order along the (111) direction, when grown by Molecular Beam Epitaxy over a Si (001) substrate, at temperatures of the order of 700 K. Ordering was first attributed to the stabilizing effects of strain,[44] but it has been later observed also in unstrained samples.[45] Two are the structures compatible with the rhombohedral symmetry of the observed phase (denoted RH1 and RH2 and shown in Fig. 3.6) and they can be identified by the intensity pattern in the electron diffraction data. The most often observed structure[45,46,47] (RH2) is higher in energy (cfr. Table 3.3) thus suggesting that the ordering is not related to bulk thermodynamics, as already observed in Ref. 48. A *reversible* order/disorder phase transition has however been reported by some authors,[40] while other groups were unable to detect such a reversible transition.[45,48] To complete the rather confusing picture of the status of the experimental knowledge, we mention that a more complex situation has also been reported[46] where the ordered structure observed during growth (the RH2) is irreversibly destroyed by heating, whereas the RH1 structure appears and disappears reversibly by subsequent annealing cycles, and so would be of thermodynamic origin. Although interesting, this last conclusion has been contested even much recently by other experiments.[47]

In this section we readdress the question of the possible bulk thermodynamical origin of the ordered phase in Si_xGe_{1-x}. In this case the two pure materials have different lattice constants and atomic relaxation—microscopic and macroscopic—has to be taken into account. Following the arguments of Chapter 2, the formation energy of any alloy configuration, $C \equiv \{\sigma_{\mathbf{R}s}\}$, at a given volume Ω, can be written as

$$\Delta\mathcal{E}(\{\sigma_{\mathbf{R}s}\},\Omega) = \frac{1}{2}\sum_{s,s'}\sum_{\mathbf{R},\mathbf{R}'}\tilde{J}^{(\Omega)}_{ss'}(\mathbf{R}-\mathbf{R}')\sigma_{\mathbf{R}s}\sigma_{\mathbf{R}'s'} - \frac{N}{2}\sum_{s,s'}\sum_{\mathbf{R}}\tilde{J}^{(\Omega)}_{ss'}(\mathbf{R}) + x(\mathcal{E}_{Si}(\Omega)-\mathcal{E}_{Si}(\Omega_{Si})) + (1-x)(\mathcal{E}_{Ge}(\Omega)-\mathcal{E}_{Ge}(\Omega_{Ge})), \quad (3.5)$$

where the $\tilde{J}^{(\Omega)}$ are the interatomic interaction constants—at volume Ω—of the alloy, where microscopic relaxation is included (Eq. 2.21), $\mathcal{E}_{Si,Ge}(\Omega)$ are the energies of the pure materials as given by their equation of state and $\Omega_{Si,Ge}$ the corresponding equilibrium volumes; N is the number of elementary cells in the sample. The index s identifies different atoms inside the virtual-crystal diamond unit cell and $\sigma_{\mathbf{R}s} = \pm 1$ according to the atom (Si or Ge) that occupies the site $\mathbf{R}$ in s-th sublattice. The main differences with respect to the $Ga_xAl_{1-x}As$ case considered previously are the presence of the macroscopic elastic term (second row in Eq. 3.5) and the use of *relaxed*—volume dependent—interaction constants in the configurational term (first row in Eq. 3.5).

The technical ingredients of our calculations are as follows. We have used norm-conserving pseudopotentials[18,42] and a plane-wave basis-set up to a kinetic-energy cutoff of 12 Ry. The sum over BZ has been performed with six special points[15] in the irreducible wedge. The equilibrium lattice constants that we obtain for the two pure materials are 10.24 a.u. (exp. 10.26) and 10.63 a.u. (exp. 10.68) for silicon and germanium respectively, thus giving a relative lattice-mismatch of 3.7 % as compared with

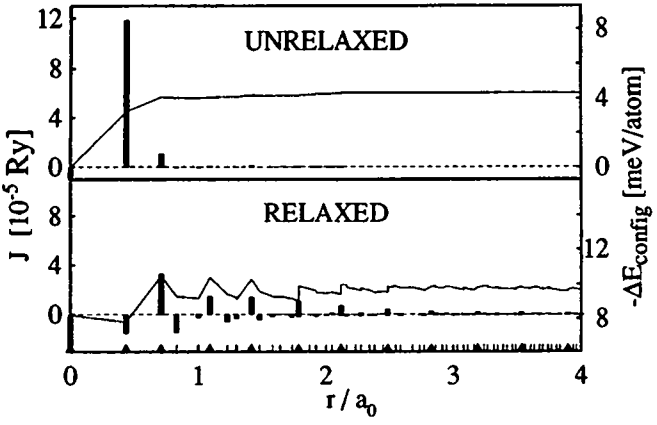

Figure 3.5: Atomic interaction constants calculated neglecting ('unrelaxed') and including ('relaxed') lattice relaxation, as functions of the interatomic separation. Thin vertical bars on the horizontal axis indicate shells of neighbors. Shells lying on the same bond chain as the atom at the origin are indicated by a solid triangle. The continuous line indicates the formation energy of the random alloy in the regular solution approximation, obtained by truncating the interaction at a given shell of neighbors

4.0 % from experiments. All the ingredients necessary to construct the interaction constants $\hat{J}$—the *unrelaxed* interaction constants J (Eq. 2.14), the harmonic force constants Φ (Eq. 2.17a), and the Kanzaki's forces $\mathbf{F}$ (Eq. 2.17b)—have been calculated in reciprocal space on a regular grid of points and Fourier-transformed to real space. Our reciprocal-space grid is such to allow the calculation of all these ingredients in real space up to the 22nd complete shell of neighbors, which is enough to get converged results. Once the J, Φ, and $\mathbf{F}$ have been obtained the $\hat{J}$ can be computed for arbitrary distances through Eq. 2.21.

In Fig. 3.5 we display the calculated interaction constants as functions of the interatomic distance, calculated at the lattice parameter given by Vegard's law for $x = \frac{1}{2}$. Neglecting lattice relaxation (upper panel), the interactions are very short-range as already seen in the case of $Ga_xAl_{1-x}As$. Lattice relaxation makes the interactions propagate rather far along the bond chains (lower panel). This happens in spite of the fact that also the Kanzaki's forces are very short-range and practically vanish beyond the second shell of neighbours. The reason for such a behaviour is that the harmonic force constants Φ tend to be rather long-range along the bond chains, as already recognized in Ref. 33, and the inversion process in Eq. 2.21 makes them even more long-range. The solid lines indicate the value of the formation energy of the random alloy, calculated using the regular-solution approximation and truncating the interac-

tion constants at different shells of neighbors. In the unrelaxed case the convergence is very rapid and few interaction constants suffice. When relaxation is included the convergence is slow and drops are observed in correspondence with shells belonging to the same bond chain as the atom at the origin. This indicates that a larger number of interaction constants have to be considered.

The ability of a perturbative calculation to reproduce the complete DFT result is examined in Table 3.3 where the configurational part of the formation energies for several ordered Si_xGe_{1-x} structures are compared, both neglecting (unrelaxed) and including (relaxed) atomic relaxation, with direct DFT calculations. All the reported energies are calculated at the lattice constant given by Vegard's law for $x = \frac{1}{2}$ and are negative since the positive contribution to Eq. 3.5 from the elastic term has not been included (and has been subtracted from the DFT calculations) in order to easily check the accuracy of the perturbative term in Eq. 3.5. Inspection of this table shows that the typical accuracy achievable by our approach is of the order of a few percent, thus giving confidence in its usefulness in the thermodynamical calculation. From this table we can also see that the observed RH2 structure is the *less* stable among the $x = 0.5$ ordered structure considered whereas the RH1 structure is more stable and actually *slightly* lower in energy than the random $Si_{\frac{1}{2}}Ge_{\frac{1}{2}}$ alloy. If macroscopic disproportion would be prevented, for instance because of the epitaxial constraint or due to a too low interdiffusion rate, the RH1 structure could become—at low enough temperature—stable with respect to the random alloy, but the corresponding ordering energy (a fraction of meV/atom, within the error bar of our calculation!) clearly indicates that the corresponding ordering temperature would be extremely small and that bulk thermodynamics is not responsible for any of the observed high-temperature ordered phases. Addition of the elastic term to the configurational formation energies of Table 3.3 makes all of them positive, so the equilibrium state at low temperature is given by the segregated compounds.

3.2.1 phase diagram

As in the *GaAlAs* case, we have investigated the thermodynamical properties of Si_xGe_{1-x} alloys by MC simulations. In this case, we have performed constant-pressure ($P = 0$), constant-chemical-potential MC simulations on a system of 1024 atoms (corresponding to an fcc supercell of linear dimensions 8 times larger than the primitive diamond cell). In our simulation a MC step is given by an attempt to change the chemical nature of a given atom (reversing its $\sigma_{\mathbf{R}_s}$) followed by an attempt to change the volume of the cell (of a random amount $\Delta\Omega$): to this end, interaction constants for an arbitrary volume are obtained by quadratic interpolation of the values calculated for three different volumes (near the equilibrium volumes of pure Si, pure Ge, and $Si_{\frac{1}{2}}Ge_{\frac{1}{2}}$, as given by Vegard's law). The two trial moves (alchemical and volumic) are made independently, the acceptance ratio of each being given by the proper Boltzmann factor:

$$p_A = \mathtt{min}\left[\, \exp\left(-\frac{\Delta\mathcal{E}_A - \mu\Delta N_{Si}}{k_B T}\right),\ 1\,\right], \tag{3.6a}$$

Structure	Unrelaxed		Relaxed	
	DFT	DFPT	DFT	DFPT
ZB	-6.5	-6.4	-6.5	-6.4
Si_3/Ge_2 (001)	-4.6	-4.6	-9.7	-9.4
Si_2/Ge_1 (001)	-3.9	-3.9	-6.4	-6.3
Si_1/Ge_2 (001)	-3.9	-3.9	-6.5	-6.3
Si_3/Ge_3 (001)	-3.2	-3.1	-9.5	-9.2
Si_3/Ge_2 (111) RH1	-5.7	-5.9	-10.0	-9.9
Si_3/Ge_2 (111) RH2	-2.5	-2.5	-6.3	-6.1
Si_3/Ge_3 (111)	-3.0	-2.9	-7.6	-7.9
Si_3/Ge_2 (110)	-2.7	-2.7	-10.7	-10.4
Si_2/Ge_1 (110)	-2.5	-2.5	-7.8	-7.5
Si_1/Ge_3 (110)	-2.5	-2.5	-7.9	-7.5
$Si_{0.5}Ge_{0.5}$ Random	—	-4.3	—	-9.7

Table 3.3: Comparison between the formation energies (at fixed volume) of several $SiGe$ superlattice structures, calculated by full self-consistent calculations (DFT) and by interatomic interaction constants obtained from perturbation theory (DFPT), both neglecting ("Unrelaxed"), and including ("Relaxed") lattice relaxation. The formation energy of the random alloy as obtained from the interatomic interaction constants is also reported for comparison. Energies are in meV/atom and all calculations are performed at the lattice constant given by Vegard's law for $x = \frac{1}{2}$. For the Si_3/Ge_2 (111) superlattices, the 'RH1' and 'RH2' labels refer to *Si-Ge—Ge-Si* and *Si-Si—Ge-Ge* layer stacking respectively (see also Fig. 3.6).

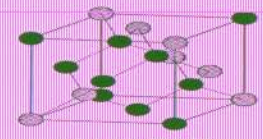

(111) RH1

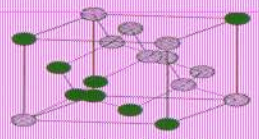

(111) RH2

Figure 3.6: Crystal structures of the two ordered Si_3/Ge_2 (111) superlattices with rhombohedral symmetry.

Structure	Unrelaxed		Relaxed	
	DFT	DFPT	DFT	DFPT
ZB	-6.5	-6.4	-6.5	-6.4
Si_3/Ge_2 (001)	-4.6	-4.6	-9.7	-9.4
Si_2/Ge_1 (001)	-3.9	-3.9	-6.4	-6.3
Si_1/Ge_2 (001)	-3.9	-3.9	-6.5	-6.3
Si_3/Ge_3 (001)	-3.2	-3.1	-9.5	-9.2
Si_3/Ge_2 (111) RH1	-5.7	-5.9	-10.0	-9.9
Si_3/Ge_2 (111) RH2	-2.5	-2.5	-6.3	-6.1
Si_3/Ge_3 (111)	-3.0	-2.9	-7.6	-7.9
Si_3/Ge_2 (110)	-2.7	-2.7	-10.7	-10.4
Si_2/Ge_1 (110)	-2.5	-2.5	-7.8	-7.5
Si_1/Ge_3 (110)	-2.5	-2.5	-7.9	-7.5
$Si_{0.5}Ge_{0.5}$ Random	—	-4.3	—	-9.7

Table 3.3: Comparison between the formation energies (at fixed volume) of several $SiGe$ superlattice structures, calculated by full self-consistent calculations (DFT) and by interatomic interaction constants obtained from perturbation theory (DFPT), both neglecting ("Unrelaxed"), and including ("Relaxed") lattice relaxation. The formation energy of the random alloy as obtained from the interatomic interaction constants is also reported for comparison. Energies are in meV/atom and all calculations are performed at the lattice constant given by Vegard's law for $x = \frac{1}{2}$. For the Si_3/Ge_2 (111) superlattices, the 'RH1' and 'RH2' labels refer to *Si-Ge—Ge-Si* and *Si-Si—Ge-Ge* layer stacking respectively (see also Fig. 3.6).

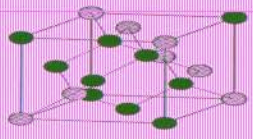

(111) RH1

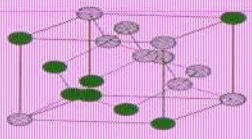

(111) RH2

Figure 3.6: Crystal structures of the two ordered Si_3/Ge_2 (111) superlattices with rhombohedral symmetry.

34

Structure	Unrelaxed		Relaxed	
	DFT	DFPT	DFT	DFPT
ZB	-6.5	-6.4	-6.5	-6.4
Si_3/Ge_2 (001)	-4.6	-4.6	-9.7	-9.4
Si_2/Ge_1 (001)	-3.9	-3.9	-6.4	-6.3
Si_1/Ge_2 (001)	-3.9	-3.9	-6.5	-6.3
Si_3/Ge_3 (001)	-3.2	-3.1	-9.5	-9.2
Si_3/Ge_2 (111) RH1	-5.7	-5.9	-10.0	-9.9
Si_3/Ge_2 (111) RH2	-2.5	-2.5	-6.3	-6.1
Si_3/Ge_3 (111)	-3.0	-2.9	-7.6	-7.9
Si_3/Ge_2 (110)	-2.7	-2.7	-10.7	-10.4
Si_2/Ge_1 (110)	-2.5	-2.5	-7.8	-7.5
Si_1/Ge_3 (110)	-2.5	-2.5	-7.9	-7.5
$Si_{0.5}Ge_{0.5}$ Random	—	-4.3	—	-9.7

Table 3.3: Comparison between the formation energies (at fixed volume) of several $SiGe$ superlattice structures, calculated by full self-consistent calculations (DFT) and by interatomic interaction constants obtained from perturbation theory (DFPT), both neglecting ("Unrelaxed"), and including ("Relaxed") lattice relaxation. The formation energy of the random alloy as obtained from the interatomic interaction constants is also reported for comparison. Energies are in meV/atom and all calculations are performed at the lattice constant given by Vegard's law for $x = \frac{1}{2}$. For the Si_3/Ge_2 (111) superlattices, the 'RH1' and 'RH2' labels refer to *Si-Ge—Ge-Si* and *Si-Si—Ge-Ge* layer stacking respectively (see also Fig. 3.6).

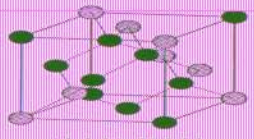

(111) RH1

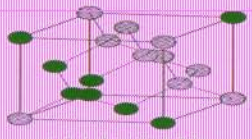

(111) RH2

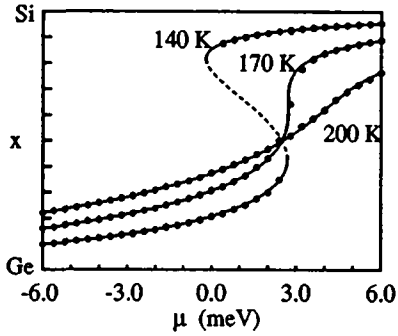

Figure 3.7: Average Si concentration of the alloy as a function of the chemical-potential, for three different temperatures. The lines are obtained by a fitting procedure, as described in the text. The dashed portion of the line at 140 K corresponds to the instability region inside the spinodal line.

$$p_V = \min\left[\exp\left(-\frac{\Delta\mathcal{E}_V + P\Delta\Omega}{k_B T}\right),\ 1\right], \tag{3.6b}$$

where $\Delta\mathcal{E}_{A,V}$ is the variation of the formation energy of the alloy due to the attempted (alchemical or volumic) move, ΔN_{Si} the corresponding variation in the number of Si atoms in the sample, μ is the chemical-potential (the difference between the Si and Ge chemical-potentials), P the pressure on the system ($P = 0$ in our case), T the simulation temperature and k_B the Boltzmann constant. For each considered temperature a sequence of chemical-potentials has been sampled in both directions; once starting from the Ge-rich phase and increasing the chemical-potential, once starting from the Si-rich phase and decreasing it. For each value of μ a thousand MC step per site have been performed.

In Fig. 3.7 we display the average Si concentration x as a function of the chemical-potential μ, obtained for three different temperatures (above, below, and at the critical temperature, T_c). The statistical errors are estimated to be smaller than the displayed full dots. The situation is very similar to the $Ga_xAl_{1-x}As$ case. Above T_c, the concentration is a continuous function of the chemical-potential and the two materials are miscible at all compositions. As the temperature decreases below T_c, a discontinuity appears and we have sudden jumps in the concentration when the chemical-potential is increased (decreased) at the lower (upper) edge of the unstable region. The main difference with respect to the $Ga_xAl_{1-x}As$ case considered above is that the dependence of the concentration x with respect to the chemical-potential μ is not symmetrical for $\mu \longrightarrow -\mu$. This is due to the volume dependence of the interaction constants $\hat{J}$ and of the elastic term in Eq. 3.5. The free energies of the Ge- and Si-rich phases are obtained by integration of the chemical-potential much in the same way as for $Ga_xAl_{1-x}As$ alloys. From the analytical expression of the free energy the miscibility gap and spinodal

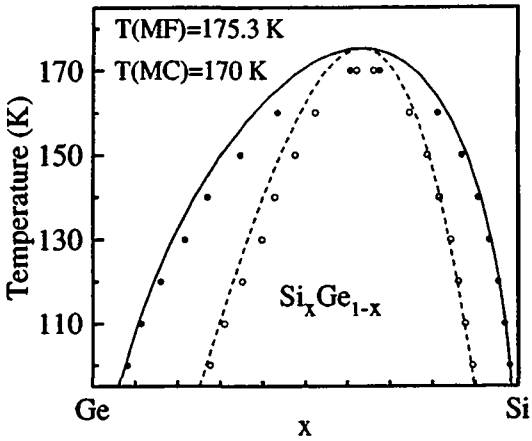

Figure 3.8: Phase diagram of SiGe alloys. Dots: Monte Carlo predictions for the miscibility gap (full) and spinodal (open) lines. Lines: Mean-field predictions for the same lines (full and dashed lines, respectively).

lines are obtained. The resulting phase diagram is drawn in Fig. 3.8, where full dots show the miscibility gap and empty dots the spinodal line as obtained by MC simulations. The asymmetry of the phase diagram reflects the asymmetric behaviour of $\mu(x)$. For comparison, the line of the miscibility gap and the spinodal line obtained by the mean-field (MF) approximation are also displayed by a continuous and a dashed line respectively. The value of T_c estimated by MC is $\approx$ 170 K, whereas MF gives 175.3 K. The two results are quite close—although MF overestimates T_c as expected—as the thermodynamics of the system is dominated by the (configuration independent) elastic contribution to the formation energy. Our results are at variance with previous cluster expansion calculations,[49] but they agree well with recent MC simulations employing semiempirical interatomic potentials.[50]

3.2.2 structural properties

MC simulations allow to study the structural properties of the alloy as a function of the chemical-potential and, hence, of the molar composition. In Fig. 3.9 we display our results for the bond-length distribution in Si_xGe_{1-x} alloys as obtained at $T = 300$ K. Similar results have been obtained at different temperature above T_c. The histogram in the left panel displays the bond-length distribution corresponding to an average composition $x = 0.45$, and shows three well distinct peaks, whose maxima are close to—but not coinciding with—the equilibrium bond-lengths of pure Si, pure Ge, and of zincblende $SiGe$ (reported on the right of the figure). In the right panel, we summarize

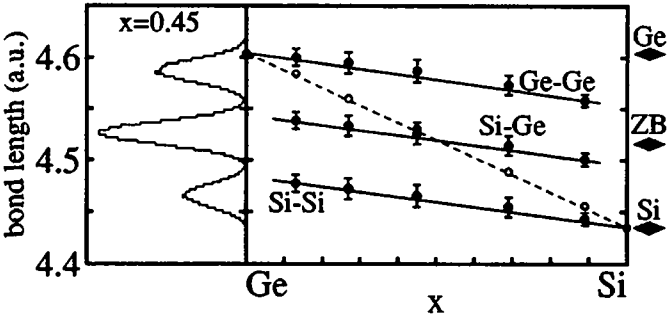

Figure 3.9: Left panel: bond-length distribution in $Si_{0.45}Ge_{0.55}$ alloy, measured by MC at $T = 300$ K. Right panel: dependence of maxima of the peaks upon Si concentration (full dots: the error bars indicate the width of the peaks); dependence upon composition of the average bond-length, as obtained from the alloy lattice parameter (open circles). The solid and dashed lines are intended as guidelines for the eyes. The diamonds on the right indicate the equilibrium bond-lengths of pure Si and Ge, and of zincblende $SiGe$

our results for different concentrations. Full dots indicate the maxima of the peaks, error bars their widths, and open circles indicate the average bond-length, as obtained by the lattice constant of the alloy. These data do not depend on temperature for any temperature above T_c, within our statistical errors, and they indicate that Vegard's law is followed very closely by the average lattice constant but not by the individual bond-lengths that, on the contrary, tend to remain close to their value in the corresponding pure material. The bond-length conservation predicted in our calculation has been very recently observed also in EXAFS experiments[51] and seems to be even more pronounced than found here. Deviations of the average lattice parameter from Vegard's law—as obtained for different temperatures in the range of $200 \div 400$ K—are displayed on a magnified scale in Fig. 3.10, along with the predictions of the quasi-regular solution approximation (continuous line). All the data coincide with the predictions of this approximation, indicating that Si_xGe_{1-x} is a random alloy already at these—and *a fortiori* at higher—temperatures.

To confirm this hypothesis, the pair correlation function, Eq. 3.4, for $Si_{\frac{1}{2}}Ge_{\frac{1}{2}}$ alloy, calculated at two temperatures above the miscibility gap, is reported in Table 3.4. For completeness, the correlation function of the segregated alloy and of the two observed[40] high-temperature ordered structures are also given. The $Si_{\frac{1}{2}}Ge_{\frac{1}{2}}$ pair correlation function shows very small values for all shells of neighbours—besides the on-site one—and does not indicate any tendency of the system to order and not even to form clusters of like atoms as was the case for $Ga_xAl_{1-x}As$ alloy. The figures quoted are extremely small and their precise value, although converged as for statistical error, can not be taken too seriously due to the other approximations in our calculations. The only important information that we can extract from these data is that Si_xGe_{1-x} alloy, just

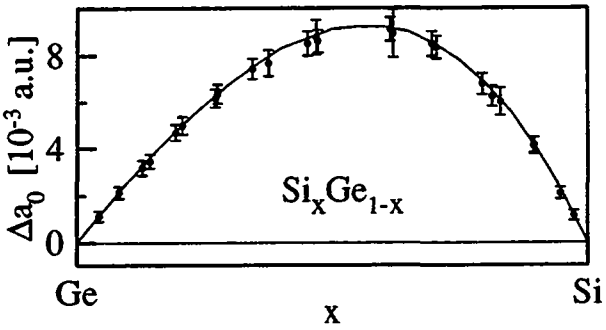

Figure 3.10: Deviation of the calculated alloy lattice parameter from linearity with respect to concentration (Vegard's law). MC results (obtained in the temperature range between 200 and 400 K) coincide with those predicted by the regular solution approximation (solid line), within statistical errors.

above the critical temperature, is already essentially random and becomes even more so increasing the temperature.

In conclusion our calculations show that bulk thermodynamics is not responsible for the ordering transitions observed in epitaxially grown samples at high temperature, thus supporting the kinetic and/or surface origin of such a phenomenon.

shell	$Si_{\frac{1}{2}}Ge_{\frac{1}{2}}$		segregated alloy	RH1	RH2
	200 K	400 K			
0^{th}	1	1	1	1	1
1^{st}	0.013	0.007	1	-1/2	1/2
2^{nd}	-0.020	-0.011	1	0	0
3^{rd}	0.013	0.007	1	1/2	-1/2
4^{th}	0.006	0.003	1	-1	-1
5^{th}	-0.007	-0.005	1	-1/2	1/2
6^{th}	0.000	0.000	1	0	0

Table 3.4: Pair correlation function of $Si_{\frac{1}{2}}Ge_{\frac{1}{2}}$ as obtained for several shells of neighbours by MC simulations at two different temperatures above the miscibility gap. Correlation functions of the segregated alloy and of the observed high-temperature ordered structures are also given.

Chapter 4

Lattice dynamics

In this chapter we study the vibrational properties of $Ga_xAl_{1-x}As$ and Si_xGe_{1-x} alloys. The two systems display quite different features. In the first case well defined dispersion relations, clearly related to the pure material ones, survive in the presence of disorder. In the second case it is not so: peaks are broadened and disappear and secondary features are present in addition to those deriving from bulk materials. In both cases the present supercell calculations compare well with available experimental data and help in their interpretation. From the computational point of view, the two systems are also different. The simple mass approximation is valid for $Ga_xAl_{1-x}As$ but not for Si_xGe_{1-x} and corrections beyond it are necessary. Moreover, mean-field calculations, that give resonable results in the pseudobinary alloy,[52-54] badly fail in the description of Si_xGe_{1-x} lattice dynamics.

4.1 GaAlAs

As a starting point for the investigation of the vibrational properties of complex $GaAlAs$ system let us consider the dispersion relations of their pure constituents. With the methods described in Chapter 2 the interatomic force constants (IFC's) of these simple semiconductors can be easily calculated and from them complete dispersion

	a (a.u.)		Z^*		ϵ_∞	
$GaAs$	10.60	(10.68)	2.07	(2.07)	12.3	(10.9)
$AlAs$	10.61	(10.69)	2.17	(2.18)	9.2	(8.2)

Table 4.1: Calculated equilibrium lattice parameters, a, Born effective charges, Z^*, and static dielectric constants, ϵ_∞, for $GaAs$ and $AlAs$. Experimental data (Ref. 55) are given in parentheses.

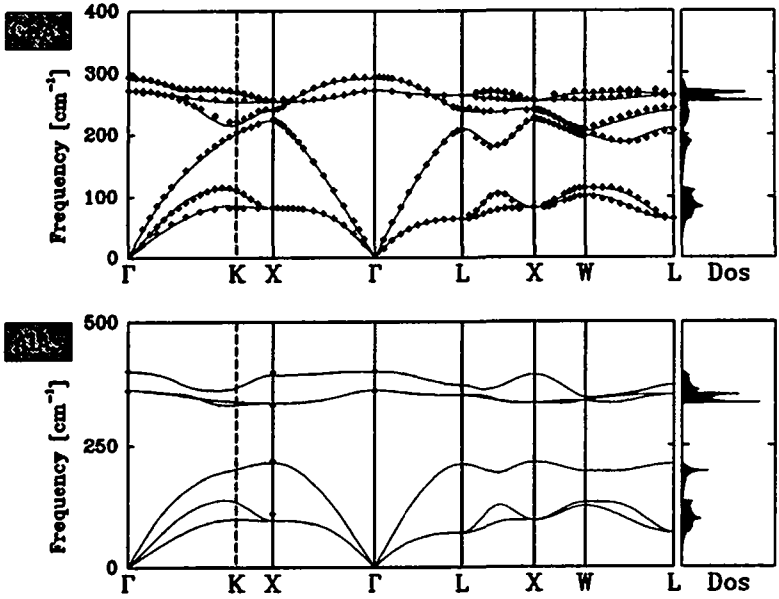

Figure 4.1: Calculated phonon dispersions and density of states of *GaAs* and *AlAs* binary semiconductors. Experimental data from Ref. 56 and 57 are also shown for comparison.

relations can be obtained. In Table 4.1 the equilibrium lattice parameters, as well as the calculated Born effective charges and dielectric constants, used in the force constants calculation, are listed. The analytic part of the interatomic force constants has been constructed to give correctly real space interactions up to the 9^{th} shell of neighbors. A 16 Ry kinetic energy cutoff in the plane-wave basis-set was sufficient to obtain a convergence in the phonon frequencies better than 5 cm^{-1}.

The results for the bulk phonon dispersions of *GaAs* and *AlAs* binary semiconductors along several symmetry lines together with the corresponding density of states are displayed in Fig. 4.1. Many neutron-diffraction and Raman scattering data[56] are available for *GaAs* but very little is known for *AlAs* for which only a few Raman experiments exist.[57] The agreement between calculations and available experiments is excellent for *GaAs* and gives confidence in our results in the case of *AlAs*, where a direct comparison with experiments is not really possible and the present calculation stands as a prediction of the full phonon dispersions.

In *GaAlAs* systems it has long been argued that the IFC's are independent of composition, and that, in particular, they are very similar in the two pure constituents. According to this *assumption*, the vibrational properties of any complex *GaAlAs* compound could be obtained constructing the dynamical matrix from the IFC's of one of the pure materials—*GaAs*, for instance—just inserting the atomic masses in the dy-

namical matrix according to the system of interest (mass approximation[30]). Empirical IFC's, fitted to the experimental phonon dispersions of *GaAs*, have therefore been extensively used to study the *AlAs* ones and those of mixed systems. Our calculation predicts, however, an *AlAs* longitudinal-optic (LO) branch along the Δ direction much flatter than hitherto suspected from empirical calculation based on mass approximation. This feature seems to be confirmed by the agreement between the calculations and the available experimental data at the X point.[57b] The reliability of those experimental data is however somewhat questionable, and the agreement perhaps fortuitous. A stronger indirect argument in favour of the reliability of the present prediction for *AlAs* comes from the similar behaviour obtained for the closely related *AlSb* system,[31] recently confirmed experimentally.[58]

The present result thus casts some doubts on the validity of the mass approximation even in the case of $Ga_xAl_{1-x}As$ systems. Actually, this is more a problem of empirical models than one of mass approximation itself. In fact, even a physically sound model as the Bond Charge Model (BCM)—that reproduces well the experimental *GaAs* dispersions with only 6 parameters—fails to reproduce correctly the atomic eigendisplacements at the X and L points.[56] Moreover, many different fits of the BCM—which describe equally well the observed vibrational spectrum of *GaAs*—turn out to yield rather different IFC's, and hence different results when used to calculate the spectrum of *AlAs*[59] (or of any mixed *GaAlAs* system). As a consequence, the accuracy of the IFC's derived from any model, even seemingly good, is rather questionable. It is worth noting that the vibrational eigendisplacements obtained from our calculations[31] are in good agreement with the available experiments[56] and the few previous *ab initio* calculations.[60,61]

4.1.1 validity of the mass approximation

We wish now to asses to which extent the mass approximation holds when *ab initio* IFC's are used to construct the dynamical matrices. To this end, we have calculated the phonon dispersions of *GaAs* and *AlAs* using the IFC's obtained for the other material. Our results are displayed in the left panel of Fig. 4.2, where the notation [A]→B indicates that phonons of material B have been obtained with the IFC's calculated for material A inserting the masses of material B in the dynamical matrices. We can see that in this case—where the two materials differ for the cationic species and have practically the same lattice parameter—the mass approximation gives phonon dispersions practically indistinguishable from the real ones in the acoustical and transverse-optic (TO) regions, while they differ by less than 10 cm^{-1} in the LO region. Such an accuracy is achieved without any empirical adjustment of the effective charges. In fact, the small residual discrepancies are almost entirely due to the small difference between the effective charges of the two materials. The validity of mass approximation is further confirmed by comparing lattice dynamical calculation for ideal ultrathin $(GaAs)_n/(AlAs)_n$ (001) superlattices, performed through fully self-consistent calculation,[29] or using the mass approximation with the bulk IFC's of the virtual crystal. The frequencies of the highest LO modes in the *GaAs*- and *AlAs*-like region of the spectrum for a few

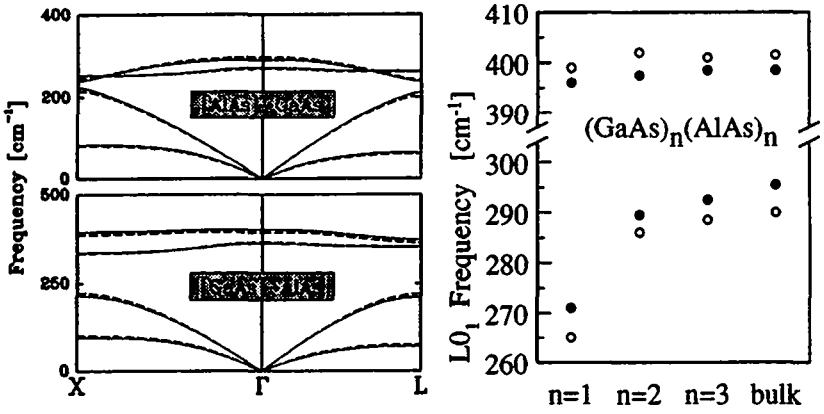

Figure 4.2: Left panel: Comparison between the phonon dispersions calculated with (dashed line) and without (full line) the mass approximation. The notation [A]→B indicates that phonon dispersions of material B have been obtained with the force constants appropriate to material A, just replacing the relevant masses. Right panel: $\omega_{LO_1}(\Gamma)$ in ideal $(GaAs)_n(AlAs)_n$ (001) superlattices: comparison between results of full *ab initio* calculations (full dots, after Ref. 29) and of calculations based on virtual-crystal force constants and the mass approximation (empty dots).

ultrathin superlattices are displayed in the right panel of Fig. 4.2. In practice, the only effect of the mass approximation is to lower (raise) *GaAs*- (*AlAs*-)like phonons modes much in the same way as in pure materials. Once this quasirigid shift is kept in mind in the comparison with experimental results, the mass approximation can be safely and conveniently used to study lattice dynamics of complex *GaAlAs* systems.

4.1.2 alloy dispersion relations

A long-debated problem is whether phonon states in semiconductor alloys can still be described in terms of well defined phonon dispersions, as they can in pure crystals. For $Ga_xAl_{1-x}As$ alloys, no neutron diffraction data exist which could assess the dispersive character of normal modes and the traditional tools of investigation are Raman and infrared spectroscopy which probe long-wavelength vibrations only. The Raman spectrum of $Ga_xAl_{1-x}As$ consists of two distinct peaks corresponding to the vibration of each cationic species separately. In the alloy, as a consequence of disorder, the peaks are shifted and broadened with respect to pure materials, with a rather asymmetric lineshape. This asymmetry has been interpreted assuming that Raman-active phonon modes are localized by disorder on a scale $\lesssim$100 Å[62] and that the $\mathbf{q} = 0$ wavevector selection rule, valid in the pure compounds, is relaxed due to disorder. Other experimental investigations,[63] however, indicate that LO phonons in $Ga_xAl_{1-x}As$ have

well defined momenta and are coherent over much longer distances. The band picture of the phonon modes has been confirmed and extended by Raman experiments on $Ga_xAl_{1-x}As/AlAs$ superlattices:[52] Raman peaks corresponding to phonons confined in the alloy region display a well defined dependence upon confinement order, which is a direct evidence of the dispersive character of lattice vibrations in the alloy.

To clarify this issue the vibrational properties of $Ga_xAl_{1-x}As$ alloys have been studied using the virtual-crystal IFC's and the mass approximation to build approximate dynamical matrices. The disordered alloys have been simulated by cubic supercells whose linear dimensions are four times the lattice parameter of the bulk alloy, thus containing 512 atoms. For any given composition x, cations are randomly assigned the Ga mass with probability x, and the Al mass with probability $(1-x)$. The dynamical matrix, constructed at the center of the supercell BZ, is straightforwardly diagonalized and the calculated physical quantities are averaged over five different cationic configurations to reduce numerical noise.

Raman spectroscopy is the main source of experimental information in $Ga_xAl_{1-x}As$ alloys. Off resonance, the Raman cross section, σ_{Raman}, is given essentially by the derivative of the macroscopic polarizability of the system with respect to the vibrational normal coordinates:

$$\sigma^{IF}_{Raman}(\omega) \propto \sum_{\nu} \delta(\omega^2 - \omega_\nu^2) \left| \hat{\epsilon}^{F*} \cdot \frac{\partial \chi}{\partial q_\nu} \cdot \hat{\epsilon}^{I} \right|^2 , \tag{4.1}$$

where $\hat{\epsilon}^{I,F}$ are the polarizations of the incoming and diffused photons, χ is the polarizability tensor, q_ν the normal coordinate of the ν-th mode, and ω_ν the corresponding frequency. The derivative of the polarizability is given by: $\partial\chi/\partial q_\nu = \sum_{\mathbf{R},s,\gamma} \partial\chi/\partial u_{\mathbf{R}s\gamma} \times \partial u_{\mathbf{R}s\gamma}/\partial q_\nu$, where $u_{\mathbf{R}s\gamma}$ is the γ-th component of the displacement of the s-th atom in the unit cell identified by the lattice vector $\mathbf{R}$. Neglecting the difference of atomic polarizability of the two kinds of cations, the symmetry of the system—for what concern the polarizability—becomes tetrahedral as in pure materials and one obtains for the derivative: $\partial\chi_{\alpha\beta}/\partial u_{\mathbf{R}s\gamma} = P(-)^s |e_{\alpha\beta\gamma}|$, where P is a material dependent constant, and $e_{\alpha\beta\gamma}$ the Levi-Civita tensor. Substituting this expression in Eq. 4.1 one obtains:

$$\sigma^{IF}_{Raman}(\omega) \propto \sum_{\nu} \frac{\delta(\omega-\omega_\nu)}{\omega_\nu} \left| \sum_{\alpha\beta\gamma} \hat{\epsilon}^{F*}_\alpha \hat{\epsilon}^{I}_\beta |e_{\alpha\beta\gamma}| \cdot \left(\sum_{\mathbf{R},s} (-1)^s \frac{\partial u_{\mathbf{R}s\gamma}}{\partial q_\nu} \right) \right|^2 , \tag{4.2}$$

where $\partial u/\partial q$ is simply related to the eigenvectors of the dynamical matrix. Note that the equal polarizability approximation adopted here yields an expression for the Raman cross section similar to the one appropriate for the pure compounds. In particular, the $\mathbf{q} = 0$ selection rule is expected to be still valid in the approximation considered. In actual calculations, the δ function appearing in Eq. 4.2 as well as in other similar expressions, is substituted by a gaussian: $\delta(\omega) \approx \frac{1}{\sqrt{2\pi\sigma^2}} \exp\left(-\frac{\omega^2}{2\sigma^2}\right)$, where we have chosen $\sigma^2 = 2\ \mathrm{cm}^{-2}$.

In order to discuss the band picture in the alloy, let us define the (momentum resolved) spectral densities of states (SDOS):

$$n_\alpha(\mathbf{q},\omega) = \sum_{\nu,s} \delta(\omega-\omega_\nu) \left| \langle \mathbf{q},\alpha,s|\xi_\nu\rangle \right|^2 , \tag{4.3}$$

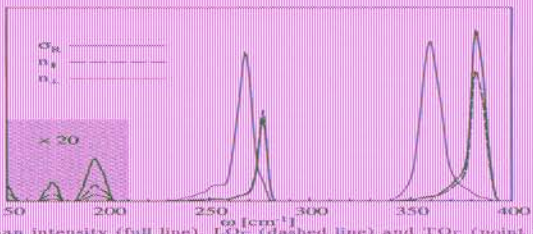

Figure 4.3: Raman intensity (full line), LO_Γ (dashed line) and TO_Γ (point line) spectral densities of states of $Ga_xAl_{1-x}As$. The data below 210 cm^{-1} are magnified by a factor 20.

where the ξ's are eigenvectors of the dynamical matrix, and $|\mathbf{q}, \alpha, s\rangle$ is a normalized vector representing a mode of wavevector $\mathbf{q}$ where the s-th atom of the unit cell moves along the α direction. An appropriate choice of the α directions gives the *longitudinal* ($\parallel$) and *transverse* ($\perp$) SDOS. In the absence of disorder, the SDOS are sums of delta functions centered at the appropriate normal frequencies with definite momentum $\mathbf{q}$. When disorder is present, $\mathbf{q}$ is no longer conserved: in case it is *approximately* so, the δ-like peaks are simply broadened and shifted; otherwise the peak structure is completely lost and normal modes are not characterized by any definite momentum.

In Fig. 4.3 we report the Raman cross section appropriate for the (001) backscattering geometry and the longitudinal and transverse spectral densities of states at $\mathbf{q} = 0$ calculated for $Ga_{.4}Al_{.6}As$. As expected the Raman intensity is very closely approximated by the longitudinal SDOS. The asymmetry of the Raman profile experimentally observed is reproduced by our calculation, showing that the release of the $\mathbf{q} = 0$ selection rule—invoked in Ref. 62 to explain the experimental findings—is not really necessary. The asymmetry in the Raman profile simply reflects the asymmetry in the longitudinal SDOS that, in turn, is a consequence of the form of the LO dispersions around Γ in the pure materials. The longitudinal SDOS at Γ originates essentially from the zone-center phonons of the pure materials. Off-center phonons—that have lower frequencies—can acquire a small $\mathbf{q} = 0$ component due to disorder and thus contribute to broaden the low-frequency side of the peaks giving raise to the observed asymmetry. Slightly below 200 cm^{-1}, in the region of Disorder-Activated Longitudinal Acoustic (DALA) modes, some very weak structure is present in the calculated spectrum. The relative intensity is however much weaker than observed experimentally, indicating that light scattering by DALA modes is enhanced by electronic resonance processes which are neglected here.

densities of states of $Ga_xAl_{1-x}As$. The data below 210 cm^{-1} are magnified by a factor 20.

where the ξ's are eigenvectors of the dynamical matrix, and $|\mathbf{q}, \alpha, s\rangle$ is a normalized vector representing a mode of wavevector $\mathbf{q}$ where the s-th atom of the unit cell moves along the α direction. An appropriate choice of the α directions gives the *longitudinal* ($\parallel$) and *transverse* ($\perp$) SDOS. In the absence of disorder, the SDOS are sums of delta functions centered at the appropriate normal frequencies with definite momentum $\mathbf{q}$. When disorder is present, $\mathbf{q}$ is no longer conserved: in case it is *approximately* so, the δ-like peaks are simply broadened and shifted; otherwise the peak structure is completely lost and normal modes are not characterized by any definite momentum.

In Fig. 4.3 we report the Raman cross section appropriate for the (001) backscattering geometry and the longitudinal and transverse spectral densities of states at $\mathbf{q} = 0$ calculated for $Ga_{.4}Al_{.6}As$. As expected the Raman intensity is very closely approximated by the longitudinal SDOS. The asymmetry of the Raman profile experimentally observed is reproduced by our calculation, showing that the release of the $\mathbf{q} = 0$ selection rule—invoked in Ref. 62 to explain the experimental findings—is not really necessary. The asymmetry in the Raman profile simply reflects the asymmetry in the longitudinal SDOS that, in turn, is a consequence of the form of the LO dispersions around Γ in the pure materials. The longitudinal SDOS at Γ originates essentially from the zone-center phonons of the pure materials. Off-center phonons—that have lower frequencies—can acquire a small $\mathbf{q} = 0$ component due to disorder and thus contribute to broaden the low-frequency side of the peaks giving raise to the observed asymmetry. Slightly below 200 cm^{-1}, in the region of Disorder-Activated Longitudinal Acoustic (DALA) modes, some very weak structure is present in the calculated spectrum. The relative intensity is however much weaker than observed experimentally, indicating that light scattering by DALA modes is enhanced by electronic resonance processes which are neglected here.

46

densities of states of $Ga_xAl_{1-x}As$. The data below 210 cm^{-1} are magnified by a factor 20.

where the ξ's are eigenvectors of the dynamical matrix, and $|\mathbf{q}, \alpha, s\rangle$ is a normalized vector representing a mode of wavevector $\mathbf{q}$ where the s-th atom of the unit cell moves along the α direction. An appropriate choice of the α directions gives the *longitudinal* ($\parallel$) and *transverse* ($\perp$) SDOS. In the absence of disorder, the SDOS are sums of delta functions centered at the appropriate normal frequencies with definite momentum $\mathbf{q}$. When disorder is present, $\mathbf{q}$ is no longer conserved: in case it is *approximately* so, the δ-like peaks are simply broadened and shifted; otherwise the peak structure is completely lost and normal modes are not characterized by any definite momentum.

In Fig. 4.3 we report the Raman cross section appropriate for the (001) backscattering geometry and the longitudinal and transverse spectral densities of states at $\mathbf{q} = 0$ calculated for $Ga_{.4}Al_{.6}As$. As expected the Raman intensity is very closely approximated by the longitudinal SDOS. The asymmetry of the Raman profile experimentally observed is reproduced by our calculation, showing that the release of the $\mathbf{q} = 0$ selection rule—invoked in Ref. 62 to explain the experimental findings—is not really necessary. The asymmetry in the Raman profile simply reflects the asymmetry in the longitudinal SDOS that, in turn, is a consequence of the form of the LO dispersions around Γ in the pure materials. The longitudinal SDOS at Γ originates essentially from the zone-center phonons of the pure materials. Off-center phonons—that have lower frequencies—can acquire a small $\mathbf{q} = 0$ component due to disorder and thus contribute to broaden the low-frequency side of the peaks giving raise to the observed asymmetry.

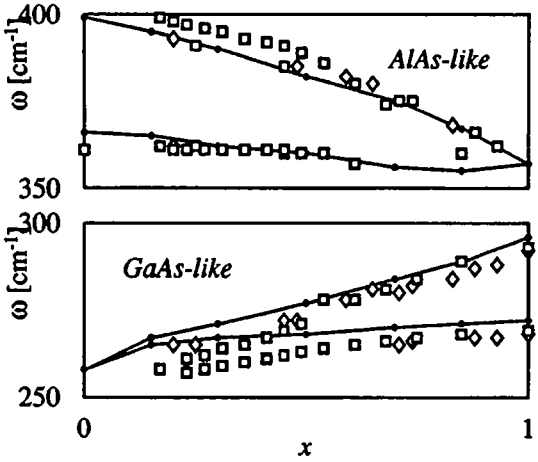

Figure 4.4: Dependence of the LO_Γ and TO_Γ peaks of $Ga_xAl_{1-x}As$ upon molar composition, x. Experimental data are indicated by squares (from Ref. 64) and diamonds (from Ref. 65).

In Fig. 4.4 we display the position of the TO and LO peaks as functions of the molar composition, x. The LO peaks depend more on composition than the TO ones, and they both tend to a same value extreme diluted limit. The agreement with experiments is good, and of the same order as that between different sets of experimental data. We note that the agreement of the present results with experiments could even be improved if they were corrected according to the difference between the pure-material frequencies calculated with and without the mass approximation.

Fig. 4.5 shows the longitudinal and transverse SDOS along the Δ direction for $x = \frac{1}{2}$. The spectral resonances—whose width is of the order of 10 cm^{-1}—move as the wavevector q varies in the BZ. The position of the peaks is indicated by the solid lines in the ωq plane. The main effects of alloying are the broadening and shift of the peaks, and a modulation of their intensity. In the acoustic region, the dispersive character of lattice vibrations is quite evident. In the optic region, it is less so due to the narrowness of the phonon branch, whose width may be comparable with that of the resonance. The resonances are however sufficiently narrow to allow one to assign a well defined position to the peaks, as the wavevector moves in the BZ. The most favorable situation is met for *GaAs*-like LO modes, in the *Ga*-rich regime, where one has a large bandwidth ($20 \div 50$ cm^{-1}) and a small resonance width ($\lesssim 5 cm^{-1}$). As the *Ga* concentration increases, the bandwidth increases and the resonance narrows, thus making the dispersive character more evident. This has been observed also experimentally in Raman spectra of *GaAlAs/AlAs* superlattices.[52]

In Fig. 4.6 we report the phonon dispersions of $Ga_{\frac{1}{2}}Al_{\frac{1}{2}}As$ along the Δ (Γ–X) and Λ (Γ–L) lines, for three different concentrations. For $x = \frac{1}{2}$ the dash-dotted line indicates the position of the maxima of the SDOS, whereas the shaded area—which is centered

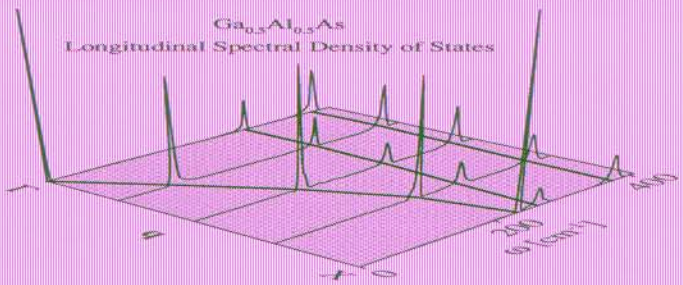

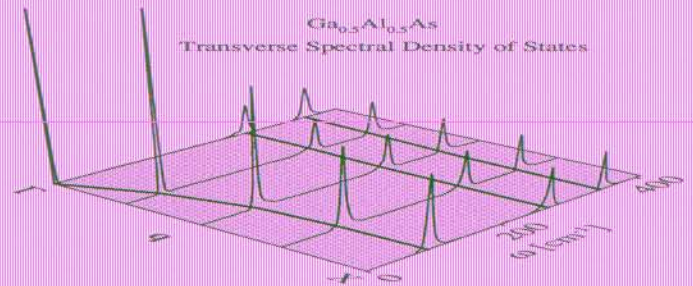

Figure 4.5: Spectral densities of states of $Ga_{\frac{1}{2}}Al_{\frac{1}{2}}As$ along the Δ direction. The positions of the peaks are indicated by the solid lines in the ωq plane.

Γ q Γ

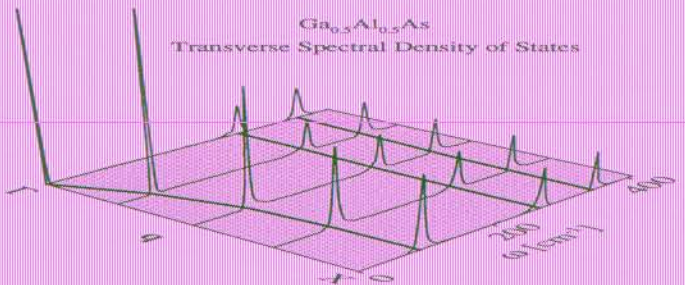

Figure 4.5: Spectral densities of states of $Ga_{\frac{1}{2}}Al_{\frac{1}{2}}As$ along the Δ direction. The positions of the peaks are indicated by the solid lines in the ωq plane.

48

Γ q Γ

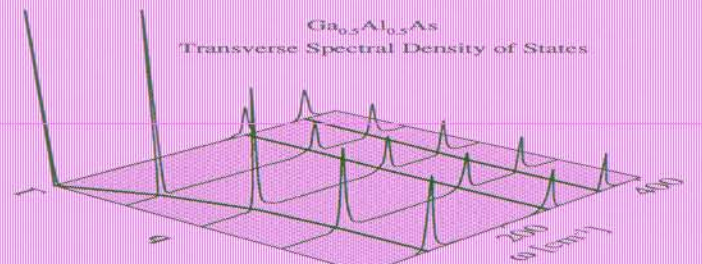

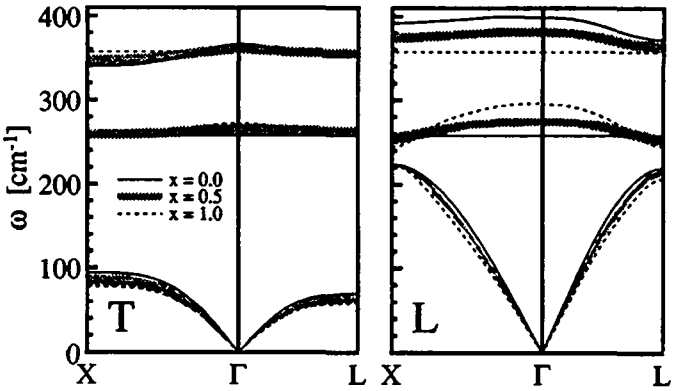

Figure 4.6: Transverse (left panel) and longitudinal (right panel) phonon dispersion of $Ga_{\frac{1}{2}}Al_{\frac{1}{2}}As$ along the Δ and Λ line. For $x = \frac{1}{2}$ the dash-dotted line indicates the position of the maxima of the SDOS, whereas the shaded area shows the width of the peaks at each **q**.

around the average frequency of the line—shows the width of the peaks at each **q**. Note that the maximum and average frequencies do not coincide, because of line asymmetry. Alloying has little effect on the acoustic branches, which are already very close in the *GaAs* and *AlAs* pure materials. Optic bands are narrowed with respect to the pure-material limit, as a consequence of dilution (in the extremely diluted limit, each band collapses into an isolated-impurity state). Longitudinal bands are lowered and—to a smaller extent—transverse bands raised, resulting in a smaller LO-TO splitting: in the extremely diluted limit, longitudinal and transverse modes are degenerate as a consequence of a vanishing macroscopic polarization. The dispersion of *AlAs*-like LO modes is very anisotropic, the width along the Λ direction being comparable with the LO-TO splitting at zone center, whereas the *AlAs*-like LO band along Δ direction—which is very flat already in pure *AlAs*—maintains its flatness upon alloying and shifts almost rigidly with concentration. This fact is relevant for the structural characterization of interfaces in *GaAs/AlAs* (001) superlattices. In fact, if a superlattice deviates from ideality and presents some cationic intermixing it can be seen as a modulated alloy in the (001) direction and the frequency of the topmost *AlAs*-like LO mode provides a lower bound for the *Ga* concentration in the *purest Al* plane. Moreover, when two adjacent cationic planes have sufficiently different *Al* concentrations—such that the corresponding bulk-alloy *AlAs*-like frequencies differ more than the LO bandwidth—then the corresponding *AlAs*-like vibrations do not penetrate in the adjacent plane and their distinct frequencies—detectable by Raman spectroscopy—are a direct measure of their composition. Due to the flatness of the *AlAs*-like LO band in the Δ direction, this happens whenever the composition difference between neighboring cationic planes corresponds to a frequency difference in the bulk-alloy *AlAs*-like Raman frequency of more than 3-4 cm^{-1} and can provides useful information on the actual composition profile of nominally ideal superlattices.[66]

4.2 SiGe

Unlike the case of $Ga_xAl_{1-x}As$ presented above, in Si_xGe_{1-x} the two pure materials have different equilibrium lattice parameters and, as we have seen in Chapter 3, the different kinds of bonds in the alloy tend to keep the same length they have in the corresponding pure materials. As a consequence of this fact, in any complex $SiGe$ system, even at equilibrium, the atomic positions are displaced from the ideal ones of the pure materials and the effects of the local strain on the atoms have to be taken into account in the study of its vibrational properties. In the absence of experimental information on the effects of atomic relaxation, treatments of $SiGe$ complex systems with empirical models are quite groundless and in fact not much theoretical work has been done so far (and mainly at a *qualitative* level). With the methods introduced in Chapter 2 on the contrary, it is possible to study the effects of atomic relaxation on the lattice dynamics of complex systems and account for them—as well as for the effects of chemical disorder—in a natural way. In the following it will be demonstrated that the present approach leads to a quantitatively correct description of the lattice dynamical properties of $SiGe$ systems.

Let us start again our investigation by examining the dispersion relations of the pure materials. The structural equilibrium parameters obtained for the two materials are listed in Table 4.2. They slightly differ from those given in Chapter 3 due to the higher cutoff (16 Ry) used here in order to have phonon frequencies converged within 3 cm^{-1}. In Fig. 4.7 the phonon dispersions of pure Si and pure Ge under hydrostatic strain are shown. For both silicon and germanium the solid lines give the results for the crystal at equilibrium (zero pressure) and the comparison with available experimental data (diamonds) shows the accuracy of *ab initio* calculations. The dashed lines correspond to Si (Ge) hydrostatically expanded (compressed) to the Ge (Si) lattice constant. The dotted lines correspond to the intermediate lattice constant of a $Si_{\frac{1}{2}}Ge_{\frac{1}{2}}$ alloy in both cases. All the frequency shifts are in agreement with those that can be deduced from the experimental Grüneisen parameters[67] and are practically equal and opposite for the two materials when the difference in the atomic masses is taken into account. We note that the phonon dispersions *at equilibrium* are very much the same in the two

	a (a.u.)		B_0 (kBar)		B'	
Si	10.20	(10.26)	976	(992)	3.7	(4.15)
Ge	10.60	(10.68)	763	(768)	5.1	(4.59)

Table 4.2: Calculated equilibrium lattice parameters, a, bulk modulus, B_0, and its pressure derivative, B', for the elemental semiconductors. Experimental data (Ref. 55) are given in parentheses.

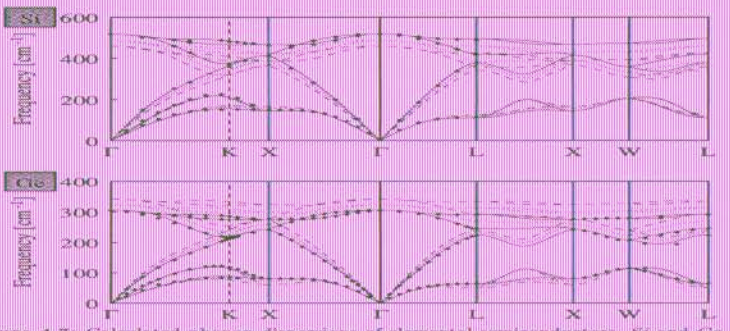

Figure 4.7: Calculated phonon dispersions of elemental semiconductors, *Si* and *Ge*, under hydrostatic strain. Solid lines correspond to the unstrained situation, dashed lines correspond to silicon (germanium) at the germanium (silicon) lattice constant. The dotted lines are calculated at the lattice constant of a $Si_{\frac{1}{2}}Ge_{\frac{1}{2}}$ alloy in both cases. Experimental data (diamonds) from Refs. 68 and 69

materials once they are scaled with the ratio of the corresponding plasma frequencies.

Similar results are obtained for the pure materials under other distortions[70] and show that the effect of strain can be as large as several tens of cm^{-1}. It is clear that it is not possible to find a unique set of IFC's that describe equally well all situations. Different strain conditions require different sets of IFC's. The effect of different chemical environment is less pronounced: the virtual-crystal IFC's under a given strain condition—after appropriate scaling with plasma frequencies—can describe quite well ($\approx$ 5 cm^{-1}) the lattice dynamics of the pure materials under the *same* distortion. So, at least for *SiGe* systems where the chemical difference between the two atoms is quite small (cfr. Chapter 3 and Ref. 71), a unique set of IFC's can describe the vibrational properties at *fixed* strain condition. Unfortunately this is of little help for the study of complex *SiGe* systems because in a real case one is interested in atomic configurations in which the chemical environment changes from site to site, and hence, due to the local atomic relaxation, the strain conditions change as well with position.

Figure 4.7: Calculated phonon dispersions of elemental semiconductors, *Si* and *Ge*, under hydrostatic strain. Solid lines correspond to the unstrained situation, dashed lines correspond to silicon (germanium) at the germanium (silicon) lattice constant. The dotted lines are calculated at the lattice constant of a $Si_{\frac{1}{2}}Ge_{\frac{1}{2}}$ alloy in both cases. Experimental data (diamonds) from Refs. 68 and 69

materials once they are scaled with the ratio of the corresponding plasma frequencies.

Similar results are obtained for the pure materials under other distortions[70] and show that the effect of strain can be as large as several tens of cm^{-1}. It is clear that it is not possible to find a unique set of IFC's that describe equally well all situations. Different strain conditions require different sets of IFC's. The effect of different chemical environment is less pronounced: the virtual-crystal IFC's under a given strain condition—after appropriate scaling with plasma frequencies—can describe quite well ($\approx$ 5 cm^{-1}) the lattice dynamics of the pure materials under the *same* distortion. So, at least for *SiGe* systems where the chemical difference between the two atoms is quite small (cfr. Chapter 3 and Ref. 71), a unique set of IFC's can describe the vibrational properties at *fixed* strain condition. Unfortunately this is of little help for the study of complex *SiGe* systems because in a real case one is interested in atomic configurations in which the chemical environment changes from site to site, and hence, due to the local atomic relaxation, the strain conditions change as well with position.

51

Figure 4.7: Calculated phonon dispersions of elemental semiconductors, *Si* and *Ge*, under hydrostatic strain. Solid lines correspond to the unstrained situation, dashed lines correspond to silicon (germanium) at the germanium (silicon) lattice constant. The dotted lines are calculated at the lattice constant of a $Si_{\frac{1}{2}}Ge_{\frac{1}{2}}$ alloy in both cases. Experimental data (diamonds) from Refs. 68 and 69

materials once they are scaled with the ratio of the corresponding plasma frequencies.

Similar results are obtained for the pure materials under other distortions[70] and show that the effect of strain can be as large as several tens of cm^{-1}. It is clear that it is not possible to find a unique set of IFC's that describe equally well all situations. Different strain conditions require different sets of IFC's. The effect of different chemical environment is less pronounced: the virtual-crystal IFC's under a given strain condition—after appropriate scaling with plasma frequencies—can describe quite well ($\approx$ 5 cm^{-1}) the lattice dynamics of the pure materials under the *same*

There is no simple satisfactory way to implement the nice scaling properties described above in the general case, and the problem has been solved introducing higher-order interatomic force constants (HIFC's).

4.2.1 testing higher-order interatomic force constants

	Silicon			Germanium		
	10.20	10.40	10.60	10.20	10.40	10.60
Γ_{LTO}	519 (517)	488 (487)	456 (458)	343 (342)	325 (321)	307 (303)
X_{TA}	136 (145)	152 (158)	166 (165)	60 (60)	74 (74)	85 (81)
X_{LOA}	414 (414)	391 (389)	367 (366)	273 (274)	260 (257)	245 (241)
X_{TO}	471 (466)	431 (425)	386 (386)	324 (324)	301 (296)	276 (273)
L_{TA}	103 (110)	114 (118)	123 (123)	49 (50)	58 (58)	65 (63)
L_{LA}	376 (378)	369 (368)	341 (342)	235 (237)	231 (230)	226 (223)
L_{TO}	497 (494)	462 (458)	424 (425)	334 (334)	314 (310)	293 (289)
L_{LO}	423 (419)	384 (379)	362 (358)	292 (293)	270 (266)	247 (243)

Table 4.3: Phonon frequencies calculated at high symmetry points Γ, X, L, for *Si* and *Ge* under hydrostatic strain. The considered lattice parameters are given in atomic units. In each case the first entry refers to the calculation with the higher-order IFC's, the second one (in parentheses) to the *ab initio* calculation.

As described in Chapter 2, one calculates the first order corrections to the virtual-crystal interatomic force constants due to the displacement of a virtual atom from its ideal position, $\Phi^{(1)}$, and to the substitution of a virtual atom with a *Si* (or *Ge*) one, $\mathbf{F}^{(1)}$, by fitting the IFC's of simple ordered structures obtained from first principles. In order to fit $\Phi^{(1)}$, the IFC's of virtual crystal under different homogeneous distortions are considered. In a cubic material there are only three independent homogeneous distortions and the choice adopted here has been: the hydrostatic strain and the isovolumic distortions in the (001) and (111) directions. As for $\mathbf{F}^{(1)}$, the IFC's of *Si*, *Ge* and zincblende *SiGe* with atoms frozen at the atomic positions of the virtual crystal have been fitted. All the resulting constraints—and the general symmetry constraints discussed in Chapter 2—have been imposed by least square minimization. The resulting HIFC's reproduce the *ab initio* results within 3-5 cm^{-1}, when used for the fitted structures. This is essentially the king of agreement one can reach between the *ab initio* calculation itself and the experimental results, when available.

To asses the reliability of the HIFC's so obtained their predictions must be checked against calculations performed in structures other than the fitted ones. This is done in Table 4.3 and Fig. 4.8. In Table 4.3 are compared the frequencies calculated *ab initio* and with the HIFC's for some high-symmetry points in *Si* and *Ge* under hydrostatic

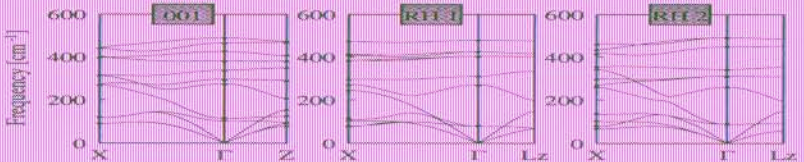

Figure 4.8: Calculated phonon dispersions of short-period Si_2/Ge_2 (001) and (111) superlattices. In the (111) direction two superlattices are possible—RH1 and RH2—depending on the layer stacking. Solid line are obtained with HIFC's, diamonds show the result of direct *ab initio* calculations.

strain. From this table we can see that the HIFC's reproduce the *ab initio* results within a few cm^{-1} over the whole range of distortions possible in the alloy, which corresponds to frequency shifts of several tens of cm^{-1}. Analogous results are obtained for the other strain conditions and the general description of the phonon dispersion relations is quite satisfactory. A more stringent test of the soundness of HIFC's is given by the results for short-period superlattices where the chemical environment is qualitatively diffe from the bulk case. To this end, some short-period superlattices lattice-matched to $Si_{\frac{1}{2}}Ge_{\frac{1}{2}}$ have been considered. The phonon dispersions of $(Si)_2/(Ge)_2$ superlattices grown in the (001) and (111) directions are shown in Fig. 4.8. In the (111) direction there are two unequivalent superlattices according to the stacking of the layers:[48] RH1 if the (111) bonds are homopolars (Si-Si or Ge-Ge), RH2 if they are heteropolars (Si-Ge). In Fig. 4.8 the solid line are given by HIFC's whereas diamonds indicate the results of *ab initio* calculation for high symmetry points. Also in this case the agreement is very good and hence one can conclude that HIFC's yield a safe approximation for the vibrational properties of complex $SiGe$ systems.

4.2.2 failure of mean-field approximations

Historically, the methods used to treat disordered systems rely on the idea that the alloy properties depend only locally on the atomic distribution and that one is interested only on their average value over the whole sample. Due to locality, the spatial average can be replaced by the average over all possible realizations of disorder and a periodic effective medium can therefore be introduced whose Green's function equals the *average* Green's function of the disordered system. In practice, the averaging process cannot be performed exactly, and one usually resorts to some kind of mean-field approximation, such as the Average T matrix Approximation (ATA),[72,73] or the Coher-

ap. matrix Approximation.

strain. From this table we can see that the HIFC's reproduce the *ab initio* results within a few cm^{-1} over the whole range of distortions possible in the alloy, which corresponds to frequency shifts of several tens of cm^{-1}. Analogous results are obtained for the other strain conditions and the general description of the phonon dispersion relations is quite satisfactory. A more stringent test of the soundness of HIFC's is given by the results for short-period superlattices where the chemical environment is qualitatively diffe from the bulk case. To this end, some short-period superlattices lattice-matched to $Si_{\frac{1}{2}}Ge_{\frac{1}{2}}$ have been considered. The phonon dispersions of $(Si)_2/(Ge)_2$ superlattices grown in the (001) and (111) directions are shown in Fig. 4.8. In the (111) direction there are two unequivalent superlattices according to the stacking of the layers:[48] RH1 if the (111) bonds are homopolars (Si-Si or Ge-Ge), RH2 if they are heteropolars (Si-Ge). In Fig. 4.8 the solid line are given by HIFC's whereas diamonds indicate the results of *ab initio* calculation for high symmetry points. Also in this case the agreement is very good and hence one can conclude that HIFC's yield a safe approximation for the vibrational properties of complex $SiGe$ systems.

4.2.2 failure of mean-field approximations

Historically, the methods used to treat disordered systems rely on the idea that the alloy properties depend only locally on the atomic distribution and that one is interested only on their average value over the whole sample. Due to locality, the spatial average can be replaced by the average over all possible realizations of disorder and a periodic effective medium can therefore be introduced whose Green's function equals the *average* Green's function of the disordered system. In practice, the averaging process cannot be performed exactly, and one usually resorts to some kind of mean-field approximation, such as the Average T matrix Approximation (ATA),[72,73] or the Coher-

ap. matrix Approximation.

strain. From this table we can see that the HIFC's reproduce the *ab initio* results within a few cm^{-1} over the whole range of distortions possible in the alloy, which corresponds to frequency shifts of several tens of cm^{-1}. Analogous results are obtained for the other strain conditions and the general description of the phonon dispersion relations is quite satisfactory. A more stringent test of the soundness of HIFC's is given by the results for short-period superlattices where the chemical environment is qualitatively diffe from the bulk case. To this end, some short-period superlattices lattice-matched to $Si_{\frac{1}{2}}Ge_{\frac{1}{2}}$ have been considered. The phonon dispersions of $(Si)_2/(Ge)_2$ superlattices grown in the (001) and (111) directions are shown in Fig. 4.8. In the (111) direction there are two unequivalent superlattices according to the stacking of the layers:[48] RH1 if the (111) bonds are homopolars (Si-Si or Ge-Ge), RH2 if they are heteropolars (Si-Ge). In Fig. 4.8 the solid line are given by HIFC's whereas diamonds indicate the results of *ab initio* calculation for high symmetry points. Also in this case the agreement is very good and hence one can conclude that HIFC's yield a safe approximation for the vibrational properties of complex $SiGe$ systems.

4.2.2 failure of mean-field approximations

Historically, the methods used to treat disordered systems rely on the idea that the alloy properties depend only locally on the atomic distribution and that one is interested only on their average value over the whole sample. Due to locality, the spatial

ent Potential Approximation (CPA),[72,74] where the alloy Green's function is expanded in terms of the single-impurity scattering T-matrix and the average is performed decoupling at different levels of accuracy the expansion. In the supercell (SC) approach, on the contrary, the averaging process is performed by *brute force*, by considering several random SC configurations whose properties are calculated directly. In trade of the much increased numerical work, this approach is exact in principle, the only (non-trivial) limitation being the size of the SC necessary to simulate a macroscopic sample of alloy. Recently, mean-field approximations have been widely used to study the vibrational properties of various $GaAlAs$ systems,[52-54] and their results are in reasonable agreement with those of the more sophisticated calculations presented above as well as with other supercell calculations.[54] In particular, the two-mode behavior of $Ga_xAl_{1-x}As$ alloys as well as the dispersive character of phonons are well described within single-site CPA.[52,53] By virtue of this success, the CPA is currently being used to study the effects of disorder in $SiGe$ superlattices.[75] In this section, single-site CPA and accurate SC calculations of the lattice dynamics of Si_xGe_{1-x} alloy are compared and it is shown that, far from being able to reproduce the fine details of superlattices spectra and at variance with the $Ga_xAl_{1-x}As$ case, mean-field approximations badly fail in the description even of the gross features of the vibrational properties of this binary alloy. SC calculations, on the contrary, compare well with available experiments and allows to clarify the microscopic origin of the observed spectral features. All the SC spectral functions presented below have been calculated with the accurate HIFC's introduced in the previous section and using cubic cells with 512 atoms. The results have been averaged over 6 random configurations and convoluted with a 2-cm^{-1} wide Lorentzian to reduce numerical noise. CPA calculations have been performed using the virtual-crystal interatomic force constants and neglecting atomic relaxation.

In Fig. 4.9 the vibrational density of states (DOS) of $Si_{\frac{1}{2}}Ge_{\frac{1}{2}}$ as obtained from SC calculations and from the CPA are compared. The general features of the DOS in the acoustic region (below ≈ 250 cm^{-1}) are well reproduced by the CPA, but for the loss of a few fine structures. In the optic region, the DOS is characterized by three well defined peaks which are interpreted as due to *Si–Si*, *Si–Ge*, and *Ge–Ge* vibrations (in order of decreasing frequency).[76,77] Some fine structures are also present, which are due to fluctuations in the local atomic environment (see below). In this region the CPA fails not only to reproduce these fine details (which is not surprising, due to the mean-field character of the CPA), but even to predict the existence of the *Si–Ge* peak. The relative intensity of the *Si–Si* and *Ge–Ge* peaks is also wrong, the latter being barely visible as a shoulder on top of a structureless background.

In Fig. 4.10 the Raman cross section, in the optical region, is displayed as obtained from SC and CPA calculations, neglecting the differences in the *Si* and *Ge* polarizabilities (Eq. 4.2). In agreement with experimental findings,[78] and as expected from inspection of the DOS, SC calculations predict the existence of three well defined Raman resonances, corresponding to *Si–Si*, *Si–Ge*, and *Ge–Ge* vibrations. The weak peaks in the region between the *Si–Ge* and *Si–Si* peaks are interpreted as due to the effect of different local atomic environment and will be discussed later. Here again, the *Si–Ge* peak is missing in the CPA, while the *Ge–Ge* one is barely visible.

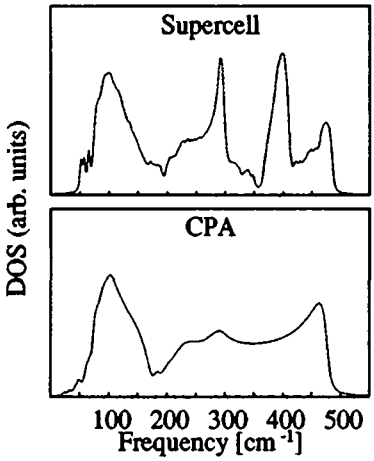

Figure 4.9: Vibrational Density of States of $Si_{\frac{1}{2}}Ge_{\frac{1}{2}}$ as obtained from SC (upper panel), and CPA (low panel) calculations.

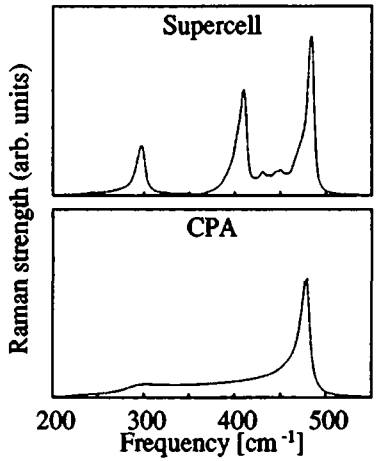

Figure 4.10: Raman cross section of $Si_{\frac{1}{2}}Ge_{\frac{1}{2}}$ as obtained from SC (upper panel), and CPA (lower panel) calculations.

The failure of single-site CPA can be traced back to a rather general feature of this approximation, as applied to alloy lattice-dynamical calculations, which does not appear to have been properly appreciated so far. The situation is already manifest in a simple model. Consider a crystal made of weakly interacting diatomic molecules, whose constituents are atoms of species A (mass m_A) with probability x and B (mass m_B) with probability $(1-x)$. Suppose that the intramolecular force constant, k, is independent of which atoms actually form the molecule, and that the intermolecular force constants can be neglected (i.e. that the separations among the optical peaks of the A_2, AB, and B_2 compounds are much larger than the typical bandwidths). Under these assumptions, the average Green's function of the system is:

$$\bar{g}(\omega) = \frac{x^2}{\mu_A\omega^2 - k} + \frac{(1-x)^2}{\mu_B\omega^2 - k} + \frac{2x(1-x)}{\mu_{AB}\omega^2 - k}, \tag{4.4}$$

where $\mu_A = \frac{1}{2}m_A$, $\mu_B = \frac{1}{2}m_B$, and $\mu_{AB} = m_Am_B/(m_A + m_B)$. The alloy DOS, at all concentrations, clearly displays three peaks corresponding to A–A, A–B, and B–B vibrations. In the CPA, atoms on a A_xB_{1-x} alloy are assigned an effective, frequency-dependent, mass which is determined by the condition that the T-matrix corresponding to the substitution of a single effective mass with a physical one vanishes on the average. Applying the CPA to this simple model, one would obtain:

$$g_{CPA}(\omega) = \frac{1}{\mu_{CPA}(\omega)\omega^2 - k}, \tag{4.5}$$

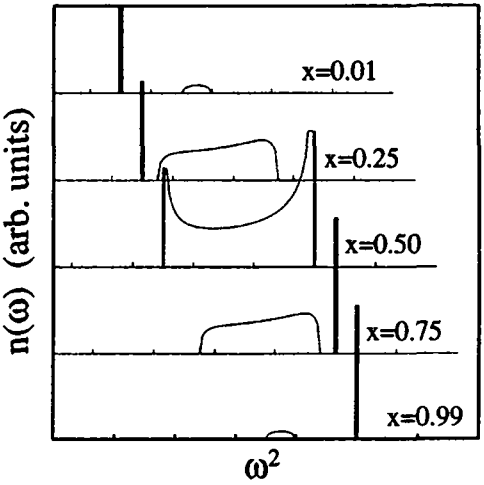

Figure 4.11: Density of states according to CPA for the model A_xB_{1-x} alloy described in the text ($m_A/m_B = 1/2$) for different concentrations, x.

where $\mu_{CPA}(\omega)$ solves the self-consistent equations

$$\mu_{CPA}(\omega) = \frac{\bar{\mu}_A\bar{\mu}_B\omega^2 - k(x\bar{\mu}_A + (1-x)\bar{\mu}_B)}{(x\bar{\mu}_B + (1-x)\bar{\mu}_A)\omega^2 - k}, \tag{4.6a}$$

$$\bar{\mu}_A = 2\mu_{CPA}m_A/(2\mu_{CPA} + m_A), \tag{4.6b}$$

$$\bar{\mu}_B = 2\mu_{CPA}m_B/(2\mu_{CPA} + m_B). \tag{4.6c}$$

The resulting density of states for $m_A/m_B = 1/2$ is displayed in Fig. 4.11. For $x \neq \frac{1}{2}$ the CPA DOS displays a single δ-like peak at the pure-component resonance of the majority band and a broad structure centered at the mixed-compound resonance, whose width vanishes in the high- and low-concentration limits. For $x = \frac{1}{2}$, one has instead two δ-like peaks corresponding to the two pure-component resonances and the broad structure covers the entire range in between. This very simple example retains the essential features of the full calculation (note the similarity of the $x = \frac{1}{2}$ DOS and the $Si_{\frac{1}{2}}Ge_{\frac{1}{2}}$ DOS of Fig. 4.9 in the optical region) and shows that mass disorder, though usually considered as site diagonal (and treated as such in the CPA) has in fact the same effect as off-diagonal disorder in that the vibrational properties are determined by the *bond force constant*, k divided by the square root of the product of the atomic masses. In the narrow-band limit, therefore, the alloy displays as many peaks as the number of different *bonds*, even though the interatomic force constants are not affected by disorder. CPA, instead, stresses the role of *atomic masses* and displays as many peaks as the number of different *atoms*. These considerations show also why the CPA can be successful in pseudobinary alloys such as *GaAlAs*. In this case, the anionic sublattice

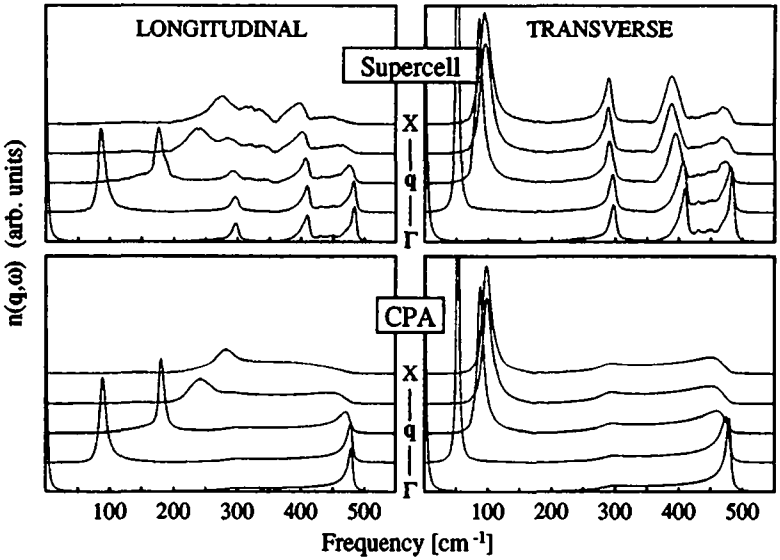

Figure 4.12: Spectral density of states of $Si_{\frac{1}{2}}Ge_{\frac{1}{2}}$ along the Δ direction, as calculated from SC's (upper panels) and by the CPA (lower panels).

is not affected by disorder and the number of different bonds is equal to the number of different cationic species on the disordered sublattice. In the case of binary alloys, on the contrary, the minimum requirement to obtain qualitatively correct vibrational properties is to consider explicitely at least the cluster of two atoms forming a bond.[79]

Let us now discuss the dispersive nature of lattice vibrations in Si_xGe_{1-x}. To this end, we consider the spectral density of states, $n(\mathbf{q},\omega)$, defined in Eq. 4.3. At zone center ($\mathbf{q} = 0$), $n(\mathbf{q},\omega)$ is closely related to the Raman cross section. The fact that the latter displays three well defined peaks would suggest that a well defined relation between frequencies and momenta exists in the alloy, as it is the case in $Ga_xAl_{1-x}As$. This is not the case here as it can be seen in Fig. 4.12 where $n(\mathbf{q},\omega)$ calculated for $Si_{\frac{1}{2}}Ge_{\frac{1}{2}}$ along the Δ (Γ–X) direction are reported. Let us discuss SC results first. At zone center, $n(\mathbf{q},\omega)$ shows three sharp peaks in addition to the acoustic one. Moving away from the Γ point, however, the *Si–Si* longitudinal peak looses its identity and disappears. The *Ge–Ge* longitudinal peak also disappears, merging into the acoustic band near zone border. The *Si–Ge* longitudinal peak remains defined, but it is substantially broadened. The transverse optical branches—which are much flatter and stay further apart from the acoustic one—seem to be less sensitive to disorder and remain well defined, but the same tendency to broaden or disappear is visible for the *Si–Ge* and *Si–Si* vibrations, respectively. As for the acoustic branches, their dispersive nature is

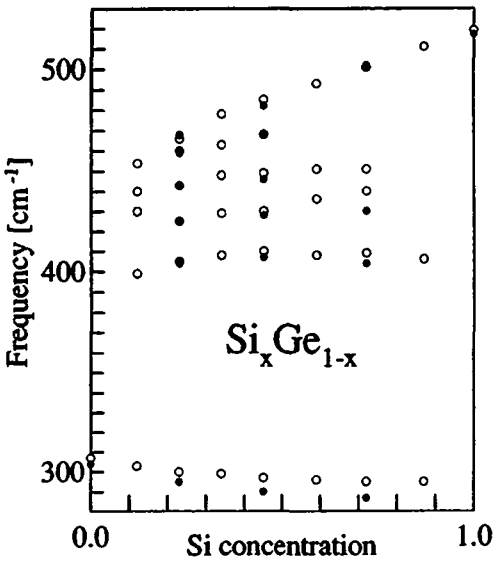

Figure 4.13: Composition dependence of the position of the Si_xGe_{1-x} Raman peaks. Results of our calculations (empty dots) are compared to experimental results (Ref. 78, full dots).

maintained in the alloy. Taken into account its already mentioned failure, the CPA reproduces some qualitative feature of the SC calculations as the dispersive nature of the acoustic branches and the tendency to disappear of the *Si–Si* optical peak, more evident in the longitudinal SDOS and less in the transverse one. As for the *Ge–Ge* and *Si–Ge* vibrations, CPA fails completely to describe their behaviour as one could already expect from the examination of the total DOS and Raman intensity.

4.2.3 effects of local atomic coordination

Early and recent Raman experiments[76–78] on Si_xGe_{1-x} alloys have revealed weak features in the frequency range between the *Si–Ge* and *Si–Si* main peaks. As we have seen, the same features are also predicted by the SC calculations. In Fig. 4.13 the dependence upon composition of the positions of the main and secondary Raman peaks is compared with experimental results. Good agreement is found between theory and experiments throughout the whole composition range. A fundamental question concerning these fine structures is their microscopic origin. The current interpretation of the weak peaks in the Raman cross section is that they are due to the fluctuations of the local atomic environment in the alloy,[77,78,80] but they have also been interpreted as signature of long-range order unintentionally present in the alloy.[81] In order to clarify

this issue, let us define a partial Raman cross section, decomposed according to the number of X atoms ($X = Si$ or Ge) vibrating at a given frequency and surrounded by a given number n of like atoms (cfr. Eq. 4.2):

$$\sigma^{IF}_{Raman}(\omega, \mathrm{X}_n) \propto \sum_{\nu} \frac{\delta(\omega - \omega_\nu)}{\omega} \left| \sum_{\alpha\beta\gamma} \hat{\epsilon}^{F*}_{\alpha} \hat{\epsilon}^{I}_{\beta} |e_{\alpha\beta\gamma}| \cdot \left(\sum_{\mathbf{R},s} (-)^s \mathbf{u}^{\nu}_{\mathbf{R},s\gamma} P_{\mathbf{R},s}(\mathrm{X}_n) \right) \right|^2 , \quad (4.7)$$

where $\epsilon^{I,F}$ are the polarizations of the incoming and outgoing photons, $e_{\alpha\beta\gamma}$ the Levi-Civita tensor, the u's are vibrational eigendisplacements, the $\mathbf{R}$'s sites of the FCC lattice, s atomic positions within an elementary cell ($s = 1, 2$), and $P_{\mathbf{R},s}(\mathrm{X}_n)$ is a weighting factor such that $P_{\mathbf{R},s}(\mathrm{X}_n) = 1$ if the $(\mathbf{R}, s)$ lattice site is occupied by an X atom surrounded by n like atoms, while $P_{\mathbf{R},s}(\mathrm{X}_n) = 0$ otherwise.

In the left panel of Fig. 4.14 we display $\sigma^{IF}_{Raman}(\omega, Si_n)$ and $\sigma^{IF}_{Raman}(\omega, Ge_n)$ calculated for $Si_{\frac{1}{2}}Ge_{\frac{1}{2}}$. Let us concentrate for the moment on the Si_n partial Raman cross that are the only non vanishing in the frequency region between Si-Ge and Si-Si main Raman peaks. It is easily recognized that different local configurations give rise to different shapes of the partial Raman cross section, thus confirming that the weak peaks are due to local fluctuations of the atomic coordination. The correspondence between local atomic configurations and fine structures in the Raman spectra is made more clear by examining those simple ordered structures that display homogeneously a single type of local coordination of the Si atoms. These special structures are the zincblende (ZB) structure for Si_0, the RH1 Si_2/Ge_2 (111) superlattice for Si_1, the Si_2/Ge_2 (001) superlattice for Si_2, the RH2 Si_2/Ge_2 (111) superlattice for Si_3, and the diamond structure (compressed to the alloy lattice constant) for Si_4. The same structures, with diamond Si obviously replaced by diamond Ge, also display a single type of local Ge_n coordination in exactly the same order as for the Si_n. The Raman cross section for these structures, spherically averaged over incoming and outgoing photon polarizations, is displayed in the right panel of Fig. 4.14. The Raman cross section of strained Ge is shown as dashed line. The close similarity of the superlattice spectra with the corresponding alloy Si_n partial Raman cross section in the 400-500 cm^{-1} frequency region further confirms the role played by the atomic coordination in the determination of these spectral features. The analysis of the peaks is now more easily done in the ordered structures. The frequencies of the modes are mainly determined by the type of bonds which stretch to first order in the phonon amplitude ('active bonds'). If one mode has only Si–Si active bonds, its frequency is very close to that of pure (strained) Si; if it has only Si–Ge active bonds its frequency is close to that of the ZB structure; if both types of bonds are active, the frequency is intermediate. The RH1 structure (corresponding to Si_1) has one doubly degenerate mode with only Si–Ge active bonds and a non degenerate mode in which all the bonds are active. The (001) superlattice (corresponding to Si_2) has three distinct peaks. The lowest-lying mode has only Si–Ge active bonds; in the highest lying mode only Si–Si bonds stretch; in the third mode all the bonds are active. The RH2 structure (corresponding to Si_3) has one doubly degenerate mode in which only Si–Si bonds stretch, and a non degenerate mode where all the bonds are active. The frequency of the 'intermediate' modes decreases with the number of like atoms, contrary to what was suggested in Ref. 78. The

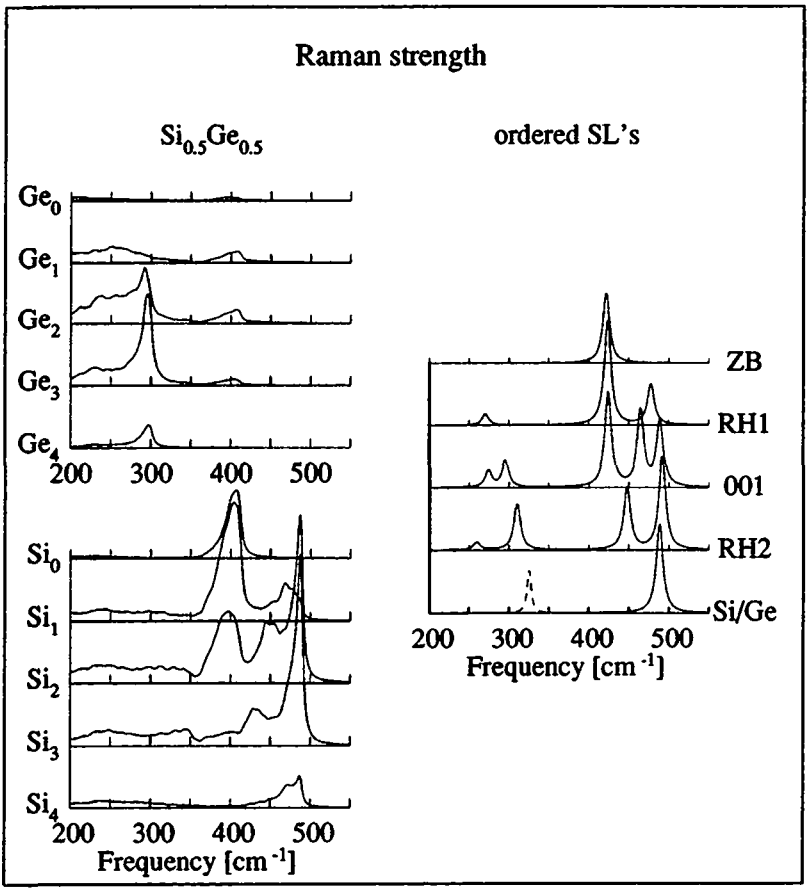

Figure 4.14: Partial Raman cross section of $Si_{\frac{1}{2}}Ge_{\frac{1}{2}}$ resolved according to the local environment, and spherical averaged Raman cross section of the corresponding ordered structures (see text).

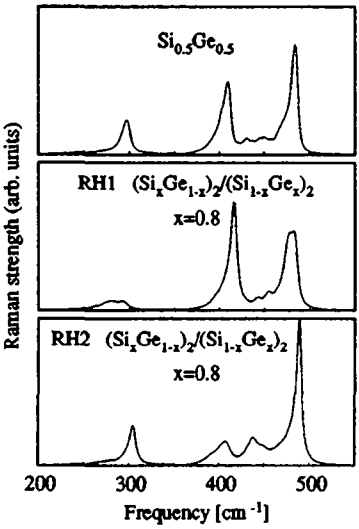

Figure 4.15: Raman spectra of $Si_{\frac{1}{2}}Ge_{\frac{1}{2}}$ with three different concentration profile: homogeneous alloy (upper panel), partially ordered RH1 alloy (middle panel) and partially ordered RH2 alloy (lower panel).

present analysis also shows that a same local environment can give rise to more than one weak peak, according to which bonds are active in the vibration. These features are potentially interesting for material characterization since from careful analysis of the relative intensities of the weak peaks some information can be gained on the dominant atomic coordination in the alloy or superstructure under study. Some similarity can also been found between the Ge_n partial Raman cross sections and the corresponding superlattice spectra in the frequency region around the *Ge-Ge* main peak. However, the situation is much less clear than for the Si_n weak peaks since in that region both kinds of atoms are vibrating as a consequence of the overlap of the *Ge* optical band with the *Si* acoustic one and so all feature are much broadened and less sensitive to the local coordination.

The possibility of extracting useful structural information from Raman spectroscopy in *SiGe* complex system is illustrated in Fig. 4.15 where the calculated Raman spectra for three sets of $Si_{\frac{1}{2}}Ge_{\frac{1}{2}}$ alloy configurations are shown. The top panel corresponds to configurations where the atoms are randomly distributed, the middle panel corresponds to configurations where atoms are still randomly distributed but with a concentration profile corresponding to a RH1 (111) superlattice with alternating Si_xGe_{1-x} layers of concentration $x = 0.2$ and $x = 0.8$. The lower panel is the same but for the RH2

(111) superlattice. As expected from comparison with Fig. 4.14, in the RH1 partially ordered structure an additional feature very close to the *Si-Si* main peak is formed and actually appears as a shoulder of it. Moreover, the intensity of the *Ge-Ge* main peak decreases and would eventually vanish in the completely ordered RH1 structure. In the RH2 partially ordered structure a very clear additional peak is present close to, but separate from, the *Si-Ge* main peak that is quite reduced and would disappear in the ordered compound.

Several authors have recognized the potential usefulness of the analysis of weak peaks in the Raman spectra of Si_xGe_{1-x} for material characterization, proposing, however, antithetic interpretations: signature of *long-range order* for some author,[81] they are, for others,[77,78] intrinsic properties of the *disordered* alloy that should not be present in the ordered case. From the previous analysis of their origin and the illustrative example of Fig. 4.15, it is clear that the correct interpretation is somewhat intermediate. *All* peaks in Si_xGe_{1-x}, main and secondary ones, are determined by the local atomic coordination and are present both in the random and in the partially ordered cases. Their intensity is determined by the relative abundance of the different atomic environments and can be used to detect deviation from the randomness in the sample. Other features, such as the peak positions and their sharpness, can be of valuable help to determine the strain condition of the sample or to detect the presence of long-range order. It is anyhow clear that to extract detailed information from Raman spectra an accurate dynamical model is necessary.

Chapter 5

Electronic structure

For their technological relevance, the electronic properties are by far the most important among the physical properties of semiconductor materials, and the interest on semiconductor alloys is primarily motivated by their potential usefulness in band-structure engineering. In this chapter the electronic structure of $Ga_{1-x}Al_xAs$ will be studied at the DFT level of approximation, describing—as usual in this work—the disordered alloy by random supercells. Correction beyond DFT will be added semi-empirically with the aim of clarifying the origin of the discrepancy between accurate quasi-particle (QP) calculations[82] and accepted experimental value of an indirect gap in $AlAs$.

5.1 GaAlAs

The electronic properties of $GaAs$, $AlAs$ and their alloys $Ga_{1-x}Al_xAs$ have been widely studied both theoretically and experimentally. Theoretically, *ab initio* determinations of single-particle energies, including self-energy corrections,[6,7] are only available for the pure compounds.[82] Alloy band structures have been mainly studied with empirical tight-binding models using CPA,[83] and recently the recursion method,[84,85] to cope with disorder. Being empirical, these approaches rely on experimental knowledge of the pure materials which is not always complete. An interesting step toward a first principles (DFT) description of alloy band structure is represented by the "Special Quasirandom Structures" (SQS) approach of Ref. 34 which, however, is presently limited to 50% alloys only. Due to the chemical similarity and the almost perfect lattice-matching of the pure compounds, disorder effects are commonly believed to be small in $Ga_{1-x}Al_xAs$ alloy and, even recently,[86,87] crude virtual-crystal DFT calculations have been performed in the alloy, which essentially interpolate linearly the pure-material band structures. Experimentally, the band structure of $GaAs$ is quite well known, while less information is available on $AlAs$. $GaAs$ is a direct ($\Gamma \rightarrow \Gamma$) gap semiconductor with higher conduction-band minima at L and X points in the BZ. In $AlAs$ the order of levels is reversed and the fundamental gap is indirect ($\Gamma \rightarrow$ X) with higher minima at L and Γ points. As a consequence of this different ordering, there is a crossover in the $Ga_{1-x}Al_xAs$ band structure from a direct to a indirect fundamental gap for an Al concentration $x \approx 0.4$. The direct gap is experimentally known[88,89] for the whole con-

centration range, whereas the indirect $\Gamma \rightarrow X$ transition has only been measured[88] where it is the fundamental one. The indirect $\Gamma \rightarrow L$ gap is never the fundamental one and it is only known[90] for *Al* concentration $x \lesssim 0.6$, where its composition dependence is remarkably linear. An experimental estimate of $\Gamma \rightarrow L$ gap in bulk *AlAs* is usually obtained by extrapolating the alloy results. This "experimental" value, however, strongly disagrees with the QP calculations of Ref. 82, where it is suggested that the extrapolation procedure could be inadequate, due to possible non-linear composition dependence of the gap in *AlAs*-rich alloys, but no explicit investigation on the origin of this non-linearity is made. In the following we will study from first principles the effects of chemical disorder on the band structure of $Ga_{1-x}Al_xAs$ and this will help reconciling previous experimental and theoretical findings.

Let us start our investigation with a study of the pure-material band structures as given by DFT calculations. The electron-ion interactions have been described by the norm-conserving non-relativistic pseudopotentials used in the previous chapters. A kinetic energy cutoff of 16 Ry and ten special points[15] for the BZ integration have been used and give single-particle energies converged within 0.01 eV. The calculations have been performed at the *theoretical* equilibrium lattice constant. Although this choice is the internally consistent one in first principles calculations,[91] a widespread attitude is—on the contrary—to calculate band structures of materials at their *experimental* lattice parameters. Besides being "empirical", this choice may lead to qualitatively incorrect results as, for instance, in the case of *Ge* which is incorrectly found[91,92] to have a vanishing direct-gap at Γ, while fully consistent DFT calculations[91] predict it to be an indirect-gap semiconductor, as the real material, with the correct conduction-band ordering. As a general trend, the calculation of band structures at theoretical equilibrium improves the agreement with experimental data, yet leaving a sizable error inherent to DFT.

In Fig. 5.1 we display the resulting band structures (solid lines) for *GaAs* and *AlAs*. The numerical values of the single-particle energies for selected high-symmetry states are reported in Table 5.1 ("DFT" rows), where, for comparison, the available experimental data and the results of QP calculations[82] are also given. All energies are referred to the valence-band maximum and spin-orbit effects are removed from experimental data. The characteristics and deficiencies of DFT band-structure calculations are manifest in this simple case. Valence-band energies calculated within DFT agree reasonably well (within 0.1–0.2 eV) with experimental data and QP calculations. As for the conduction bands, DFT reproduces correctly the order of levels but seriously underestimates their energies ($0.4 \div 0.7$ eV in *GaAs* and $0.7 \div 1.0$ eV in *AlAs* with respect to QP calculations). Quasi-particle energies agree generally well (within 0.1–0.2 eV) with experimental data with the only, already mentioned, exception of the L conduction-band minimum in *AlAs* which is placed by QP calculations ≈ 0.5 eV higher than the experimental value.

In order to study the electronic properties of disordered $Ga_{1-x}Al_xAs$ alloy in supercells containing several hundreds of atoms we simplify the DFT band-structure calculations as explained in Chapter 2. In the next section the approximations introduced are recalled and their validity in the present case is examined.

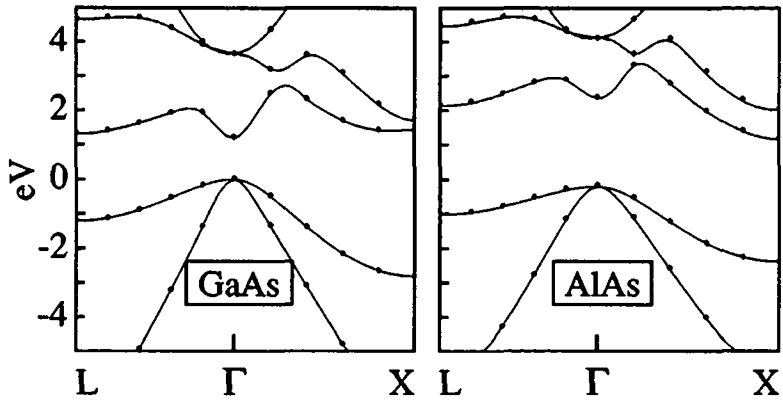

Figure 5.1: Band structures of *GaAs* and *AlAs* as obtained *i)* by DFT calculations (solid line), *ii)* with the linearized potential described in Section 5.1.1 (dashed line), and *iii)* with the linearized potential *and* a reduced basis-set of 8 virtual-crystal wavefunctions per k-point (dots).

GaAs	X_{3v}	X_{5v}	L_{1v}	L_{3v}	Γ_{1c}	X_{1c}	X_{3c}	L_{1c}
DFT	-6.83	-2.81	-6.72	-1.21	1.20	1.44	1.70	1.31
DFPT-8	-6.87	-2.84	-6.75	-1.23	1.20	1.43	1.71	1.31
QP[a]	—	-2.64	—	-1.11	1.58	2.19	2.41	1.93
Expt.[b]	-6.70	-2.80	-6.70	-1.30	1.62	2.10	2.50	1.93
AlAs	X_{3v}	X_{5v}	L_{1v}	L_{3v}	Γ_{1c}	X_{1c}	X_{3c}	L_{1c}
DFT	-5.48	-2.17	-5.64	-0.81	2.57	1.39	2.23	2.35
DFPT-8	-5.54	-2.23	-5.70	-0.84	2.55	1.37	2.23	2.33
QP[a]	—	-2.30	—	-0.89	3.35	2.18	—	3.12
Expt.[b]	—	-2.32	—	—	3.23	2.34	—	2.6

[a] Reference 82. [b] References 82 and 55.

Table 5.1: Single-particle energies (in eV) for selected high-symmetry states in *GaAs* and *AlAs* as obtained from complete DFT calculations and with the perturbative approach described in Section 5.1.1 (DFPT-8). Experimental data and quasi-particle results are also given for comparison. Spin-orbit effects are removed.

5.1.1 basic approximations and their validity

Any, simple or complex, *GaAlAs* system is defined by a set of Ising-like variables $\{\sigma_{\mathbf{R}}\}$, where $\sigma_{\mathbf{R}} = \pm 1$ if the cationic site at $\mathbf{R}$ is occupied by a *Ga* or an *Al* atom respectively. By considering the system as a slight perturbation with respect to the 50% virtual crystal, its KS effective potential can be written, exactly to linear order in the perturbation strength, as:

$$V_{eff}(\mathbf{r}) = V_{av,eff}(\mathbf{r}) + \sum_{\mathbf{R}} \sigma_{\mathbf{R}} \Delta V_{\sigma,eff}(\mathbf{r} - \mathbf{R}), \tag{5.1}$$

where $V_{av,eff}(\mathbf{r})$ is the virtual-crystal KS potential and $\Delta V_{\sigma,eff}(\mathbf{r})$ is the first order variation of the KS potential, induced by the transformation of the virtual atom at the origin into a real one, according to the value of σ.

The band structures of *GaAs* and *AlAs* as obtained with this linearized potential are drawn in Fig. 5.1 as dashed lines. These band structures are practically indistinguishable from those given by the complete DFT calculations discussed above (solid lines) showing that the linear approximation of Eq. 5.1 is an excellent one in *GaAlAs* systems.

In order to treat disorder, large supercells are needed and the corresponding eigenvalue problem has therefore to be further simplified. To this end the alloy wavefunctions, $\psi(\mathbf{r})$'s are expanded in terms of the virtual-crystal eigenfunctions, $\phi_{\mathbf{k},i}(\mathbf{r})$'s:

$$\psi(\mathbf{r}) = \sum_{i=1}^{N_b} \sum_{\mathbf{k}} c_i(\mathbf{k}) \phi_{\mathbf{k},i}(\mathbf{r}), \tag{5.2}$$

where the sum over $\mathbf{k}$ runs over the entire BZ and that over i includes only a limited number, N_b, of virtual-crystal bands.

In the case of $Ga_{1-x}Al_xAs$ considered here, owing to the similarity of the alloy and the virtual crystal, a basis-set including only a very small number of virtual-crystal eigenfunctions per atom is sufficient to give good results. This is demonstrated in the simple case of pure compounds in Fig. 5.1 where the band energies obtained with the linearized potential of Eq. 5.1 *and* a wavefunction expansion (Eq. 5.2) limited to 8 virtual-crystal bands are reported as dots. These energies are very close to the complete DFT results, slightly overestimating them as expected for an incomplete basis-set. The energies of several high-symmetry states, with respect to the valence-band top, are given in Table 5.1 ("DFPT-8" rows) and agree within 0.01–0.03 eV with DFT results for valence and conduction states close to the valence-band edge. The agreement is somewhat worse (0.03–0.06 eV) for deeper valence states, which are systematically found at a lower energy—with respect to valence-band top—than in the DFT calculations. This feature is a clear effect of basis-set incompleteness. Increasing by a factor 2–3 the number of virtual-crystal bands included in the expansion of Eq. 5.2, low-energy valence states, which are already converged for $N_b = 8$, remain practically unchanged, while near-edge valence and conduction bands are pushed down almost rigidly by interaction with higher states. The distance of the lower valence bands from valence-band top is thus reduced, while near-edge transitions are left almost unaltered.

$(GaAs)_1/(AlAs)_1$	$\overline{M}_v$	$\overline{R}_v$	$\overline{\Gamma}_{4c}$	$\overline{\Gamma}_{1c}$	$\overline{\Gamma}_{1c}$	$\overline{M}_{5c}$	$\overline{M}_{1c}$	$\overline{M}_{2c}$	$\overline{R}_{1c}$	$\overline{R}_{4c}$
DFT	-2.41	-0.98	1.49	1.56	2.30	1.41	1.52	2.40	1.41	2.28
DFPT-8	-2.46	-1.01	1.48	1.55	2.30	1.40	1.52	2.40	1.39	2.26
$(GaAs)_2/(AlAs)_2$	$\overline{M}_v$	$\overline{X}_v$	$\overline{\Gamma}_{1c}$	$\overline{\Gamma}_{1c}$	$\overline{\Gamma}_{4c}$	$\overline{M}_{2c}$	$\overline{M}_{1c}$	$\overline{M}_{5c}$	$\overline{X}_{1c}$	$\overline{X}_{4c}$
DFT	-2.49	-1.00	1.37	1.75	1.91	1.35	1.39	1.93	1.77	1.80
DFPT-8	-2.54	-1.02	1.37	1.72	1.93	1.34	1.39	1.93	1.75	1.77

Table 5.2: Single-particle energies (in eV) for selected high-symmetry states two short-period (001) superlattices as obtained from complete DFT calculations and from the present perturbative approach (DFPT-8).

As a further test of the accuracy of our approximations, the band structures of a few ordered *GaAlAs* structures have been examined. In Table 5.2 the results for two short-period (001) SL's, as obtained within DFT and by the present method (with $N_b = 8$), are reported, and confirm the reliability of the perturbative calculations. Also in this case, the agreement for lower valence states improves by improving basis-set completeness while near-edge transitions remain unchanged. A few other ordered structures have been considered obtaining similar results.

Electronic properties of short-period SL's are interesting on their own and have been extensively studied in the last years.[93–95] Short-period SL states can be classified[95] as "repelling", "segregating" or "averaging" according to which of the following cases applies. *i)* Two SL states are said to be "repelling" if, having *different* symmetry in the virtual crystal, they acquire the same symmetry in the SL and therefore repel each other. An example of this behaviour are the two $\overline{\Gamma}_{1c}$ states in the 1+1 SL (we denote by a bar SL states and keep ordinary symbols for the original zincblende ones) that come from Γ_{1c} and X_{3c} states of the virtual crystal. SL potential split the two levels pushing the lowest one, which has $\approx 50\%$ Γ-character *below* the average value of the Γ_{1c} states in the pure materials. This state gives rise to an optical transition, observed[94] in the SL 0.1÷0.15 eV below the alloy optical gap.[88,89] The $\overline{\Gamma}_{4c}$ SL state, coming from virtual-crystal X_{1c} one, is also repelled by one of the valence-band Γ_{15v} states, but only weakly and acquires only a small Γ-character ($\lesssim 5\%$). The corresponding transition is therefore only "pseudo"-direct. *ii)* Some SL states would belong to the *same* symmetry in the virtual crystal but have different symmetry in the SL. They are called[95] "segregating" when the SL symmetry-restriction localizes them in different portions of the system. An example of this behaviour is given by the $\overline{R}_{1c}$ and $\overline{R}_{4c}$ states in the 1+1 SL, which

come from the L_{1c} virtual-crystal states and are localized by symmetry on the *GaAs* and *AlAs* layers, respectively. As a consequence their energy is very close to L_{1c} energy in the corresponding pure materials. *iii)* In the absence of symmetry-induced repulsion or segregation SL states are delocalized over the entire SL and experience therefore an "average" crystal potential and their energy stays close to the virtual-crystal one. This is the case, for instance, for $\overline{M}_{5c}$ states in 1+1 and 2+2 SL's that originate from X_{1c} and X_{3c} virtual-crystal states respectively. We stress again that all these different situations are well reproduced by the smallest, $N_b = 8$, basis-set considered here.

5.1.2 alloy band structure

We pass now to illustrate our results for homogeneous $Ga_{1-x}Al_xAs$ alloys. The disordered alloys have been simulated by simple-cubic supercells containing 512 atoms (256 cations) randomly distributed, according to the concentration considered. The $N_b = 8$ basis-set have been used in the wavefunction expansion and the resulting alloy hamiltonian matrices were small enough to be diagonalized with standard techniques. For each concentration the results were averaged over five random configurations.

In order to discuss the alloy band structure, let us define the momentum-projected densities of states:

$$n(\mathbf{k},\epsilon) = \sum_\nu \delta(\epsilon - \epsilon_\nu)\langle\psi_\nu|\hat{P}_\mathbf{k}|\psi_\nu\rangle = \sum_\nu \delta(\epsilon - \epsilon_\nu)\sum_i^{N_b} |\langle\psi_\nu|\phi_{\mathbf{k},i}\rangle|^2 \qquad (5.3)$$

where $\hat{P}_\mathbf{k}$ projects over states with crystal momentum $\mathbf{k}$, and the sums run over all alloy states, ψ_ν's, and all basis-functions of that crystal momentum, $\phi_{\mathbf{k},i}$'s, respectively. In actual calculations the δ function appearing in Eq. 5.3 is substituted by a gaussian of standard deviation $\sigma = 0.02$ eV.

Electronic disorder is usually believed to be weak in *GaAlAs* systems and one expects the band picture—strictly valid only in the pure compounds—to be still approximately so in the alloy as well. This is actually the case and in Fig 5.2 we show the band structure of $Ga_{\frac{1}{2}}Al_{\frac{1}{2}}As$ as obtained from the peak positions in the alloy k-projected DOS (also reported in Fig 5.2). Peaks are quite sharp in the valence-band region, whereas they are broader for conduction bands, yet remaining well defined. In the present DFT calculations $Ga_{\frac{1}{2}}Al_{\frac{1}{2}}As$ is found to be a indirect gap ($\Gamma \rightarrow X$) semiconductor with close higher transitions at L and Γ points, a feature in agreement with experimental data.[89-90]

The composition dependence of the projected DOS for high-symmetry points is analyzed in Fig. 5.3 for energies around the fundamental gap. The composition average of the valence-band tops of the pure materials has been taken as reference energy in all cases. The maximum of the valence band is found to be at Γ point for all compositions and its dependence on *Al* concentration is remarkably linear, thus the virtual crystal approximation works well in this case. This is not unexpected since these states are mostly *As* p-like and are little affected by alloying the cationic sublattice. No contribution to the non-linear variation (bowing) of the gap energies with composition comes from valence-band states.

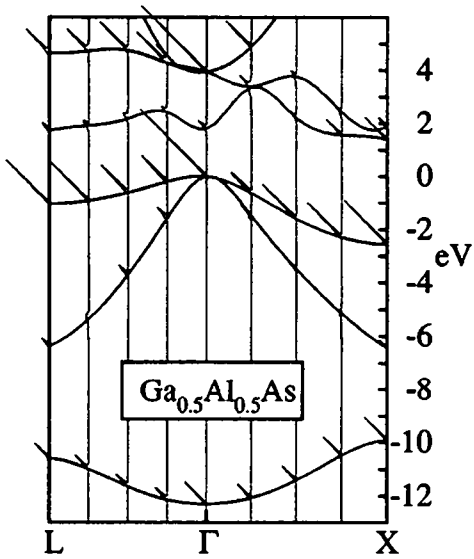

Figure 5.2: Band structure along Λ and Δ symmetry directions for $Ga_{\frac{1}{2}}Al_{\frac{1}{2}}As$, as obtained by supercell calculations. Momentum-projected DOS are also shown.

Conduction states, on the contrary, have large components on cationic sites and their energy levels display deviations from linearity. Virtual crystal results, shown in Fig. 5.3 as dashed lines, give only a poor approximation in this case. Bowing is weak for X_{1c} state, whereas it is substantial for Γ_{1c}, X_{3c} and L_{1c} ones. Peaks are well defined at low excitation energy—in particular the conduction-band absolute minimum in the alloy is always quite sharp—but they are broader and less well defined for higher excitation energy states, as a consequence of the increased number of close-in-energy states to which they can be scattered by the random alloy potential. The composition dependence of the average peak energies, as obtained by our supercell calculations, is reported in Fig. 5.3 as solid lines and the results for the different energy gaps are collected in the left panel of Fig. 5.4.

In Fig. 5.4, we can see that the correct order of level-crossings (L-X, Γ-X and then Γ-L) is reproduced by our calculations, but the corresponding crossover concentrations are poorly estimated. Moreover, little, if any, improvement is found with respect to simple virtual crystal approximation (see Table 5.3). However, DFT gaps cannot be directly compared with experiments and one has to correct for the intrinsic DFT error before making the comparison. The simplest way, adopted here, to correct for this error is to assume that QP and disorder effects act separately on the reference virtual-crystal band structure. Moreover, QP corrections for the virtual crystal can be taken to be the linear interpolation of the empirical corrections to be added to DFT pure-

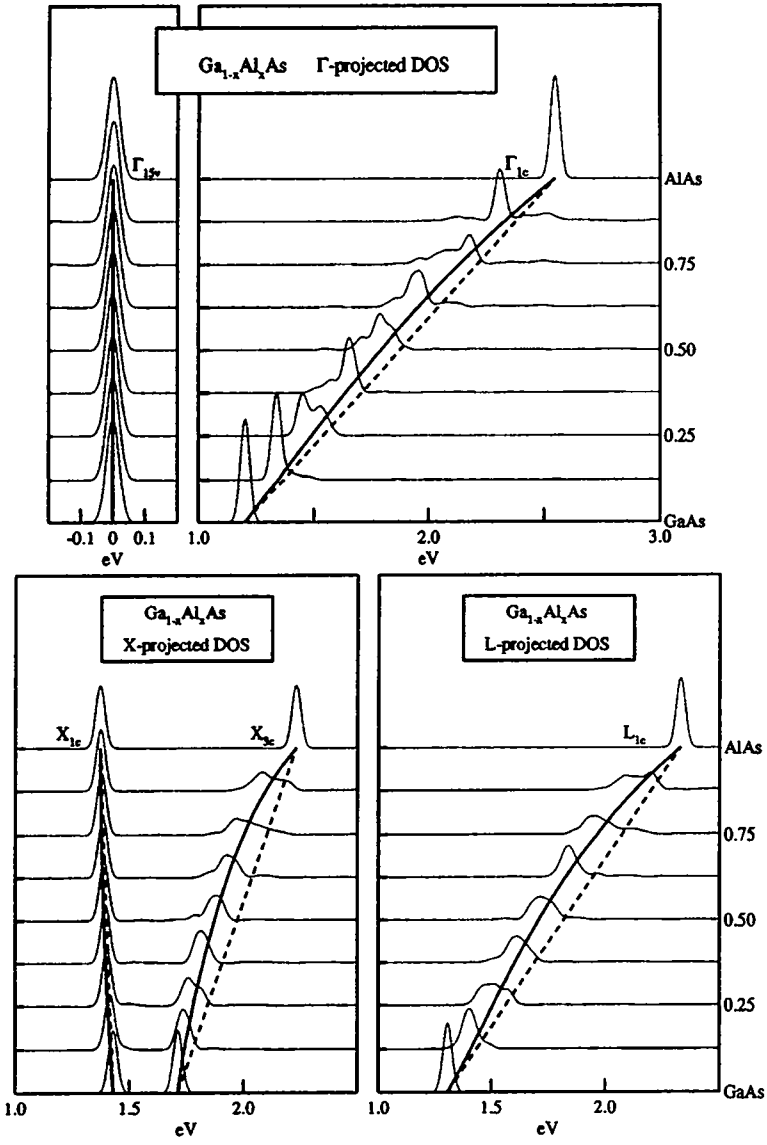

Figure 5.3: Projected density of states for Γ, X and L points displayed as a function of $Ga_{1-x}Al_xAs$ composition, x. The composition dependence of the peak positions is drawn as solid lines. Dashed lines show the virtual-crystal results.

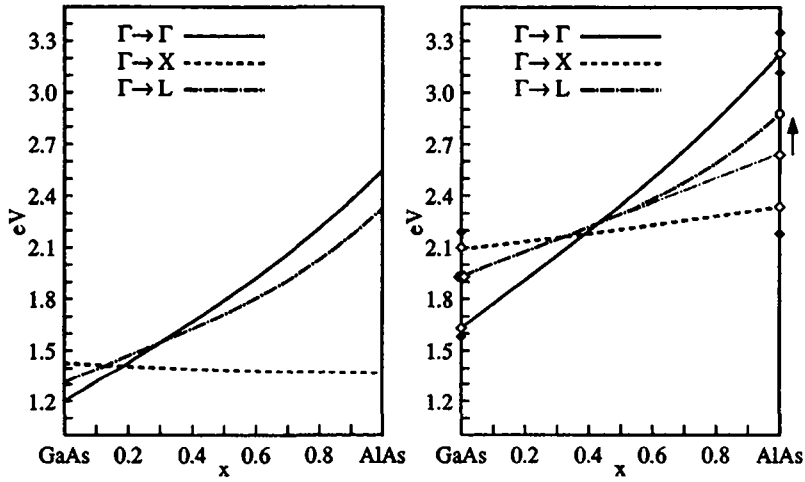

Figure 5.4: Band gaps of $Ga_{1-x}Al_xAs$ as obtained from the present DFT calculations (left) and after empirical correction to agree with the end-points experimental data as explained in the text (right). Solid diamonds are the quasi-particle results of Ref. 82, empty diamonds are the usually accepted experimental values. The empty dot marks the revised value of the indirect L gap of $AlAs$ suggested by the present calculations.

material gaps in order to reproduce the experimental results of Table 5.1. Adopting this correction, however, even worse results are obtained, and even the order of the level-crossings is wrong, predicting a large range of compositions ($0.3 \lesssim x \lesssim 0.6$) where the fundamental gap would be the indirect $\Gamma \rightarrow$ L one. This situation, although predicted (and judged satisfactory) in some recent theoretical work,[96] is in sharp contradiction with experimental data, showing that our correction is somewhat oversimplified. The root of the problem (and of its solution) can be found in the marked non-linearity, in the composition dependence, of the $\Gamma \rightarrow$ L energy gap which is apparently in disagreement with the linear dependence reported experimentally.[90] As a matter of fact, $\Gamma \rightarrow$ L transition is experimentally known only for $GaAs$-rich alloys ($x \lesssim 0.6$), where also our calculated gap is remarkably linear, and the "experimental" value of the gap in $AlAs$ is obtaine by linear extrapolation of the alloy data. A better way to use experimental information to correct the calculated $\Gamma \rightarrow$ L gap is, therefore, to require agreement with the experimental results for the value linearly extrapolated from $GaAs$-rich alloys. The situation is illustrated in the right panel of Fig. 5.4, where the experimental values and the QP results[82] of Table 5.1 are also reported for comparison as empty and solid diamonds, respectively. From this figure it can be seen that good agreement with a linear behaviour is found for all concentrations in the experimentally accessible range thus confirming the soundness of our semi-empirical correction. Substantial agreement with experimental results is also obtained for the crossover concentrations and the

crossover	VCA	DFT	corrected DFT	Experiment
L-X	0.11	0.13	0.33 (2.16)	0.35 (2.15)
Γ-X	0.16	0.19	0.39 (2.18)	0.40 (2.16)
Γ-L	0.33	0.30	0.43 (2.24)	0.43 (2.20)

Table 5.3: Crossover concentrations of the different gaps in $Ga_{1-x}Al_xAs$ alloys as obtained by the virtual crystal approximation, our DFT supercell calculations and after their empirical correction described in the text. Experimental value are also shown for comparison. In the last two cases the energy of gaps at the crossover composition is also given (in parenthesis).

corresponding gap energies (see Table 5.3).

The most important finding in our calculations is however the appearance of strong non-linearity of the composition dependence of the $\Gamma \rightarrow$ L transition in *AlAs*-rich $Ga_{1-x}Al_xAs$ alloys. This behaviour, proposed in Ref. 82 to explain the disagreement with experimental results of their QP calculations, is demonstrated here from first principles. From our calculations the $\Gamma \rightarrow$ L gap in *AlAs* is placed ≈ 0.25 eV higher in energy than its extrapolated value from low-concentration alloys and thus within ≈ 0.25 eV the QP results of Ref. 82. In view of the 0.2 eV error-bar quoted for the QP calculations, this agreement can be considered as satisfactory.

Let us finally discuss the importance of self-energy contributions to the bowing of energy gaps, that have been neglected here. It is not easy to give a realistic value of these contributions without a full calculation, but an order-of-magnitude estimate can be obtained by simple considerations. Self-energy corrections in semiconductors can roughly be represented by a *scissors operator*[97] that rigidly shifts upward conduction bands and whose value is $\approx 9/\epsilon_\infty$ eV, where ϵ_∞ is the high-frequency static dielectric constant of the system considered.[87,98] Together with the linear composition dependence of the dielectric constant in $Ga_{1-x}Al_xAs$ alloys, this very crude model gives a self-energy correction to the energy bowing one order of magnitude smaller than our DFT results. Virtual-crystal calculations with a more refined semi-empirical correction give an even smaller effect. Although it is clear that a final answer to this question can only come from a complete self-energy calculation in a realistic realization of the alloy, it seems evident that a proper description of disorder at the DFT level of approximation already captures the essential features of the system and can be very useful in the study of complex situations.

Chapter 6

Conclusions

In this thesis the structure, the thermodynamics, the lattice dynamics and the electronic structure of semiconductor alloys have been studied from first principles. These properties have been studied by a perturbative approach where, relying on the chemical similarity of semiconductor compounds, one describes the alloy as a slight perturbation with respect to the corresponding 50% virtual crystal. The quantities relevant to describe the physical property under investigation are therefore expanded around the reference system. Different physical properties are described by different models, all having in common their first principles perturbative origin and their simplicity. Although approximated, this approach has shown to be quite accurate in all the situations considered in this work, and has allowed to study the different physical properties employing a realistic description of the disorder in the alloy.

Among semiconductor alloys, the $Ga_xAl_{1-x}As$ and the Si_xGe_{1-x} alloys, which are the most interesting for their possible technological applications, have been studied in details. Our investigation has allowed, in many cases, to clarify, or to understand better, some experimentally observed features of these systems.

Studying the bulk thermodynamics of $Ga_xAl_{1-x}As$ and Si_xGe_{1-x} we have found that in both case the segregated compounds are the equilibrium states of the alloy at low temperature, while, already at room temperature, the two systems are miscible in the whole composition range and the random alloy is the stable state. No thermodynamic tendency to order is found in our calculations, showing that the ordered structures observed[39,40] in epitaxially grown samples are not the thermodynamical equilibrium state, but are probably induced by the growth process. Other semiconductor systems have to be studied, before the generality of this finding can be assessed. The study of thermodynamics of $Ga_xIn_{1-x}P$ alloy is currently under way.[99]

As for their vibrational properties, $Ga_xAl_{1-x}As$ and Si_xGe_{1-x} alloys are, instead, quite different. In $Ga_xAl_{1-x}As$ well defined dispersion relations survive in the disordered alloy. In Si_xGe_{1-x} the phonon dispersions are much less well defined and additional weak features, in the density of states and Raman spectra, are found, which originate from the different local environments present in the alloy. Using the same techniques employed in this work for the homogeneous alloy, interface-disordered $GaAs/AlAs$ superlattices have been studied.[66] This study has allowed to clarify some

controversial aspects of the vibrational properties of these systems and to give valuable information for their structural characterization. A similar study in the case of *SiGe* systems will be undertaken in the future.

As for the electronic structure calculations, only $Ga_xAl_{1-x}As$ alloy has been studied. The predictive power of our first principles calculations is in this case necessarily somewhat spoiled by the neglect of quasiparticle corrections. Nevertheless, the proper description of the effects of disorder at the DFT level already gives the essential features of the system and allows to reconcile previous experimental[90] and theoretical[82] results for *AlAs*. With the present method, the effects of interface disorder on the electronic properties of short-period superlattices could be studied, which is of interest both from the fundamental point of view and for material characterization. However, a method, approximate but reliable, to incorporate in the band structure calculation of the alloy the quasiparticle effects is highly desirable.

In conclusion, this thesis has demonstrated that accurate numerical calculations can, nowadays, be performed in semiconductor alloys and that these investigations can be of valuable help in the interpretations of the experimental results and in the understanding of the physical properties of these technologically important materials.

Appendix A

Technical aspects in DFPT pseudopotential calculations

A.1 non-local norm-conserving pseudopotentials

In modern pseudopotential calculations the electron-ion interaction is described by *ab initio* norm-conserving pseudopotentials,[18] constructed from first principles in such a way to reproduce the *all-electrons* results with minimum error. They contain a local term and an angular-momentum-dependent non-local one that describes the orthogonality of valence electrons to the different core states:

$$V_{ps} = V^{loc}(\mathbf{r}) + \sum_l V_l^{NL}(\mathbf{r})\hat{P}_l, \tag{A.1}$$

where $\hat{P}_l$ is the projector over the subspace of angular momentum l.

Only a few modifications are necessary in the formalism outlined in Section 2.1 to use non-local potentials. Kohn-Sham equations, Eqs. 2.2, are solved iteratively as usual with the only modification that the external potential, and hence the effective one, is non-local. Pseudopotentials are usually expressed in terms of analytic functions[100] and their matrix elements between plane waves are easily evaluated. In the expression for the electronic energy, Eq. 2.1, the term involving the external potential is modified:

$$\int V(\mathbf{r})n(\mathbf{r})d\mathbf{r} \longrightarrow \sum_i \langle\phi_i|V|\phi_i\rangle, \tag{A.2}$$

where the sum runs over the occupied states, ϕ_i's, and $n(\mathbf{r}) = \sum_i |\phi_i(\mathbf{r})|^2$ is the ground state electron density of the system. Note that the new expression is more general and reduces to the previous one when the external potential is local. The expression for the first-order energy derivative, Eq. 2.5, is modified accordingly:

$$\frac{d\mathcal{E}_{el}}{d\lambda} = \sum_i \langle\phi_i|\Delta V|\phi_i\rangle, \tag{A.3}$$

and that for the second-order one, Eq. 2.7, becomes

$$\frac{d^2\mathcal{E}_{el}}{d\lambda^2} = 2\sum_i \langle\phi_i|\Delta V|\Delta\phi_i\rangle, \tag{A.4}$$

where the $\Delta\phi_i$'s are the first order variations of the ϕ_i's induced by the perturbation ΔV, and can be obtained as usual from Eqs. 2.8, with the only modification that the perturbing potential, and hence ΔV_{eff}, is now a non-local operator.

A.2 macroscopic electric field

The high-frequency static dielectric tensor relates the screened electric field (with clamped ions) $\mathbf{E}$ to the bare electric field $\mathbf{E}_0$: $\mathbf{E}_0 = \epsilon_\infty \cdot \mathbf{E}$. The Born effective charges are defined as the force acting on ions due to the presence of an electric field or, equivalently, the macroscopic polarization induced by atomic displacements. The key quantity in their evaluation is the response of the crystal to an applied electric field.

The calculation of the ground state of a crystal, with the standard Born-von Kármán boundary conditions, in the presence of a nonvanishing electric field is not possible, since the diagonal matrix elements of the bare electrostatic potential, $\Delta V(\mathbf{r}) = e\mathbf{E}_0 \cdot \mathbf{r}$, are ill-defined in an infinite solid with periodic boundary conditions. No particular problem arises, instead, in a perturbative calculation of the *variation* of the energy induced by applying an electric field, since only off-diagonal matrix elements are then needed and these are well defined quantities. A compact way to express this fact is through the following linear system

$$\left[-\frac{\hbar^2}{2m}\nabla^2 + V_{eff}(\mathbf{r}) - \varepsilon_i\right] \hat{Q}_i \mathbf{r} \phi_i(\mathbf{r}) = \hat{Q}_i \left[h_{eff}, \mathbf{r}\right] \phi_i(\mathbf{r}), \tag{A.5}$$

where $\hat{Q}_i = 1 - \hat{P}_i = 1 - |\phi_i\rangle\langle\phi_i|$ is the projector on the Hilbert subspace orthogonal to the state under consideration and the commutator is a well-behaved periodic operator given by

$$\left[h_{eff}, \mathbf{r}\right] = \frac{-i\hbar\mathbf{p}}{m} + \left[V, \mathbf{r}\right], \tag{A.6}$$

where the first term comes from the kinetic energy and the second one, coming from the external potential, would vanish for local pseudopotentials. The Hartree and the exchange-correletion potentials, being local, give no contrinution to the commutator.

When the perturbing potental is a macroscopic electric field, Eqs. 2.8 are slightly modified to take into account the fact that the density response, and therefore the effective perturbing potential, has a macroscopic part as well as the usual microscopic one. Let us introduce the auxiliary functions $\mathbf{Q}_i(\mathbf{r}) = \hat{Q}_i \mathbf{r} \phi_i(\mathbf{r})$, that can be evaluated from Eqs. A.5-6 and stored once and for all at the beginning of the linear-response calculation. Eqs. 2.8 become:

$$\left[-\frac{\hbar^2}{2m}\nabla^2 + V_{eff}(\mathbf{r}) - \varepsilon_i\right] \Delta\phi_i(\mathbf{r}) = \hat{Q}_i \Delta V^{mic}_{eff}(\mathbf{r}) \phi_i(\mathbf{r}) + e\mathbf{E} \cdot \mathbf{Q}_i(\mathbf{r}), \tag{A.7a}$$

$$\Delta V^{mic}_{eff}(\mathbf{r}) = e^2 \int \frac{\Delta n^{mic}(\mathbf{r}')}{|\mathbf{r} - \mathbf{r}'|} d\mathbf{r}' + \frac{d\mu^{hom}_{xc}}{dn}(n_0(\mathbf{r}))\, \Delta n^{mic}(\mathbf{r}), \tag{A.7b}$$

$$\Delta n^{mic}(\mathbf{r}) = 2 \sum_i \phi^*_i(\mathbf{r}) \Delta\phi_i(\mathbf{r}), \tag{A.7c}$$

$$\mathbf{E} = \mathbf{E}_0 - 4\pi\mathbf{P}, \quad \mathbf{P} = \frac{e}{N\Omega} 2 \sum_i \langle Q_i | \Delta\phi_i(\mathbf{r}) \rangle, \tag{A.7d}$$

where $N\Omega$ is the total volume of the sample.

These equations can be solved iteratively, as usual, starting from a given bare electric field, $\mathbf{E}_0$, and screening it with the microscopic (Eq. A.7b) as well as with the macroscopic (Eq. A.7d) term. However, for the sake of computational stability and simplicity, it is more convenient to keep the value of the screened macroscopic field, $\mathbf{E}$, fixed during the calculation, iterating only Eqs. A.7a-c. Once self-consistency is achieved, Eq. A.7d gives directly the dielectric constant tensor:

$$\epsilon_{\infty,\alpha\beta} = \delta_{\alpha\beta} + \frac{8\pi e^2}{N\Omega} \sum_i \langle Q_i^\alpha | \Delta_{\mathbf{E}^\beta} \phi_i \rangle \tag{A.8}$$

where $\Delta_{\mathbf{E}}\phi_i(\mathbf{r})$ is the linear response of the wavefunction $\phi_i(\mathbf{r})$ when a unitary electric field, $e\mathbf{E}$, is applied. The Born effective charges are, instead, given by:

$$Z^*_{s,\alpha\beta} = Z_s \delta_{\alpha\beta} + \frac{2}{N} \sum_i \langle \phi_i | \Delta V^s_{\mathbf{u}^\beta} | \Delta_{\mathbf{E}^\alpha} \phi_i \rangle, \tag{A.9a}$$

$$Z^*_{s,\alpha\beta} = Z_s \delta_{\alpha\beta} + \frac{2}{N} \sum_i \langle Q_i^\alpha | \Delta_{\mathbf{u}_s^\beta} \phi_i \rangle, \tag{A.9b}$$

according to the two, equivalent, definitions. The first expression—where $\Delta V^s_{\mathbf{u}^\alpha}$ is the bare perturbing potential corresponding to the displacement of the atom s and Z_s its bare ionic (pseudo)charge—gives the force acting on the atom s due to the presence of the electric field and the second one—where $\Delta_{\mathbf{u}_s^\beta}\phi_i(\mathbf{r})$ is the linear response of the wavefunction $\phi_i(\mathbf{r})$ to the displacement of the atom s—gives the macroscopic polarization induced by the displacement of that atom. From the computational point of view the two expressions are of comparable complexity and either of them can be used to evaluate the effective charges, in practice.

References

[1] To have just a glance of the recent activity in the field, see for instance the *Proc. of the 20th International Conference on the Physics of Semiconductors*, E.M. Anastassakis and J.D. Joannopoulos Eds., World Scientific, Singapore (1991).

[2] P. Hohenberg and W. Kohn, Phys. Rev. **136**, B864 (1964).

[3] W. Kohn and L.J. Sham, Phys. Rev. **140**, A1133 (1965).

[4] J.P. Perdew and M. Levy, Phys. Rev. Lett. **51**, 1884 (1983); L.J. Sham and M. Schlüter, Phys. Rev. Lett. **51**, 1888 (1983); L.J. Sham and M. Schlüter, Phys. Rev. B **32**, 3883 (1985).

[5] W.H. Butler and W. Kohn, J. of Res. of the Nat. Bureau of Standards, A. *Physics and Chemistry*, **74A**, 443 (1970); W. Kohn and J. Olson, Journal de Physique, Colloque C3, **33**, 135 (1972).

[6] L. Hedin, Phys. Rev. **139**, A796 (1965).

[7] M.S. Hybertsen and S.G. Louie, Phys. Rev. Lett. **55**, 1418 (1985); M.S. Hybertsen and S.G. Louie, Phys. Rev. B **34**, 5390 (1986); R.W. Godby, M. Schlüter, and L.J. Sham, Phys. Rev. Lett. **56**, 2415 (1986); R.W. Godby, M. Schlüter, and L.J. Sham, Phys. Rev. B **35**, 4170 (1987); R.W. Godby, M. Schlüter, and L.J. Sham, Phys. Rev. B **36**, 6497 (1987); R.W. Godby, M. Schlüter, and L.J. Sham, Phys. Rev. B **37**, 10159 (1988); F. Gygi and A. Baldereschi, Phys. Rev. Lett. **62**, 2160 (1989).

[8] D.M. Ceperley and B.J. Alder, Phys. Rev. Lett. **45**, 566 (1980); J. Perdew and A. Zunger, Phys. Rev. B **23**, 5048 (1981).

[9] H. Hellmann, *Einführung in die Quantenchemie* (Deuticke, Leipzig, 1937); R.P. Feynman, Phys. Rev. **56**, 340 (1939).

[10] X. Gonze and J.P. Vigneron, Phys. Rev. B **39**, 13120 (1989).

[11] S. Baroni, P. Giannozzi, and A. Testa, Phys. Rev. Lett. **58**, 1861 (1987).

[12] S. de Gironcoli, S. Baroni, and R. Resta, Phys. Rev. Lett. **62**, 2853 (1989); S. de Gironcoli, S. Baroni, and R. Resta, Ferroelectrics **111**, 19 (1990).

[13] P. Giannozzi, S. de Gironcoli, R. Resta, in *Proc. Phonons 89*, edited by S. Hunklinger, W. Ludwig, and G. weiss (World Scientific, Singapore, 1989), p. 205.

[14] R.M. Martin and K. Kunc, Phys. Rev. B **24**, 2081 (1981); K. Kunc and R. Resta, Phys. Rev. Lett. **51**, 686 (1983); J.B. McKitterick, Phys. Rev. B **28**, 7384 (1983).

[15] A. Baldereschi, Phys. Rev. B **7**, 5212 (1973); D.J. Chadi and M.L. Cohen, Phys. Rev. B **8**, 5747 (1973); H.J. Monkhorst and J.D. Pack, Phys. Rev. B **13**, 5188 (1976).

[16] F. Bassani and G. Pastori Parravicini, *Electronic States and Optical Transitions in Solids* (Pergamon, Oxford, 1975).

[17] P. Giannozzi, G. Grosso and G. Pastori Parravicini, La Rivista del Nuovo Cimento **13**, n° 3.

[18] D.R. Hamann, M. Schlüter and C. Chiang, Phys. Rev. Lett. **43**, 1494 (1979).

[19] V. Heine and D. Weaire, *Solid State Physics*, edited by H. Ehrenreich, F. Seitz, and D. Turnbull (Academic, New York, 1970), Vol. 24, p. 250; J. Hafner, *From Hamiltonians to Phase Diagrams*, Springer Series in Solid State Science, Vol. 70 (Springer, Berlin, 1987).

[20] The fact that to second order in the perturbation the lattice interactions are only two-body interactions is closely related to a well known similar property obtained for continuous interactions in pseudopotential perturbation theory. See for instance: M.H. Cohen, J. Phys. Radium **23**, 643 (1962).

[21] H. Kanzaki, J. Phys. Chem. Solids **2**, 24 (1952); H. Kanzaki, J. Phys. Chem. Solids **2**, 107 (1952).

[22] S. Froyen and C. Herring, J. Appl. Phys. **52**, 7165 (1981).

[23] R. Kikuchi, Phys. Rev. **81**, 988 (1951).

[24] D. de Fontaine, in *Solid State Physics*, edited by H. Ehrenreich, F. Seitz, and D. Turnbull (Academic, New York, 1970), Vol. 34, p. 73.

[25] L.G. Ferreira, S-H. Wei, and A. Zunger, Phys. Rev. B **40**, 3197 (1989); S-H. Wei, L.G. Ferreira, and A. Zunger, Phys. Rev. B **41**, 8240 (1990).

[26] D.B. Laks, L.G. Ferreira, S. Froyen, and A. Zunger, unpublished; A. Zunger private communication.

[27] M. Born and K. Huang, *Dynamical Theory of Crystal Lattices* (Oxford University Press, Oxford, 1954).

[28] W. Cochran and R.A. Cowley, J. Chem. Phys. Solids **23**, 447 (1962).

[29] S. Baroni, P. Giannozzi, and E. Molinari, Phys. Rev. B **41**, 3870 (1990).

[30] A.S. Barker Jr., J.L. Merz, and A.C. Gossard, Phys. Rev. B **17**, 3181 (1978).

[31] P. Giannozzi, S. de Gironcoli, P. Pavone, and S. Baroni, Phys. Rev. B **43**, 7231 (1991)

[32] R. Pick, M.H. Cohen, and R.M. Martin, Phys. Rev. B **1**, 910 (1970).

[33] A. Fleszar and R. Resta, Phys. Rev. B **34**, 7140 (1986).

[34] A. Zunger, S.-H. Wei, L.G. Ferreira, and J.E. Bernard, Phys. Rev. Lett. **65**, 353 (1990); K.C. Hass, L.C. Davis, and A. Zunger, Phys. Rev. B **42**, 3757 (1990); S.-H. Wei, L.G. Ferreira, J.E. Bernard, and A. Zunger, Phys. Rev. B **42**, 9622 (1990).

[35] S. Baroni, R. Resta, A. Baldereschi, and M. Peressi, in *Spectroscopy of semiconductor Microstructures*, edited by G. Fasol, A. Fasolino, and P. Lugli, NATO Advanced Study Institute Ser. B, Vol. 106 (Plenum, New York, 1989), p. 251; M. Peressi, S. Baroni, A. Baldereschi, and R. Resta, Phys. Rev. B **41**, 12106 (1990).

[36] M.B. Panish and M. Ilegems, in *Progress in solid State Chemistry*, edited by H. Reiss and J.O. Mc Caldin, Vol. 7, Pergamon Press, New York (1972); G.B. Stringfellow, J. Phys. Chem. Solids **33**, 665 (1972); G.B. Stringfellow, J. Phys. Chem. Solids **34**, 1749 (1973).

[37] L.M. Foster, J.E. Scardefield, and J.F. Woods, J. Electrochem. Soc. **119**, 765 (1972); V.T. Bublik and V.N. Leikin, Phys. Status Solidi A **46**, 365 (1978).

[38] C.D. Thourmound, J. Phys. Chem. **57**, 827 (1953); M. Hansen, *Constitution of Binary Alloys* (McGraw-Hill, New York, 1858), 2nd ed., p. 774.

[39] T.S. Kuan, T.F. Kuech, W.I. Wang, and E.L. Wilkie, Phys. Rev. Lett. **54**, 201 (1985); C. Bocchi, P. Franzosi, and C. Ghezzi, J. Appl. Phys. **57**, 4533 (1985).

[40] A. Ourmazd and J.C. Bean, Phys. Rev. Lett. **55**, 765 (191985).

[41] H.R. Jen, M.J. Cherng, and G.B. Stringfellow, Appl. Phys. Lett. **48**, 1603 (1986); A. Gomyo, T. Suzuki, K. Kobayashi, I. Hino, and T. Yuasa, Appl. Phys. Lett. **50**, 673 (1987); M.A. Shahid, S. Mahajan, D.E. Laughlin, and H.M. Cox, Phys. Rev. Lett. **58**, 2567 (1987); T.S. Kuan, W.I. Wang, and E.L. Wilkie, Appl. Phys. Lett. **51**, 51 (1987); A. Gomyo, T. Suzuki, and S. Iijima, Phys. Rev. Lett. **60**, 2645 (1988).

[42] U. von Barth and R. Car, unpublished. This scheme consists essentially in a fitting minimization of the squared differences between the atomic all-electron and pseudo eigenvalues and eigenfunctions (beyond a given core radius r_c), as functions of a few parameters upon which the pseudopotential depends.

[43] S. Lee, D.M. Bylander, and L. Kleinman, Phys. Rev. B **40**, 8399 (1989).

[44] P.B. Littlewood, Phys. Rev. B **34**, 1363 (1986); J.L. Martins and A. Zunger, Phys. Rev. Lett. **56**, 1400 (1986); S. Ciraci and I.P. Batra, Phys. Rev. B **38**, 1835 (1988); B. Koiller and M.O. Robbins, Phys. Rev. B **40**, 12554 (1989).

[45] F.K. LeGoues, V.P. Kesan, and S.S. Iyer, Phys. Rev. Lett. **64**, 40 (1990).

[46] H. von Kanel, E. Müller, H.-U. Nissen, W. Bacsa, M. Ospelt, K.A. Mäder, R. Stalder, and A. Baldereschi, J. Cryst. Growth **11**, 889 (1991); E. Müller, H.-U. Nissen, K.A. Mäder, M. Ospelt, H. von Kanel, Phil. Mag. Lett. **64**,183 (1991).

[47] V.P. Kesan, F.K. LeGoues, and S.S. Iyer, Phys. Rev. B **46**, 1576 (1992).

[48] F.K. LeGoues, V.P. Kesan, S.S. Iyer, J. Tersoff, and R. Tromp, Phys. Rev. Lett. **64**, 2038 (1990).

[49] A. Qteish and R. Resta, Phys. Rev. B **37**, 6983 (1988).

[50] P.C. Kelires and J. Tersoff, Phys. Rev. Lett. **63**, 1164 (1989).

[51] J.C. Woicik, C.E. Bouldin, M.I. Bell, J.O. Cross, D.T. Tweet, B.D. Swanson, T.M. Zhang, L.B. Sorensen, C.A. King, J.L. Hoyt, P. Pianetta, and J.F. Gibbons, Phys. Rev. B **43**, 2419 (1991); H. Kajiyama, S. Muramatsu, T. Shimada, and Y. Nishino, Phys. Rev. B **45**, 14005 (1992).

[52] B. Jusserand, D. Paquet, and F. Mollot, Phys. Rev. Lett. **63**, 2397 (1989).

[53] B. Jusserand, F. Mollot, L.G. Quagliano, G. Le Roux, and R. Planel, Phys. Rev. Lett. **67**, 2803 (1991).

[54] M. Bernasconi, L. Colombo, L. Miglio, and G. Benedek, Phys. Rev. B **43**, 14447 (1991); M. Bernasconi, L. Colombo, and L. Miglio, Phys. Rev. B **43**, 14457 (1991).

[55] *Numerical Data and Functional Relationships in Science and Technology*, edited by K.-H. Hellwege and 0. Madelung, Landolt-Börnstein, New Series, Group III, Vols. 17a and 22a (Springer, New York, 1982), and references quoted therein.

[56] D. Strauch and B. Dorner, J. Phys.: Condens. Matter **2**, 1457 (1990).

[57] a) A. Onton, in *Proc. 10th Int. Conf. Phys. Semiconductors*, USAEC, New York (1970), p. 107; b) B. Monemar, Phys. Rev. B **8**, 5711 (1973).

[58] D. Strauch, B. Dorner, and K. Karch, in *Proc. 3rd International Conference on Phonon Physics*, edited by S. Hunklinger, W. Ludwig, and G. Weiss (World Scientific, Singapore, 1990), p. 82.

[59] P. Giannozzi and L. Colombo, unpublished; P. Giannozzi, private communication.

[60] K. Kunc and R.M. Martin, in *Ab Initio Calculation of Phonon Spectra*, edited by J.T. Devreese, V.E. van Doren, and P.E. van Camp (Plenum, New York, 1983), p. 65.

[61] K. Kunc and P. Hagège, in *Phonon Physics*, edited by J. Kollár, N. Kroó, N. Menyhárd, and T. Siklós (World Scientific, Singapore, 1985), p. 943.

[62] P. Parayanthal and F.H. Pollak, Phys. Rev. Lett. **52**, 1822 (1984).

[63] J.A. Kash, J.M. Hvam, J.C. Tsang, and T.F. Kuech, Phys. Rev. B **38**, 5776 (1988).

[64] R. Tsu, H. Kawamura, and L. Esaki, in *Proc. of the 11th International Conference on the Physics of Semiconductors, Warsaw, 1972*, edited by M. Miasek (PWN Polish Scientific, Warsaw, 1972), p. 1135.

[65] B. Jusserand and J. Sapriel, Phys. Rev. B **24**, 7194 (1981).

[66] A detailed analysis of the effects of cationic intermixing at the interfaces of *GaAs/AlAs* (001) superlattices—using much the same techniques used here for the homogeneous alloy—is beyond the scope of this work and has been presented in a number of parers to which we refer for details: E. Molinari, S. Baroni, P. Giannozzi, and S. de Gironcoli, in *Proc. 20th International Conference on the Physics of Semiconductors*, edited by E. Anastassakis and J.D. Joannopoulos (World Scientific, Singapore, 1990), p. 1427; E. Molinari, S. Baroni, P. Giannozzi, and S. de Gironcoli, Phys. Rev. B **45**, 4280 (1992); S. Baroni, P. Pavone, P. Giannozzi, S. de Gironcoli, and E. Molinari, in *Proc. International School of Physics "Enrico Fermi", course CXVII, "Semiconductors Superlattices and Iterfaces"*, edited by L. Miglio and A. Stella (Academic, New York, 1992), in press.

[67] B.A. Weinstein and G.J. Piermarini, Phys. Rev. B **12**, 1172 (1975); J. Buchenauer, F. Cerdeira, and M. Cardona, in *Proceedings of the 2nd International Conference of Light Scattering in Solids*, edited by M. Balkanski, (Flammarion, Paris, 1971), p. 280.

[68] G. Dolling, in *Inelastic Scattering of Neutrons in Solids and Liquids* IAEA, Vienna 1963, Vol. II, p. 37; G. Nilsson and G. Nelin, Phys. Rev. B **6**, 3777 (1972).

[69] G. Nilsson and G. Nelin, Phys. Rev. B **3**, 364 (1971).

[70] S. de Gironcoli, Phys. Rev. B **46**, 2412 (1992).

[71] S. de Gironcoli, P. Giannozzi, and S. Baroni, Phys. Rev. Lett. **66**, 2116 (1991).

[72] R.J. Elliott, J.A. Krumhansl, and P.L. Leath, Review of Modern Physics **46**, 465 (1974).

[73] J.L. Beeby and S.F. Edwards, Proc. R. Soc. A **274**, 395 (1963).

[74] P. Soven, Phys. Rev. **156**, 809 (1967); D.W. Taylor, Phys. Rev. **156**, 1017 (1967).

[75] S. Wilke, J. Mašek, and B. Velický, Phys. Rev. B **41**, 3769 (1990).

[76] M.A. Renucci, J.B. Renucci, and M. Cardona, in *Light Scattering in Solids*, edited by M. Balkanski (Flammarion, Paris, 1971), p. 326.

[77] W.J. Brya, Solid State Commun. **12**, 253 (1973).

[78] M.I. Alonso and K. Winer, Phys. Rev. B **39**, 10056 (1989).

[79] G.M. Zinger, I.P. Ipatova, and A.V. Subashiev, Sov. Phys. Semicond. **11**, 383 (1977).

[80] C.H. Grein and M. Cardona, Phys. Rev. B **45**, 8328 (1992).

[81] D.J. Lockwood, K. Rajan, E.W. Fenton, J.-M. Baribeau, and M.W. Denhoff, Solid State Commun. **61**, 465 (1987).

[82] R.W. Godby, M. Schlüter, and L.J. Sham, Phys. Rev. B **35**, 4170 (1987)

[83] A.-B. Chen and A. Sher, Phys. Rev. B **23**, 5360 (1981).

[84] Z.Q. Li and W. Pötz, Phys. Rev. B **43**, 12670 (1991).

[85] R. Haydock, in *Solid State Physics*, edited by H. Ehrenreich, F. Seitz and D. Turnbull (Academic press, New York, 1980), Vol. 35.

[86] J.S. Nelson, A.F. Wright, and C.Y. Fong, Phys. Rev. B **43**, 4908 (1991).

[87] V. Fiorentini and A. Baldereschi, J. Phys. Condens. Matter **4**, 5967 (1992).

[88] B. Monemar, K.K. Shih, and G.D. pettit, J. Appl. Phys. **47**, 2604 (1976); R. Dingle, R.A. Logan, and J.R. Arthur Jr., Inst. Phys. Conf. Ser. **33a**, 210, (1977).

[89] C. Bosio, J.L. Staehli, M. Guzzi, G. Burri, and R.A. Logan, Phys. Rev. B **38**, 3263 (1988).

[90] J.C.M. Henning, J.P.M. Ansems, and P.J. Roksnoer, J. Phys. C **19**, L335 (1986).

[91] V. Fiorentini, Phys. Rev. B **46**, 2086 (1992).

[92] G.B. Bachelet and N.E. Christensen, Phys. Rev. B **31**, 879 (1985).

[93] E. Caruthers, and P.J. Lin-Chung, Phys. Rev. Lett. **38**, 1534 (1977); E. Caruthers, and P.J. Lin-Chung, Phys. Rev. B **17**, 2705 (1978); J.N. Schulmann and T.C. McGill, Phys. Rev. B **19**, 6341 (1979); W. Andreoni and R. Car, Phys. Rev. B **21**, 3334 (1980); K.K. Mon, Solid State Commun. **41**, 199 (1982).

[94] M. Garriga, M. Cardona, N.E. Christensen, P. Lautenschlager, T. Isu, and K. Ploog, Phys. Rev. B **36**, 3254 (1987); M. Cardona, T. Suemoto, N.E. Christensen, T. Isu, and K. Ploog, Phys. Rev. B **36**, 5906 (1987); M. Alouani, S. Gopalan, M. Garriga, and N.E. Christensen, Phys. Rev. Lett. **61**, 1643 (1988).

[95] S.-H. Wei and A. Zunger, J. Appl. Phys. **63**, 5794 (1988); D.M. Wood, S.-H. Wei, and A. Zunger, Phys. Rev. B **37**, 1342 (1988).

[96] M.F. Ling and D.J. Miller, Phys. Rev. B **38**, 6113 (1988).

[97] G. Barraf and M. Schlüter, Phys. Rev. B **30**, 3460 (1984).

[98] W. von der Linden, P. Horsh, and W.-D. Lukas, Solid State Commun. **59**, 485 (1986).

[99] N. Marzari, graduation thesis; N. Marzari, private communication.

[100] G.B. Bachelet, D.R. Hamann, and M. Schlüter, Phys. Rev. B **26**, 4199 (1982).

Remerciement

Je tiens à remercier les Proff. Franco Bassani et Manuel Cardona, et le Dr. Klaus Maschke pour avoir accepté de faire partie de mon jury de thèse, ansi que mon directeur de thèse Prof. Alfonso Baldereschi pour m'avoir entroduit au sujet de ce travail et pour la confiance et la liberté qu'il m'a accordées.
Je tiens également à remercier Stefano Baroni et Paolo Giannozzi pour m'avoir donné l'opportunité de travailler avec eux et de profiter de leur amitié et expérience.
Je remercie Pietro Ballone pour l'intérêt qu'il a démontré pour mon travail, par les nombreuses discussions toujours utiles et une lecture attentive de cette mémoire dans une forme encore provvisoire.
Que tous les amis de IRRMA et non trouvent ici l'expression de ma reconnaissance pour les quatre ans passés ensemble (trop vite) à Lausanne.
Un merci particulier va à Silvia Rubini pour son soutien et amitié.

CURRICULUM VITÆ

Nom et Prénom	de GIRONCOLI Stefano
Né le	24 janvier 1964 à Trieste (Italie)
Nationalité	Italienne
1970-1978	Etudes primaires et secondaires à Trieste
1978-1983	Liceo Scientifico à Trieste
1983-1988	Etudes de Physique, Université de Trieste
1 oct. 1988	Diploma di Laurea in Fisica
1989-1992	Assistant à l'Institut Romand de Recherche numérique en physique de MAtériaux (IRRMA), EPFL